First-Principle Modeling and Machine Learning for Space Weather Forecasting

by

Xiantong Wang

A dissertation submitted in partial fulfillment
of the requirements for the degree of
Doctor of Philosophy
(Climate and Space Sciences and Engineering and Scientific Computing)
in the University of Michigan
2022

Doctoral Committee:

Research Professor Gábor Tóth, Chair
Associate Research Scholar Yuxi Chen
Professor Tamas I. Gombosi
Professor Kenneth G. Powell
Professor Tuija Pulkkinen

Xiantong Wang
xtwang@umich.edu
ORCID iD: 0000-0002-8963-7432

DEDICATION

To my parents, who introduced this colorful world to me.
献给我的父母，他们向我介绍了这个多彩的世界。

ACKNOWLEDGMENTS

This work is supported by NSF PRE-EVENTS grant No.1663800 and NASA grant 80NSSC20K0600. I am grateful to the NSF and NASA for paying the tuition, stipend, and travel costs. I also want to thank Horace H. Rackham School of Graduate Studies for their support in traveling to American Geophysical Union conferences.

High-performance computing resources supporting this work were provided by the NASA Pleiades Supercomputer through the NASA Advanced Supercomputing (NAS) Division at Ames Research Center and the Frontera Supercomputer in the Texas Advanced Computing Center (TACC) at The University of Texas at Austin.

Foremost I want to thank my advisor Dr. Gábor Tóth, who provided thoughtful guidance and detailed assistance throughout my entire dissertation work during the past few years. I cannot imagine I can accomplish so much without working with you. I want to thank Dr. Yang Chen from the Department of Statistics and Dr. Alfred O. Hero, III from the Department of EECS for their mentoring on the machine learning project. I am also thankful to other members of my dissertation committee: Drs. Yuxi Chen, Tamas I. Gombosi, Kenneth G. Powell, and Tuija Pulkkinen for taking the time reading through the dissertation and providing feedbacks.

During my academic and personal life, I received many helps from my colleagues and friends. I want to thank Dr. Yuxi Chen for every minute I spent at your office desk. Your knowledge and experience not only helped me through the obstacles, but also inspired me to be a better researcher. I want to express my thanks to Dr. Wenzao Li at Stony Brook,

for the wise perspectives you shared and the thirteen U.S. states we have visited together so far. Special thanks to Dr. Nishtha Sachdeva for willing to listen to my hours and hours of confusion and panic during the COVID-19 pandemic. Thank you Simin Zhang and Shuang Xu for coming by from Columbus and checking on me during the pandemic, you are truly loyal friends! I appreciate the cookies and lasagna I got from Timothy Keebler, also the time we spent in the parks. I want to thank other members in my research group: Hongyang Zhou, Fuming Chang and Yifu An for the wonderful time we worked together. Thanks to the events organized by CLaSP GUStO, I tried things that I didn't think about doing before but now being a part of my life.

Thank you to staffs of the CLaSP department: Darren Britten-Bozzone, Laura Hopkins, Claire Miller, Rachel Long, Faye Ogasawara, and Sandra Pytlinski. I wouldn't be able to make it here without a fantastic department you all are running!

TABLE OF CONTENTS

LIST OF FIGURES

FIGURE

LIST OF TABLES

TABLE

ABSTRACT

Space weather is becoming a topic that has attracted increasing attention during the past few decades. The increase of human activities in space makes it critical to understand space weather events better. This dissertation applies a novel first-principle model to investigate the multi-scale physics in the Earth magnetosphere under strong solar wind driving conditions that have geomagnetic impacts and a machine learning model to perform solar flare forecasting related to the energy source of the space weather events.

I perform a geomagnetic event simulation using a newly developed magnetohydrodynamic with adaptively embedded particle-in-cell (MHD-AEPIC) model, the first global geomagnetic storm simulation containing kinetic physics. I have developed effective criteria for identifying reconnection sites in the magnetotail and covering them with the PIC model. I compare the MHD-AEPIC simulation results with Hall MHD and ideal MHD simulations to study the impacts of kinetic reconnection at multiple physical scales. Three models produce very similar global scale features such as SYM-H, SuperMag Electrojet (SME) indexes, polar cap potentials, and field-aligned currents. They also produce good agreements with in-situ Geotail observations at the mesoscale. At the kinetic scale, the MHD-AEPIC simulation can produce a crescent shape distribution of the electron velocity space at the electron diffusion region, which agrees very well with Magnetospheric Multiscale (MMS) satellite observations. The MHD-AEPIC model compares well with observations at all scales, it works robustly, and the computational cost is acceptable due to the adaptive adjustment of the PIC domain.

I investigate a kinetic physics mechanism in the magnetotail to induce sawtooth oscillations. The simulation results of our global MHD model with local kinetic physics show that when the total magnetic flux from the solar wind exceeds a threshold, sawtooth-like

magnetospheric oscillations can be generated even without time-varying ionospheric outflow. The period of the oscillations varies from 1.5 to 3 hours, in good agreement with observations. The amplitude of the oscillations measured in the local B_Z field also agrees well with observations at $8\,R_E$ distance from the center of Earth. The simulated oscillations cover a wide range of local times, similar to observations, although the distribution of magnitude as a function of local time is somewhat different from the observed distribution. This work suggests that kinetic reconnection physics in the magnetotail can be a major contributing factor to magnetospheric sawtooth oscillations.

I implemented a deep learning network using Long-Short Term Memory (LSTM) to predict whether a solar active region (AR) will produce a flare of class Γ in the next 24 hours. The essence of using LSTM, a recurrent neural network, is its capability to capture temporal information of the data samples. The input features are time sequences of 20 magnetic parameters from the Space-weather HMI Active Region Patches (SHARPs). I analyze active regions from June 2010 to Dec 2018 and their associated flares identified in the GOES X-ray flare catalogs. The results (i) produce skill scores consistent with recently published results using LSTMs and are better than the previous results using single time input. (ii) The skill scores from the model show statistically significant variation when different years of data are chosen for training and testing. In particular, the years 2015 to 2018 have better True Skill Statistic (TSS) and Heidke Skill Scores (HSS) for predicting $\geq C$ medium flares than 2011 to 2014.

CHAPTER 1

Introduction and Motivation

This chapter starts with an introduction to the solar wind and its interaction with the Earth's magnetosphere. Then the concept of space weather and the motivation for studying it will be explained. In the end, we will present the outline of this dissertation.

1.1 Solar Wind and Earth's Magnetosphere

The Sun is the only star in our solar system, which is the dominant energy source that drives the physical phenomena in our space environment. One "basic" mode of the Sun and Earth interaction is through the solar wind, which is the extension of the solar corona. This section will describe how the solar wind originates and how the Earth's magnetosphere reacts to it.

1.1.1 Solar Wind

When Biermann [1951] was studying the acceleration of the plasma structures in comet tails, he suggested the existence of a continuous solar wind coming out from the Sun with speed ranges from 500 km/s to 1500 km/s. Parker [1958] then came up with mathematical theory of the solar wind. He pointed out that the hydrostatic solution cannot represent an equilibrium solution of the hot solar corona. The solar wind can be accelerated towards supersonic speed by the pressure difference between the base of the solar corona and the interstellar medium, since the pressure in the latter is ten orders of magnitude smaller than the former. He also

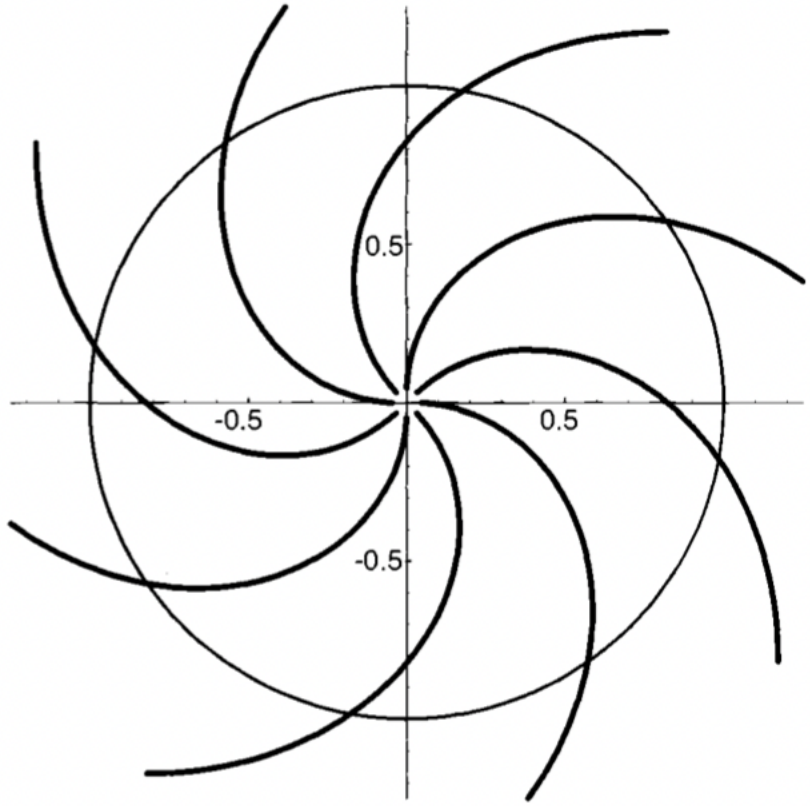

Figure 1.1: A schematic plot of the spiral shape of the interplanetary magnetic field [Gombosi, 1998].

pointed out the existence of the interplanetary magnetic field (IMF), which is the extension of the solar magnetic field into the interplanetary medium. The rotation of the Sun results in a spiral structure of the IMF that is called the Parker spiral, see Figure 1.1.

The first continuous observation of the solar wind is reported by Snyder and Neugebauer [1965] from the Marine-2 mission. Figure 1.2 shows the measurement in a 4-month time range. The solar wind velocity varies from 300 km/s to 700 km/s, and the proton density varies from 1 cm^{-3} to about 100 cm^{-3}. Based on many observations, including the Ulysses spacecraft, the solar wind can be classified into two categories: the slow wind with a typical velocity of 300-500km/s and a composition that is similar to the corona, and the fast wind with a typical velocity of 750km/s and a composition that matches the photosphere. The origin of the fast solar wind is believed to be the coronal holes on the Sun, where field lines

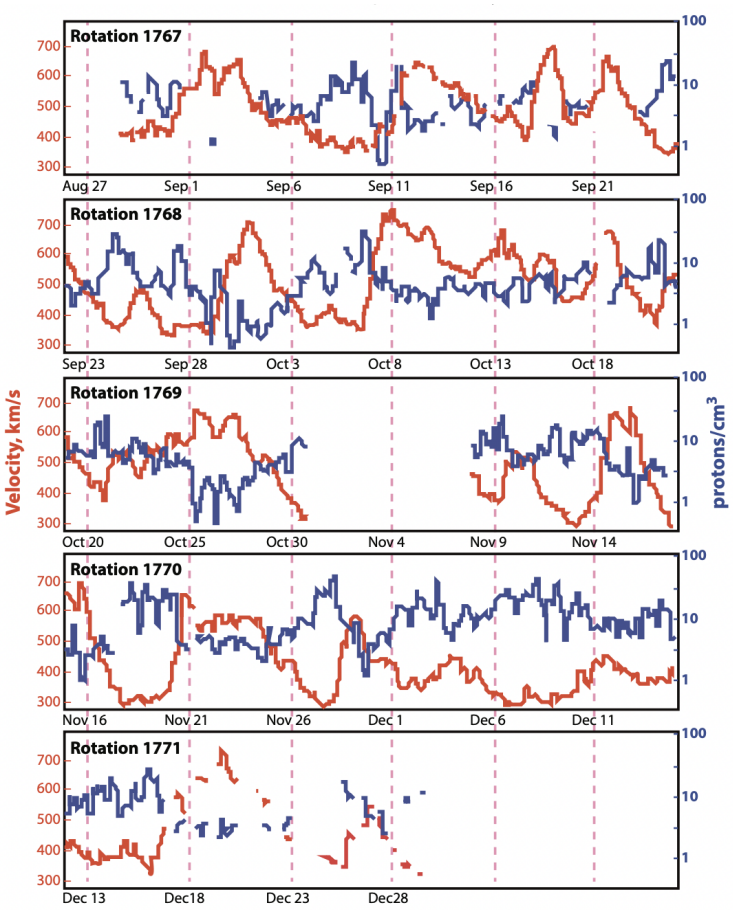

Figure 1.2: The Marine-2 Measurement of the solar wind velocity and proton density [Snyder and Neugebauer, 1965].

are open to the interplanetary space.

The solar wind consists of electrons and ions, as well as the interplanetary magnetic field (IMF). When the solar wind interacts with the planets that have an intrinsic magnetic field, it drives the formation and evolution of the planetary magnetospheres. We will introduce Earth's magnetosphere specifically in the next subsection, which is studied in this dissertation.

1.1.2 Earth's Magnetosphere

The Earth's magnetosphere is formed as a result of the interaction of the superfast, magnetized solar wind with the intrinsic magnetic field of the Earth. The magnetosphere is

the region that is controlled by the Earth's intrinsic magnetic field, which extends from the bottom of the ionosphere to more than ten Earth radii (R_E) in the sunward direction and to several hundred R_E in the anti-sunward direction.

The Earth's magnetic field can be approximated very well using a magnetic dipole field. The dipole field parameters for 1990 are summarized in Table 1.1. In addition to the dipole field, the dipole axis is tilted around 10.8° from the axis of terrestrial rotation. The Earth's rotation axis is also inclined 23.5° to the ecliptic plane. As a consequence of the Earth's daily rotation and its orbit around the Sun, the angle between the Sun-Earth line and the terrestrial magnetic dipole varies between about 56° and 90°. The variation of this angle has important consequences for the Earth's magnetosphere configuration.

Quantity	**Symbol**	**Value**
Dipole moment	$\frac{\mu_0}{4\pi} M_E$	$7.84 \times 10^{15} T \cdot m^3$
Tilt of dipole axis		10.8°
Geographic latitude of magnetic north pole	λ_N	79.2°
Geographic longitude of magnetic north pole	ϕ_N	$289° E$

Table 1.1: Terrestrial dipole parameters in 1990 [Gombosi, 1998].

When the magnetized solar wind flow arrives at the Earth, the terrestrial magnetic field significantly deviates from the dipole field and forms the magnetosphere. Figure 1.3 shows a schematic representation of the magnetosphere in the noon-midnight meridian. Since the solar wind is superfast, a bow shock exists before the solar wind reaches the magnetosphere. The solar wind gets slowed down but compressed and heated across the bow shock. The location of the bow shock depends on the solar wind condition as well as the shape of the planet's body. The Earth's bow shock is about $3\,R_E$ away from the edge of the magnetosphere. The position where the total pressure of the confined Earth's dipole field balances the solar wind after shock is called the magnetopause. The area between the bow shock and the magnetopause is called the magnetosheath. Different from the dayside magnetic field lines of the dipole, where they are compressed by the solar wind, the field lines at the nightside are stretched to form a region called the magnetotail. The magnetotail is divided into two

parts by the current sheet. The magnetic field lines in the northern lobe are pointing toward the Earth, while the field lines in the southern lobe are pointing away from the Earth.

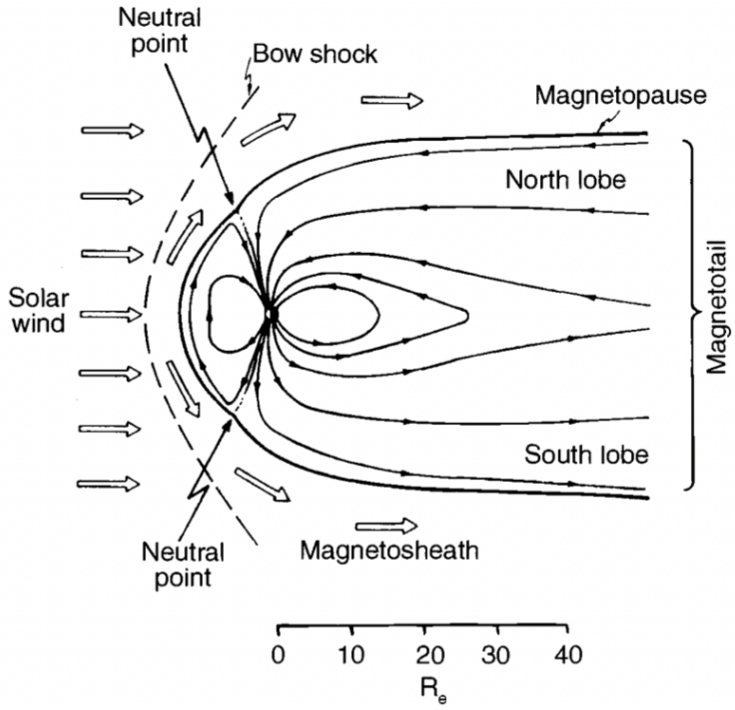

Figure 1.3: The schematic plot of the meridional plane of the Earth's magnetosphere [Vasyliunas, 1983].

There are several regions inside the magnetosphere populated by magnetosheath-type plasma. These regions are called magnetospheric boundary layers. As shown in Figure 1.4, the region where the magnetosheath plasma extends deep into the magnetosphere is the polar cusp. The low latitude boundary layer (LLBL) is a thin region just inside the magnetopause. The plasma population inside the LLBL resembles that in the magnetosheath, which indicates that the magnetopause is not a perfectly conducting layer that blocks all the incoming plasma particles. Plasma from the magnetosheath expands into the plasma mantle, and the field lines are convected towards the magnetotail. In the plasma sheet, there is hot and dense plasma extending along the center of the magnetotail. Between the plasma sheet and the plasma mantle are the magnetotail lobes, which have very low plasma densities and steady and strong magnetic fields (low plasma β). A magnetosphere that contains both

plasma and magnetic fields can change dynamically, driven by the solar wind.

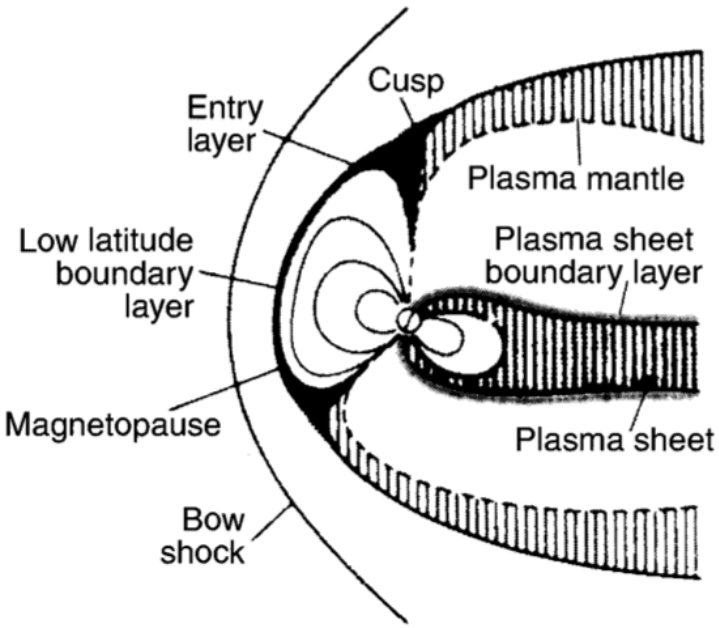

Figure 1.4: The schematic plot of the magnetospheric boundary layers [Gombosi, 1998].

1.1.3 Dungey Cycle

The magnetosphere is not a still system, and there is a global magnetospheric convection called the Dungey cycle. First discussed by Dungey [1961], this convection mode exists because magnetic reconnection, a fundamental plasma process that transports energy from the magnetic field to the plasma, happens both at the dayside magnetopause and the magnetotail. Figure 1.5 shows the progression of the Dungey cycle. The closed field lines in the magnetosphere (red) reconnect with the solar wind magnetic field lines (blue) and result in "open" field lines that are connected to the planet at one end (purple). Meanwhile, plasma is transported poleward through the cusps and into the magnetotail. Hence the magnetic flux is accumulated on open field lines in the magnetotail. Then the magnetic reconnection across the tail current sheet returns plasma on closed field lines (red) back towards the Earth. Meanwhile, the magnetic flux returns to the dayside that completes the Dungey cycle. At

Earth, the Dungey cycle takes about 1 hour.

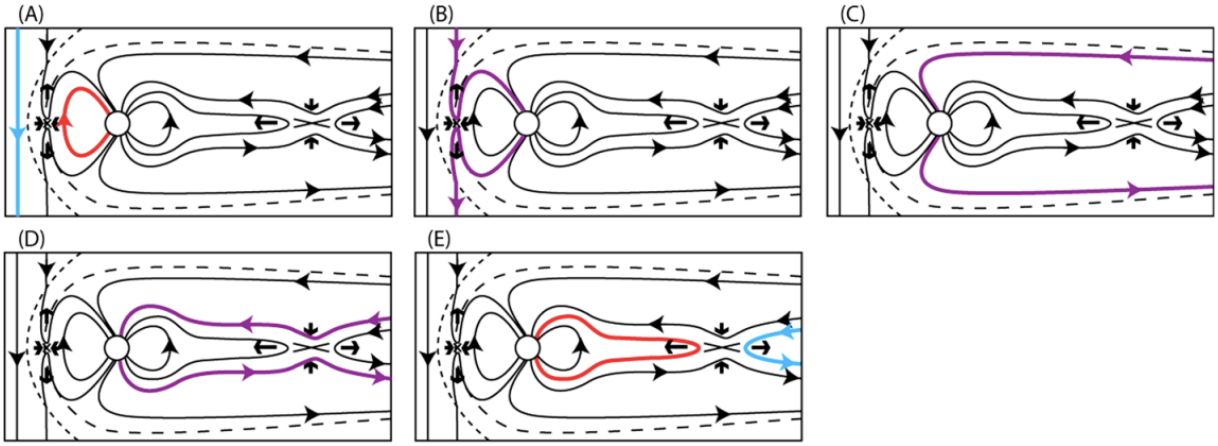

Figure 1.5: Cartoon showing the progression of the Dungey cycle [Eastwood et al., 2015].

1.2 Space Weather

The term "Space Weather" refers to the collective, often violent, changes in the space environment surrounding the Earth. In the past few decades, the usage of space-based assets for navigation, communication, military reconnaissance, and exploration has increased a lot. Meanwhile, observations, numerical simulations, and predictive models are helping important efforts to study and forecast space weather (National Space Weather Program Strategic Plan [Williamson et al., 2010]).

The study of space weather is essentially the study of the linked Sun-Earth system. The Sun is the dominant driver of the space weather effects in near-Earth space. The solar wind emanating from the Sun – and the embedded interplanetary magnetic field (IMF) – provides the energy and much of the mass that drives the dynamics of Earth's magnetosphere. Earth's ionosphere and atmosphere respond to solar wind driving in complicated ways. The ionosphere can supply particles (mass) to populate the terrestrial magnetosphere. The neutral atmosphere responds strongly to solar irradiance as well as to plasma interactions with the solar wind.

1.2.1 Solar Flare

Solar activity is the energy source of almost all space weather events that have terrestrial impacts. Solar flares are a major form of solar activity that we will focus on in this dissertation. A solar flare is a localized explosive release of energy that appears as a sudden, short-lived brightening of an area in the chromosphere. Solar flares release their energy mainly in the form of electromagnetic radiation and energetic particles. Figure 1.6 shows the image of a solar flare that happened in April 2022. The intensity of solar flares is measured by the X-ray emission, which can be enhanced by several orders of magnitudes. The most common X-ray index is based on the peak energy flux of the flare in the 1 to 8 $\mathring{A}$ soft X-ray band measured by geosynchronous satellites. The first symbol characterizes the order of magnitude ($C = 10^{-3}$ ergs cm^{-2} s^{-1}, $M = 10^{-2}$ ergs cm^{-2} s^{-1}, $X = 10^{-1}$ ergs cm^{-2} s^{-1}), followed by the most significant digit of the actual peak flux. For instance, a peak flux of 6.3×10^{-2} ergs cm^{-2} s^{-1} is reported as an M6 soft X-ray flare.

Although solar flares mostly occur in closed field line regions and their plasma emission is usually not very significant, solar flares can generate energetic particle events, which may have interaction with Earth's space environment and pose a potential threat to human activities. Moreover, solar flares are closely related to coronal mass ejections (CMEs), which can cause geomagnetic storms if they hit the Earth. Compagnino et al. [2017] analyzed solar flares and CMEs from solar cycles 23 and 24. From the CME catalog provided by the Coordinated Data Analysis Workshops (CDAW), 56.47% of C flares, 69.43% of M flares, and 89.39% of X flares are associated with CMEs within a 2-hour time window. Hence, it is significant to have an accurate and reliable prediction of solar flares, especially the strong ones.

In the past decade, NASA's Solar Dynamics Observatory (SDO) has provided massive observational data of the Sun. The Helioseismic and Magnetic Imager (HMI) instrument onboard provides dopplergrams (maps of solar surface plasma velocity), continuum filtergrams (broad-wavelength photographs of the solar photosphere), and both line-of-sight and

vector magnetograms (maps of the photospheric magnetic field). In this dissertation, we will make use of one data product derived from the HMI magnetograms, the Spaceweather HMI Active Region Patch (SHARP), to build a machine learning-based solar flare forecasting model. More details can be found in Chapter 5.

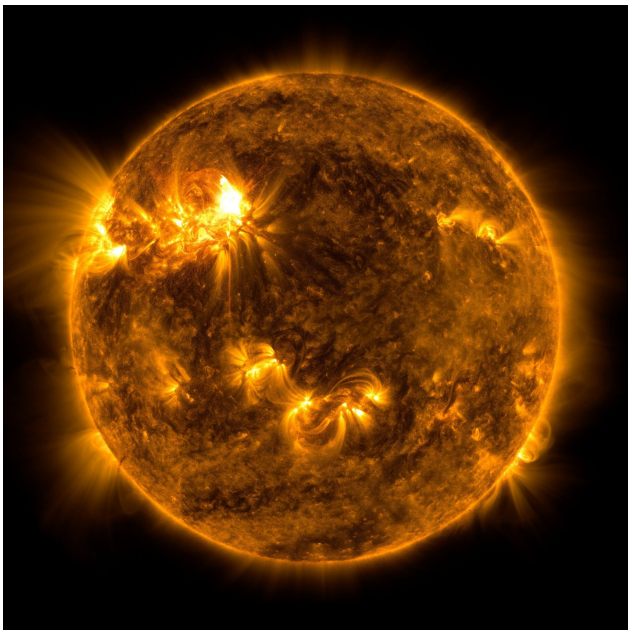

Figure 1.6: NASA's Solar Dynamics Observatory captured this image of a solar flare - the bright flash in the upper left portion of the image– on April 20, 2022. The image shows the intensity at the 171 $\mathring{A}$ wavelength, which represents the emission from the upper transition region and quiet solar corona. Credit: SDO/NASA (https://blogs.nasa.gov/solarcycle25/2022/04/21/moderate-solar-flare-erupts-from-sun)

1.2.2 Magnetic Reconnection

As described in the previous section, an important topic of space weather is how energy is transported or transformed within the Sun-Earth system. Magnetic reconnection is the physical process that rearranges the magnetic field topology and converts the magnetic field energy to kinetic and thermal energy. Figure 1.7 is a schematic diagram of magnetic reconnection. This physical process is observed in many places in the heliosphere [Masuda et al., 1994, Tsuneta, 1996], at Earth's magnetopause [Burch and Phan, 2016] and in the magnetotail [Nagai et al., 2001].

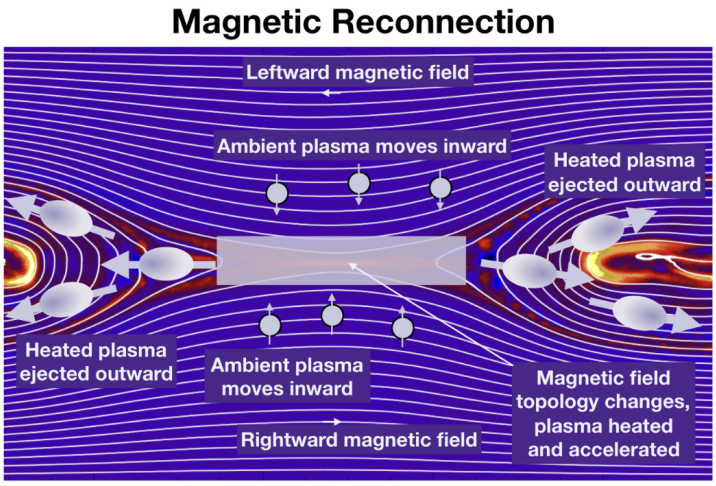

Figure 1.7: Simplified two-dimensional schematic diagram of magnetic reconnection. Oppositely directed magnetic fields (light blue lines) and ambient plasma (light blue circles) move into the diffusion region (shaded box in the center), where magnetic reconnection occurs. The plasma is heated and accelerated into jets to the left and right (shaded blue ovals) [Hesse and Cassak, 2020].

The first theoretical magnetic reconnection model is called the Sweet-Parker model proposed by Parker [1957]. The left panel of Figure 1.8 is a sketch of the Sweet-Parker model. Suppose two oppositely directed magnetic fields $\pm B$, in a plasma with density ρ and conductivity σ, are carried toward the neutral line at speed $v_{\rm in}$ over a characteristic length $2L$. There is a layer of width 2δ where the field reconnects. The reconnected field and plasma are expelled at speed $v_{\rm out}$. Assume the system is in a steady state. According to the conservation of mass and energy (using CGS units),

$$Lv_{\rm in} \sim \delta v_{\rm out} \tag{1.1}$$

$$Lv_{\rm in}\frac{B^2}{8\pi} \sim \delta v_{\rm out}\frac{\rho v_{\rm out}^2}{2} \tag{1.2}$$

combining these equations, the outflow scales with the upstream Alfvén speed,

$$v_{\rm out} \sim v_A \equiv \frac{B}{\sqrt{4\pi\rho}} \tag{1.3}$$

considering the electric field outside the layer balances the resistive electric field inside the layer

$$\frac{v_{\rm in}B}{c} \sim \eta J \sim \frac{c\eta}{4\pi}\frac{B}{\delta} \tag{1.4}$$

η is the electric resistivity and the current J is acquired from Ampere's law: $\mathbf{J} = \frac{c}{4\pi}\nabla \times \mathbf{B}$. Hence

$$v_{\rm in} \sim \frac{c^2\eta}{4\pi}\frac{1}{\delta} = \frac{D_\eta}{\delta} \tag{1.5}$$

where the magnetic diffusivity $D_\eta = \frac{c^2\eta}{4\pi}$. Hence

$$v_{\rm in}^2 = v_{\rm in}\cdot v_{\rm in} \sim \frac{D_\eta}{\delta}\cdot\frac{\delta v_{\rm out}}{L} = v_{\rm out}^2\frac{D_\eta}{Lv_{\rm out}} \sim v_{\rm out}^2\frac{D_\eta}{Lv_A} \tag{1.6}$$

Here we defined the reconnection rate

$$R = \frac{v_{\rm in}}{v_{\rm out}} = \sqrt{\frac{v_{\rm in}^2}{v_{\rm out}^2}} \sim \sqrt{\frac{D_\eta}{Lv_{\rm A}}} = \frac{1}{\sqrt{S}} \tag{1.7}$$

S is defined as the Lundquist number $S = \frac{Lv_A}{D_\eta}$. Most astrophysical systems, like a solar flare or magnetotail current, have a very large Lundquist number from 10^9 and 10^{20}. Hence the Sweet-Parker reconnection rate is very low. In order to achieve a higher S, the resistive layer must be thin because that is the only way to make the current density large enough to dissipate the incoming magnetic energy. But the resistive layer width is also the width of the outflow, which means that the mass flux out of the layer is very small, which limits $v_{\rm in}$. To achieve a higher reconnection rate, Petschek [1964] proposed an X-point geometry where the length scale L is replaced by a much smaller length scale $L^{'}$. Hence the reconnection rate increases by $\sqrt{L/L'}$. Petschek derived a family of solutions and illustrated that the reconnection rate in this model $R \sim \frac{1}{\ln S}$, which is higher than the Sweet-Parker reconnection rate. However, the major limitation of the Petschek model is that spatially-localized resistivity (anomalous resistivity) is required to get Petschek reconnection in resistive MHD simulations. The anomalous resistivity requires collisionless effects that fall into a length

scale where MHD breaks down.

To introduce a more self-consistent mechanism beyond the ideal MHD theory, Hall and electron pressure terms are introduced into the generalized Ohm's law and applied into the MHD equations. In the generalized Ohm's law,

$$\mathbf{E} + \mathbf{u} \times \mathbf{B} = \eta \mathbf{J} + \frac{1}{ne}\mathbf{J} \times \mathbf{B} - \frac{\nabla \cdot \mathbf{P}_e}{ne} \tag{1.8}$$

the first and second terms on the right-hand side are the resistive term and Hall term, respectively. Hall effect, which is a result of electron-ion velocity difference at the sub-ion gyroradius scales can change the geometry of magnetic reconnection. The third term is the divergence of the electron pressure tensor, which can potentially break the frozen-in condition and induce the magnetic reconnection. Simulations also show that the reconnection rate is higher when the Hall effect is included [Birn et al., 2001b, Ma and Bhattacharjee, 2001, Murphy et al., 2009b], and the reconnection geometry resembles the Petschek model.

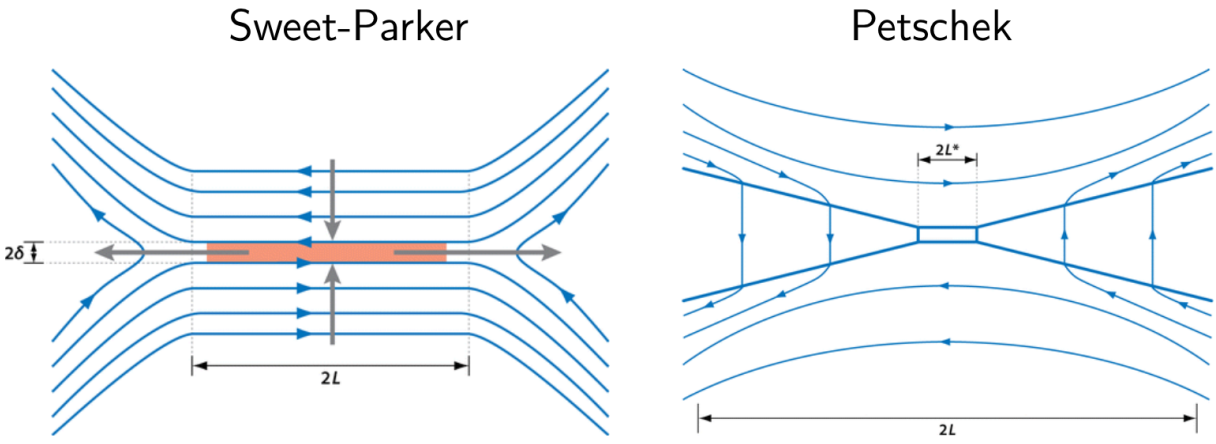

Figure 1.8: Sketch of magnetic field geometry in Sweet-Parker and Petschek reconnection models [Zweibel and Yamada, 2009].

However, the Hall effect is not the whole story. In fact, the MHD assumption is not valid anymore inside the diffusion regions of the magnetic reconnection where the magnetic field is weak, and the ions and electrons are unmagnetized. Non-Maxwellian distributions

of the particles are observed by NASA's Magnetospheric Multiscale (MMS) mission [Burch et al., 2016b]. The important divergence of the electron pressure tensor is also better to be studied directly from the particles. Hence, kinetic models, which directly simulate the motion of particles and electromagnetic fields, are necessary to understand the kinetic physics of magnetic reconnection. We will discuss more in Chapter 2 how we incorporate the particle-in-cell model, which is a kinetic model, into the global magnetospheric simulation.

1.2.3 Magnetospheric Substorms and Storms

As described in 1.1.3, the Dungey cycle plays an important role in the magnetospheric dynamics. When the dayside reconnection continues for an extended interval with southward IMF and the open flux accumulates in the magnetotail, the magnetosphere can become highly dynamic. Magnetospheric substorms and storms are two major types of magnetospheric activity that have significant space weather impacts.

A magnetospheric substorm is a periodic release of the accumulated energy in the magnetotail [Rostoker et al., 1980, Baker et al., 1996, Angelopoulos et al., 2008]. As the magnetic field strength in the lobes increases, the magnetotail current sheet becomes thinner. The reconnection happens in the closed field line region leading to the formation of a plasmoid, which is bounded by the magnetic tension of the surrounding closed field lines connected to the Earth. While there are still debates about the exact trigger of the substorms, the most accepted theory is that a reconnection X-line forms between $20 \sim 30\,R_E$ from the Earth [Nagai et al., 1998]. Eventually, the open field lines begin to reconnect, at which point the plasmoid is released and can move downtail [Hones Jr, 1978, Baker et al., 1996, Slavin et al., 1999, 2002]. The formation of the near-Earth neutral line results in the Earthward injection of plasma and leads to bright auroral displays and associated disturbances to ground-based magnetometers—the auroral substorm [Akasofu, 1964]. Since intervals that are less than an hour of southward IMF occur naturally in the solar wind, substorms occur on a daily basis [Borovsky et al., 1993b].

Substorms have a geomagnetic impact, but mostly in the auroral region. A geomagnetic storm may develop if the solar wind magnetic field sustains southward for a longer period of time (hours) [Gonzalez et al., 1994, Russell, 2001]. Different from the substorms, geomagnetic storms have more impact on low-latitude regions. Storms are characterized by energization of the radiation belts and enhanced ring current, which cause a significant depression in the equatorial magnetic field, measured by the Dst index, for example. The corresponding solar wind conditions correspond to events like Coronal Mass Ejections (CMEs) and Corotating Interaction Regions (CIRs) [Gonzalez et al., 1999], which can both provide long intervals of southward IMF [Forbes, 2000, Tsurutani et al., 2006]. CMEs are responsible for the largest geomagnetic disturbances, with the storm size depending on the solar wind speed, the field strength, and the southward component of the magnetic field [Gosling et al., 1991, Richardson et al., 2001].

1.2.4 Space Weather Impacts

The impacts of space weather on the near-Earth environment can be divided into three major categories. First, the high-energy protons and heavy ions arriving at the near-Earth environment could damage microminiaturized electronics that can disrupt sensitive space systems, see Figure 1.9(a). The result can be damaging to satellite solar power panels, confusion to optical tracker systems, and scrambling of spacecraft command and control software. Solar Energy Particle (SEP) events can also be life-threatening for astronauts in space [Turner et al., 2000]. Second, relativistic electrons can also be harmful. As shown in Figure 1.9(b), these high-energy electrons can penetrate the shielding of the spacecraft and can bury themselves within dielectric materials. When this charge has built up, a powerful electrical discharge can cause spacecraft failures [Vampola, 1987]. Third, "surface charging" as another space weather phenomenon is illustrated by Figure 1.9(c). Electrical charges coming from 10-100 kV electrons within Earth's magnetosphere can accumulate on the surfaces of satellites. If enough charge builds upon a region of surface dielectric material,

there can be a powerful, disruptive discharge [Robinson and Behnke, 2001].

Space weather can also have impact on the near-Earth environment, but also it can have severe effects on the surface of the Earth. Geomagnetic storms can impact the operational reliability of electric power grids. For example, a major storm in 1989 shut down the Hydro Quebec power system in Canada for many hours. The power grids are disrupted by the geomagnetically induced currents (GICs) caused by the geomagnetic storms. The GICs flow through transformers and power lines, and the accumulative effect applied to the power grid facilities can cause economic loss [Kappenman, 2001]. Moreover, a major geomagnetic storm can modify the ionosphere of Earth and therefore can disrupt high frequency radio communication. This is a problem for the military and airlines that are attempting to communicate with aircraft flying transpolar routes. Space weather can also cause sudden heating of Earth's upper neutral atmosphere. This heating causes an expansion of the upper atmospheric layer (the thermosphere), which can suddenly increase the drag force on low-altitude spacecraft [Lanzerotti, 2001, Song et al., 2001]. Recently, SpaceX lost 40 of 49 satellites one day after launch due to a geomagnetic storm on February 3, 2022.

1.3 Motivations and Outline of the Dissertation

1.3.1 Motivations

Space weather closely impacts to human society, and understanding it better would help us not only gain new knowledge in the solar-terrestrial system but also contribute to mitigating its negative impacts on human activities. There are several open questions on this topic that also serve as the major motivation of this dissertation work:

1. Can we incorporate kinetic physics into a global MHD model and use it to simulate geomagnetic storm events?

2. Does kinetic physics have global-scale effects? If so, how does it affect the global

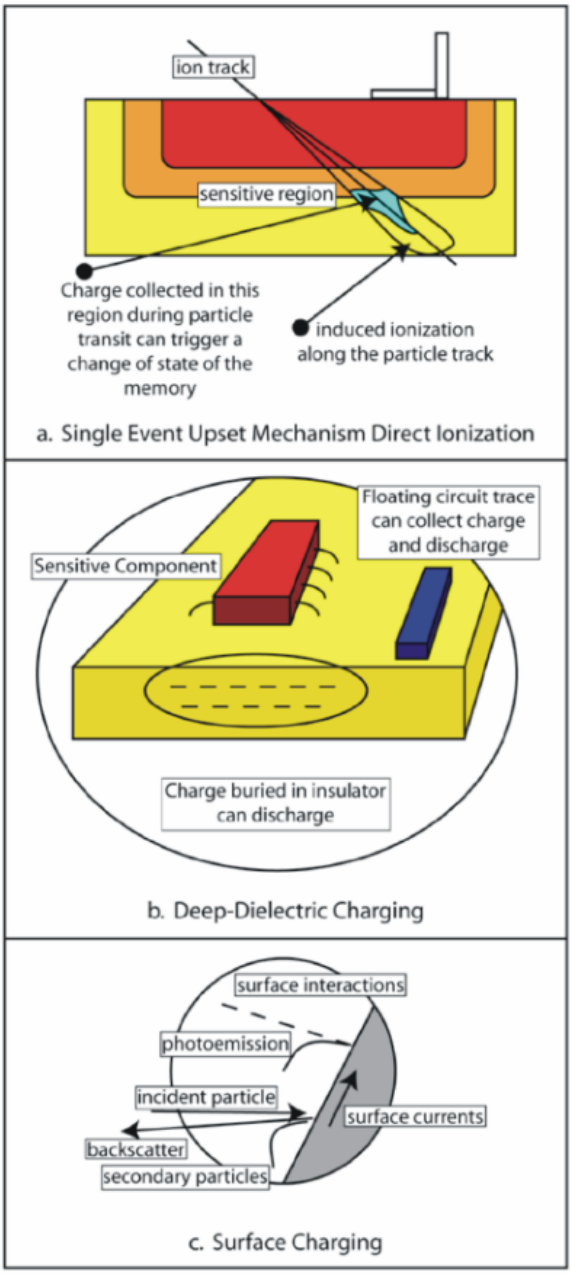

Figure 1.9: A diagram illustrating space environment effects due to (a) Ions causing single-event upsets, (b) deep-dielectric charging, and (c) surface charging [Baker, 1998].

configuration of the Earth's magnetosphere?

3. Can we utilize machine learning methods and the massive data coming from the current generation of space missions to provide a better forecast of solar flares?

1.3.2 Outline of the Dissertation

This dissertation contains my response to the presented open questions. Chapter 2 describes the models used in the dissertation. Chapter 3 presents the simulation of a geomagnetic storm event using the newly developed MagnetoHydroDynamics with Adaptively Embedded Particle-In-Cell (MHD-AEPIC) model. The results on kinetic scale, mesoscale and global scale are discussed. Chapter 4 shows how kinetic reconnection affects the global magnetosphere configuration when the solar wind driving is strong and constant. We also conduct simulations for the same event without the kinetic model to better understand the role of reconnection physics. In Chapter 5, we present a machine learning based solar flare forecasting model using the HMI observational data in the past ten years. The influence of the solar cycle variation is also discussed in this chapter. At the end, there is a summary and discussion of future work.

CHAPTER 2

Model Description

In this chapter, we describe the models used in this dissertation. We start with introducing the **Space Weather Modeling Framework (SWMF)** [Tóth et al., 2012], which is the framework containing multiple components for the geospace modeling. Next we describe the magnetohydrodynamics (MHD) model **BATS-R-US (Block Adaptive Tree Solar-wind Roe-type Upwind Scheme)** that serves as the global magnetosphere (GM) component in the SWMF. The particle-in-cell model **FLexible Exascale Kinetic Simulator (FLKES)** is described afterwards, which is the kinetic particle-in-cell (PC) component in the SWMF. The two models are coupled together with the **MHD with adaptively embedded Particle-in-Cell (MHD-AEPIC)** algorithm. The machine learning models are presented in the last section of this chapter.

2.1 Space Weather Modeling Framework

The Space Weather Modeling Framework (SWMF) is a software framework that couples multiple physics-based numerical models for simulating space weather and space physic processes on a wide range of spatio-temporal scales. Each physics domain in the SWMF corresponds to a component. Each component is represented by one or more component versions. A component version is a physics model plus the appropriate wrappers and couplers. The components are compiled into libraries, and they are linked to the core of the framework and the shared libraries to form a single executable. The SWMF distributes the components over

a parallel machine, and executes and couples them in an efficient manner [Tóth, 2006] using the Message Passing Interface (MPI) library for communication. Furthermore, the physics models can also be compiled into individual executables and used as stand-alone codes. See Figure 2.1 for general structure of the SWMF.

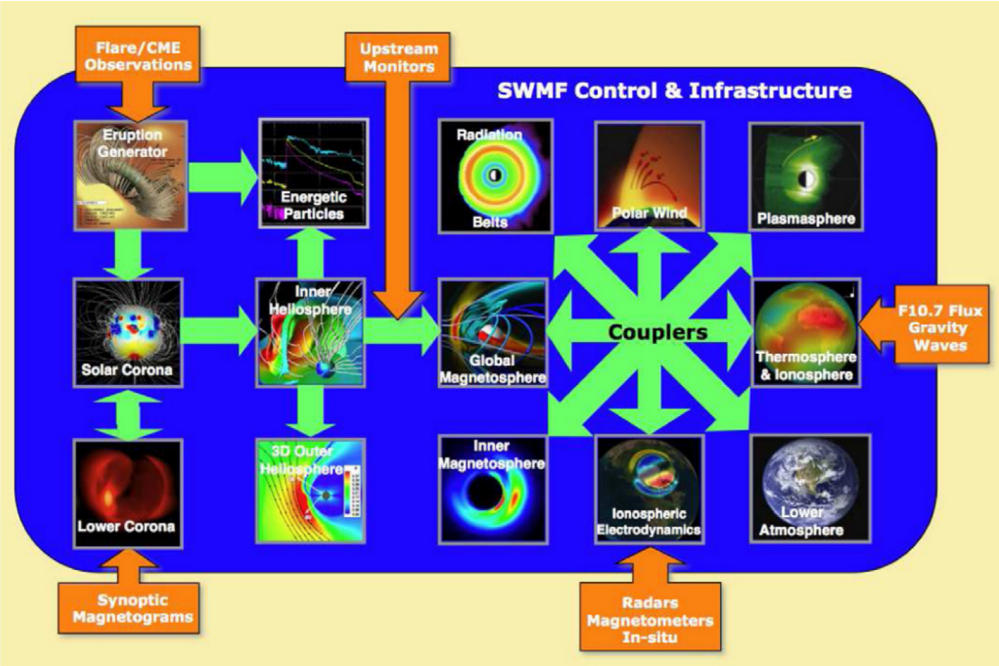

Figure 2.1: Components (boxes) and their couplings (green arrows) in the Space Weather Modeling Framework. External input is indicated by the orange arrows.

2.2 MHD model: BATS-R-US

The Block-Adaptive-Tree Solarwind Roe-type Upwind Scheme (BATS-R-US) [Powell et al., 1999a, De Zeeuw et al., 2000] is a multi-physics MHD code that has been continuously developed at the University of Michigan for over two decades. The BATS-R-US model is the most important component in the SWMF, which has been applied to simulate multi-scale space physics systems including, but not limited to, the solar corona, the heliosphere, planetary magnetospheres, moons, comets and the outer heliosphere. The BATS-R-US supports **adaptive mesh refinement (AMR)** that enables multi-scale physics simulations. For the purpose of running efficiently, the code is using a 3-D block-adaptive mesh with MPI

parallelization [Stout et al., 1997, De Zeeuw et al., 2000]. The original block-adaptive mesh is replaced with the generalized and redesigned **Block Adaptive Tree Library (BATL)** by Tóth et al. [2012]. This library is designed for creating, adapting, load-balancing and message-passing a 1, 2, or 3 dimensional block-adaptive grid in generalized coordinates. The size of the adaptive block is an important parameter for the code efficiency. Smaller blocks allow precise grid adaptation, but a large number blocks introduces more storage and computation spent on ghost cells. Larger blocks reduce the total number of ghost cells surrounding the grid blocks, but make the grid adaptivity less efficient. The typical choice of block size in 3D ranges between 4^3 to 16^3 grid cells, with an additional 1-3 layers of ghost cells on each side depending on the order of the numerical scheme.

In addition to the adaptive block feature, the BATS-R-US has been continuously developed to include new schemes as well as new physical models. Currently, there are 60 equation sets from ideal hydrodynamics to the recent six-moment MHD model [Huang et al., 2019]. For simulating space plasma, magnetohydrodynamic (MHD) equations are mostly used, including resistive, Hall, semi-relativistic, multi-species and multi-fluid MHD, optionally with anisotropic pressure, radiative transport and heat conduction. The choices for numerical schemes vary from the Roe scheme to many others, including Rusanov and HLLE, combined with a second order total variation diminishing (TVD) scheme or a fifth order accurate conservative finite difference scheme of [Chen et al., 2016b]. The time discretization can be explicit, point- implicit, semi-implicit, or fully implicit.

2.2.1 Hall MHD with Electron Pressure Equations

The equation set of the geospace simulations in this dissertation is the Hall MHD with electron pressure equations [Tóth et al., 2008]. As an extension to the ideal and resistive MHD model, the electron and ion motions are decoupled in the Hall MHD equations by

including the Hall term in the generalized Ohm's law:

$$\mathbf{E} = -\mathbf{u} \times \mathbf{B} + \eta \mathbf{J} + \frac{1}{ne}\mathbf{J} \times \mathbf{B} - \frac{\nabla p_e}{ne} \tag{2.1}$$

where the first term on the right-hand-side is the convection term, the second term is the resistive term, the third term is the Hall term, and the fourth term is the electron pressure gradient term. Here we use a scalar electron pressure, that is the simplest approximation for the electron pressure tensor. The entire set of equations is:

$$\begin{aligned}
\frac{\partial \rho}{\partial t} &= -\nabla \cdot (\rho \mathbf{u}) && (2.2)\\
\frac{\partial (\rho \mathbf{u})}{\partial t} &= -\nabla \cdot \left[\rho \mathbf{u}\mathbf{u} + (p + p_e)\bar{I} + \frac{B^2}{2\mu_0}\bar{I} - \frac{\mathbf{B}\mathbf{B}}{\mu_0} \right] && (2.3)\\
\frac{\partial \epsilon}{\partial t} &= -\nabla \cdot \left[(\epsilon_h + p)\mathbf{u} + p_e \mathbf{u}_e + \mathbf{u}_e \cdot \left(\frac{\mathbf{B}^2}{\mu_0}\bar{I} - \frac{\mathbf{B}\mathbf{B}}{\mu_0} \right) \right] + p_e \nabla \cdot \mathbf{u}_e && (2.4)\\
\frac{\partial \mathbf{B}}{\partial t} &= -\nabla \times \left[-\mathbf{u}_e \times \mathbf{B} - \frac{\nabla p_e}{ne} \right] && (2.5)\\
\frac{\partial p_e}{\partial t} &= -\nabla \cdot (p_e \mathbf{u}_e) - (\gamma - 1) p_e \nabla \cdot \mathbf{u}_e && (2.6)
\end{aligned}$$

where $\bar{I}$ is the identity matrix, ρ is the mass density, $\mathbf{u}$ is the plasma bulk velocity, $\mathbf{B}$ is the magnetic field, p_e is the electron pressure, p is the ion pressure and $\mathbf{j} = \nabla \times \mathbf{B}/\mu_\mathbf{0}$ is the current density. The Hall velocity and electron bulk velocity are defined as

$$\begin{aligned}
\mathbf{v}_H &= -\frac{\mathbf{j}}{ne} = -\frac{M_i}{e}\frac{\mathbf{j}}{\rho} && (2.7)\\
\mathbf{u}_e &= \mathbf{u} + \mathbf{v}_H && (2.8)
\end{aligned}$$

where $n = \rho/M_i$ is the number density, M_i is the ion mass, and e is the elementary charge. The total energy density is defined as

$$\epsilon = \epsilon_h + \frac{B^2}{2\mu_0} = \frac{1}{2}\rho \mathbf{u}^2 + \frac{p}{\gamma - 1} + \frac{\mathbf{B}^2}{2\mu_0} \tag{2.9}$$

where $\epsilon_h = \rho \mathbf{u}^2/2 + p/(\gamma - 1)$ is the hydrodynamic energy density of the ions and $\gamma = 5/3$ is the adiabatic index. The thermal energy density of the electrons is $\epsilon_e = p_e/(\gamma - 1)$. We note that the $e + \epsilon_e$ is conserved both analytically and numerically as the non-conservative source terms $\pm p_e \nabla \cdot \mathbf{u}$ in equations (2.4) and (2.6) cancel out. Apart from $(\rho, \mathbf{u}, \mathbf{B}, p, p_e)$, other variables are derived quantities.

2.3 MHD with Adaptively Embedded Particle-In-Cell (MHD-AEPIC) model

MHD models are efficient in simulating global magnetospheres. However, the underlying assumption, which is the MHD description of plasma is not valid for phenomena involving kinetic physics, such as magnetic reconnection. Particle-in-cell (PIC) methods have been demonstrated as a powerful tool to study kinetic physics. But the PIC codes are so computationally expensive that it is still extremely difficult to do global simulations [Lapenta, 2012]. In this section, we will describe the PIC model we are using in this dissertation and how we combine the efficiency of the MHD model and the physics capability of the PIC code [Daldorff et al., 2014].

2.3.1 Particle-in-cell Method

There are two sets of equations in the PIC model. First, the motion of macro-particles satisfying the Vlasov equation is solved by:

$$\frac{\mathrm{d}\mathbf{x}_p}{\mathrm{d}t} = \mathbf{v}_p \tag{2.10}$$

$$\frac{\mathrm{d}\mathbf{v}_p}{\mathrm{d}t} = \frac{q_p}{m_p}(\mathbf{E}_p + \mathbf{v}_p \times \mathbf{B}_p) \tag{2.11}$$

where $\mathbf{x}_p$ is the particle position and $\mathbf{v}_p$ is the particle velocity, $\mathbf{E}_p$ and $\mathbf{B}_p$ are the electromagnetic field values interpolated at the particle position. Second, the electric field $\mathbf{E}$ and

the magnetic field $\mathbf{B}$ is solved from the Maxwell equations:

$$\nabla \cdot \mathbf{E} = \frac{\rho_c}{\epsilon_0} \tag{2.12}$$

$$\nabla \cdot \mathbf{B} = 0 \tag{2.13}$$

$$\nabla \times \mathbf{E} = -\frac{\partial \mathbf{B}}{\partial t} \tag{2.14}$$

$$\nabla \times \mathbf{B} = \mu_0 \epsilon_0 \frac{\partial \mathbf{E}}{\partial t} + \mu_0 \mathbf{J} \tag{2.15}$$

where the current density $\mathbf{J}$ and charge density ρ_c are interpolated from the particle to the grid cells. The PIC model is using a 3-D Cartesian grid. The electric field $\mathbf{E}$ and the current density $\mathbf{J}$ are stored at the vertices of the grid. Meanwhile, the magnetic field $\mathbf{B}$ and charge density ρ are stored on the cell centers. Figure 2.2 shows the field storage on a single grid cell.

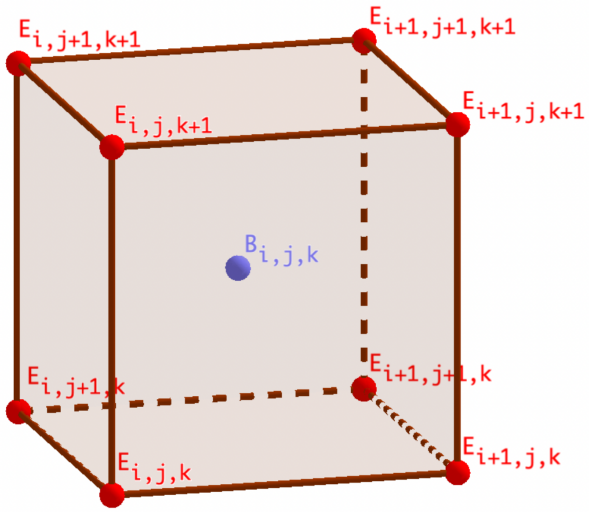

Figure 2.2: Staggered field storage in the PIC algorithm for cell index (i, j, k). The electric field $\mathbf{E}$ and the current density $\mathbf{J}$ are stored at the vertices of the grid. Meanwhile, the magnetic field $\mathbf{B}$ and charge density ρ_c are stored at the cell centers.

2.3.2 Gauss's Law Satisfying Energy Conserving Semi-Implicit Method

The Gauss's Law satisfying Energy Conserving Semi-Implicit Method (GL-ECSIM) is the numerical scheme used to solve the PIC equations. The original Energy Conserving Semi-Implicit Method (ECSIM) was published by Lapenta [2017]. Chen and Tóth [2019] improved the ECSIM with better stability, charge conservation, particle splitting and merging algorithm. The key steps of the method are presented as follows.

The macro particles with position $\mathbf{x}_p$ and velocity $\mathbf{v}_p$ are updated explicitly via

$$\mathbf{x}_p^{n+1/2} = \mathbf{x}_p^{n-1/2} + \Delta t \mathbf{v}_p^n \tag{2.16}$$

$$\mathbf{v}_p^{n+1} = \mathbf{v}_p^n + \frac{q_p \Delta t}{m_p}\left[\mathbf{E}^{n+\theta} + \frac{\mathbf{v}_p^n + \mathbf{v}_p^{n+1}}{2} \times \mathbf{B}^n\right] \tag{2.17}$$

where a leapfrog scheme is used to update the particle's position and velocity. The electric field at time step $n+\theta$ and the magnetic field at time step n is used to update the particles [Lapenta, 2012].

The electromagnetic fields are updated through an implicit scheme:

$$\frac{\mathbf{B}^{n+1} - \mathbf{B}^n}{\Delta t} = -c\nabla \times \mathbf{E}^{n+\theta} \tag{2.18}$$

$$\frac{\mathbf{E}^{n+1} - \mathbf{E}^n}{\Delta t} = -c\nabla \times \mathbf{B}^{n+\theta} - 4\pi\bar{\mathbf{J}} \tag{2.19}$$

where $\bar{\mathbf{J}}$ is the predicted current at $n+\frac{1}{2}$ time stage that depends on the unknown electric field $\mathbf{E}^{n+\theta}$. The values at time step $n+\theta$ is defined as weighted linear combinations of values at time step n and $n+1$:

$$\mathbf{E}^{n+\theta} = (1-\theta)\mathbf{E}^{n} + \theta\mathbf{E}^{n+1} \tag{2.20}$$

$$\mathbf{B}^{n+\theta} = (1-\theta)\mathbf{B}^{n} + \theta\mathbf{B}^{n+1} \tag{2.21}$$

expressing $\mathbf{B}^{n+\theta}$ from Faraday's law [2.18] and substituting to Ampere's law [2.19] results in an equation that only contains the electric field as unknowns:

$$\mathbf{E}^{n+\theta} + \delta^2\left[\nabla(\nabla\cdot\mathbf{E}^{n+\theta}) - \nabla^2\mathbf{E}^{n+\theta}\right] = \mathbf{E}^{n} + \delta\left(\nabla\times\mathbf{B}^{n} - \frac{4\pi}{c}\bar{\mathbf{J}}\right) \tag{2.22}$$

where $\delta = c\theta\Delta t$. The exact energy conservation can be achieved when $\theta = 0.5$. However, Chen and Tóth [2019] found that it will still create numerical waves, so $\theta = 0.51$ is used in our simulations. After the field solver, the particles are moved to/towards the positions that satisfies Gauss's law. Since the particle displacement will not change the electromagnetic field and the particle velocities, the energy is still conserved. The new particle locations modify the mass density that reduces the error in Gauss's law.

2.3.3 FLexible Exascale Kinetic Simulator (FLEKS)

The described PIC algorithms are implemented in the model FLexible Exascale Kinetic Simulator (FLEKS) by Chen et al. [2021]. Compared to the existing particle-in-cell model with GL-ECSIM algorithm, FLEKS introduces the adaptive grid feature that brings much more flexibility to cover the regions of interest. For example, if a box-shaped PIC domain is used to cover the dayside magnetopause, the box will cut through the planet and introduce difficulties to the PIC model. Also, the PIC model will cover a large area where kinetic effects are not important. A flexible PIC region resembles a paraboloid shape to cover the magnetopause will solve this problem. The dynamic adaptive PIC grid is also helpful to improve efficiency. For instance, the magnetotail current sheet may exhibit a flapping motion during a geomagnetic storm because of the transverse IMF components. If the PIC grid is

fixed through the entire simulation, a large enough box is required that is not affordable with current computational resources. However, if the PIC grid can dynamically switch on/off a portion of its cells so that it only covers the location where magnetic reconnection may happen, a substantial amount of computational time will be saved.

To implement this adaptive grid feature, FLEKS uses the parallel data structure provided by the AMReX library [Zhang et al., 2019]. FLEKS still requires the shape of the full PIC grid to be a box, as well as an uniform Cartesian grid that is a requirement of the GL-ECSIM algorithm. However, FLEKS splits the whole computational domain into a number of patches, each patch contains N ($N \geq 2$) cells on each direction. $N = 1$ is not allowed because FLEKS requires two layers of ghost cells to couple with the MHD model. If $N = 1$, ghost cells from two different patches may overlap with each other that introduces difficulty in determining the ghost cell values. In the MHD-AEPIC simulation, the MHD model controls the status of the patches based on the geometric and physics-based criteria. The MHD model sends a bit-wise patch status array to FLEKS through the Message Passing Interface (MPI). The bit-wise array reduces the size of this array substantially (proportional to N^{-3} in 3D). In this dissertation, we use the word "active" to describe the PIC patches that are turned on. Figure 2.3 shows an example of a PIC domain with two active PIC patches.

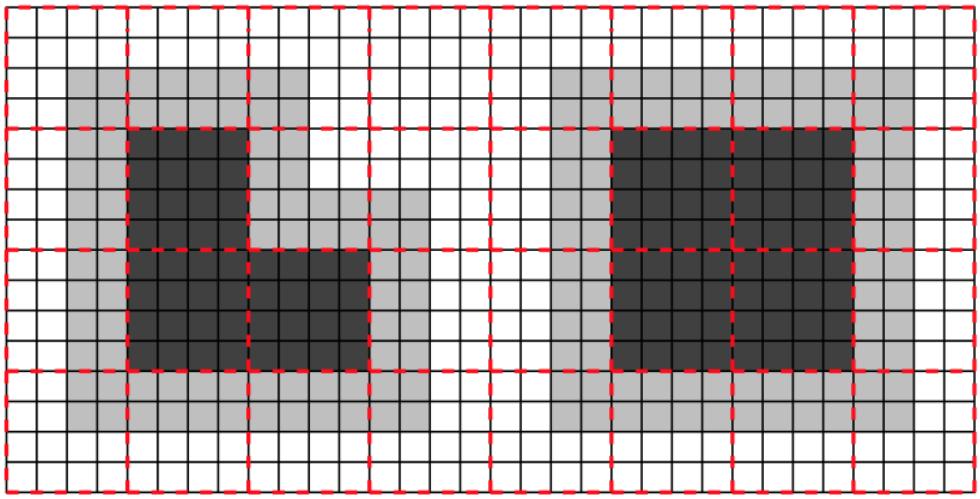

Figure 2.3: The black lines represent the PIC cells. The red dashed lines show the patches, and one patch contains 4×4 cells in this example. The active patches/cells are colored by dark gray, and light gray area represents the ghost cells of the active PIC regions [Chen et al., 2021].

In addition to the adaptive grid feature, there are other improvements in the FLEKS, such as the adaptive time stepping, particle resampling, and the test particle module. More details can be found in the original paper [Chen et al., 2021].

2.3.4 Two-way Coupling between MHD and PIC Models

Developed by Daldorff et al. [2014], the MHD model and the PIC model can be two-way coupled together through the SWMF with the Embedded Particle-In-Cell (MHD-EPIC) algorithm. This model requires the PIC region to be a fixed rectangle box that has been successfully applied to many planetary magnetospheric simulations, such as Mercury [Chen et al., 2019b], Earth [Chen et al., 2017, 2020, Tóth et al., 2017], Mars [Ma et al., 2018] and Ganymede [Tóth et al., 2016, Zhou et al., 2019, 2020a].

Figure 2.4 shows the temporal discretization of the MHD-EPIC coupling algorithm. As mentioned in 2.3.3, a fixed PIC box can introduce limitations in many applications. In this dissertation, we improve the MHD-EPIC to MHD with Adaptively Embedded PIC (MHD-AEPIC) that allows the PIC region to be adaptive, and provide simulation results using this

new model. The MHD-AEPIC still uses the same temporal discretization as the MHD-EPIC in the coupling, but now the shape of the PIC region can be arbitrary. More details can be found in Chapter 3.

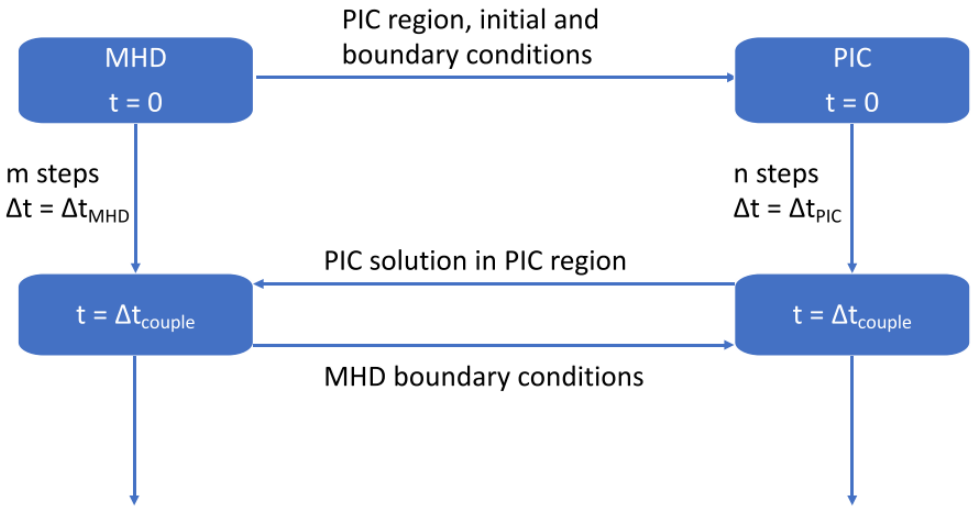

Figure 2.4: Temporal discretization of the MHD-EPIC coupling algorithm [Daldorff et al., 2014].

2.4 Machine Learning Methodology

The development of artificial intelligence (AI) is almost a cyclical repetition of springs and winters. In the past decade, people gradually believed that we are experiencing a new AI spring, when the AI has finally entered industrial production. The hype and disillusionment, though interesting, will not be discussed in this dissertation. Machine learning is a type of artificial intelligence (AI) that allows the "trained" models to predict outcomes without being explicitly programmed to do so. In other words, machine learning algorithms use historical data as input to predict new output values. In this section, we will describe the general concepts of machine learning. The details of the specific model we used in solar flare prediction can be found in Chapter 5.

2.4.1 Supervised Learning

Supervised learning is a type of machine learning method that is used when both the input and target values are available. The model is "supervised" by the observed target values during the training process. Depending on the type of target values, there are two types of supervised learning models: supervised regression and supervised classification. In Chapter 5, we use the supervised learning method to forecast solar flare classes.

2.4.1.1 Supervised Regression

The supervised regression is used to find a map between a set of multidimensional input $\mathbf{x} = (x_1, x_2, \ldots, x_{N_i})$ and its corresponding scalar output y,

$$y = f(\mathbf{x}) + \epsilon \tag{2.23}$$

where $f : \mathbb{R}^{N_i} \to \mathbb{R}$ is a mapping function and ϵ is a stochastic error term. The i^{th} observational data point is noted as $\{\mathbf{x}^i_{\text{obs}}, y^i_{\text{obs}}\}$. No matter what assumptions we make on the function f and on the error term ϵ, this problem can be understood as an optimization problem. In fact, any regression problem can be set up as finding the unknown map f that minimizes a given cost function. The cost function is computed with the difference between the observational values y^i_{obs} and the predictions $\hat{y}^i = f(\mathbf{x}^i_{\text{obs}})$ for a certain number of training data $i = 1, 2, \ldots, N_T$. Examples of cost functions are the mean squared error $\text{MSE} = \frac{1}{N_T}\sum_{i=1}^{N_T}(\hat{y}^i - y^i_{\text{obs}})^2$ and the mean absolute error $\text{MAE} = \frac{1}{N_T}\sum_{i=1}^{N_T}|\hat{y}^i - y^i_{\text{obs}}|$.

The input $\mathbf{x}$ and the output y can be taken as quantities observed at the same time, in which case the problem is referred to as nowcasting, or with a time lag, which is the forecasting. In principle a supervised regression task can be successfully applied to any problem for which there is a (physically motivated) reason to infer some time-lagged causality between a set of drivers and an output of interest.

2.4.1.2 Supervised Classification

The supervised classification model answers the question: What class does an input belong to? In practice, by introducing arbitrary thresholds and dividing the range of predictions into "classes", any regression problem for a continuous variable can be simplified into a classification task. The forecast of the solar flare classes is a good example for this kind of task. The classification into A, B, C, M, and X classes is based on the measured peak flux in (W/m^2) arbitrarily divided in a logarithmic scale. The classification is different from regression in the definition of cost functions and discrete output. For instance, a regression output z can be interpreted as the probability of the associated event being true or false (in a binary classification setting), by inputting the real value through a logistic function:

$$\hat{y} = \sigma(z) = \frac{1}{1 + e^{-z}} \tag{2.24}$$

and a simple and effective loss function is the cross-entropy:

$$C(y, z) = (y - 1)\log(1 - \sigma(z)) - y\log(\sigma(z)) \tag{2.25}$$

where y is the ground truth value (0 or 1) and z is the model output. It is easy to verify that C diverges to ∞ when $|y - \hat{y}| = 1$ which refers to the sample is wrongly classified, and it approaches to 0 when $|y - \hat{y}| = 0$, which means that the sample is correctly classified.

CHAPTER 3

Global Magnetohydrodynamic Magnetosphere Simulation with an Adaptively Embedded Particle-in-cell Model

This chapter as well as Appendix are adapted from a manuscript currently under review by the *Journal of Geophysical Research: Space Physics*. The introduction to MHD equations in section 3.2.1 is moved to Chapter 2 in this dissertation.

3.1 Introduction

A geomagnetic storm is a major disturbance of Earth's magnetosphere that occurs when a significant amount of energy is deposited into the geospace. The most widely used and successful simulation tools to study the geomagnetic storms are based on the magnetohydrodynamic (MHD) description, which is computationally feasible to solve. The first global MHD models were developed in the 1980s [LeBoeuf et al., 1981, Wu et al., 1981, Brecht et al., 1981, 1982]. Later on, models with more advanced numerical algorithms have been developed, such as the Lyon-Fedder-Mobarry (LFM) [Lyon et al., 1986, 2004], the OpenGGCM [Raeder et al., 1995, 1996] and the GUMICS (Grand Unified Magnetosphere Ionosphere Coupling Simulation) model [Janhunen, 1996].

In this paper, we use the University of Michigan's Space Weather Modeling Framework

(SWMF [Tóth et al., 2012]) which also includes an MHD model, the Block Adaptive-Tree Solar-wind Roe-type Upwind Scheme (BATS-R-US) [Powell et al., 1999b] as its global magnetosphere (GM) component. The SWMF has been applied to many storm event simulations [Tóth et al., 2007, Glocer et al., 2009, Haiducek et al., 2017], and it has also been selected as the physics-based model at the NOAA Space Weather Prediction Center based on a thorough model comparison [Pulkkinen et al., 2013].

Magnetic reconnection plays a key role in the magnetosphere both at the dayside and in the tail. Despite all the successful applications MHD models have achieved, magnetic reconnection in the global MHD models relies on either Hall resistivity, ad hoc anomalous resistivity, or simply numerical diffusion. The numerical diffusion plays an important role in both ideal and Hall MHD models because it is required to break the field lines. As we show in Appendix , the reconnection rate remains finite when the grid resolution becomes finer. The Hall resistivity, although does not break the field lines that are frozen into the electron fluid, changes the structure of the reconnection region, which can lead to faster reconnection rate than ideal MHD [Birn et al., 2001a]. A current dependent anomalous resistivity has also been applied in MHD simulations [Raeder et al., 2001]. However, none of these approximations truly describe the physical processes responsible for collisionless reconnection. It is very important to properly represent kinetic reconnection physics in a global simulation and check if it plays an important role in contributing to the larger scale processes that eventually produce geomagnetic disturbances and space weather effects. Furthermore, the MHD approximation assumes that the distribution functions of the ions and electrons are Maxwellian. Numerous observations suggest that this condition is violated especially near the magnetic reconnection sites [Chen et al., 2016a, Burch et al., 2016a, Hwang et al., 2019, Lotekar et al., 2020].

The MHD with embedded Particle-In-Cell (MHD-EPIC) model [Daldorff et al., 2014] enables kinetic physics to be introduced into a global MHD model. The MHD-EPIC model has been successfully used to study the interaction between the Jovian corotating plasma

and Ganymede's magnetopshere [Tóth et al., 2016, Zhou et al., 2019, 2020a]; flux transfer events (FTEs) at the Earth's dayside magnetopause [Chen et al., 2017]; Mars' magnetotail dynamics [Ma et al., 2018] and the dawn-dusk asymmetries discovered at the Mercury's magnetotail [Chen et al., 2019b]. However, the iPIC3D [Markidis et al., 2010] code, which is the PIC model used in the MHD-EPIC simulations, can only run on a fixed Cartesian grid. The magnetotail (and the associated current sheet that contains the reconnection sites) typically exhibits a flapping motion [Tsutomu and Teruki, 1976, Volwerk et al., 2013] during a geomagnetic storms. Covering the whole domain of interest where reconnection can occur in the magnetotail would require a very large PIC grid and would result in a massive computational cost. This may be feasible for a short simulation time (up to an hour or so) but for geomagnetic storms that usually happen and last for days, the computational cost would become prohibitive.

To tackle this problem, we have developed the MHD with Adaptively Embedded PIC (MHD-AEPIC) algorithm that allows smaller PIC region than MHD-EPIC, which saves computational resources. Shou et al. [2021] introduces this idea and verifies that covering part of the simulation domain with a dynamically moving PIC box gives the same solution as using alarger fixed PIC domain, while running significantly faster. This justifies our effort to use an adaptive PIC region in the simulation. In this paper, we further improve this method and make it more flexible: 1. The size and shape of the active PIC regions can be adapted during the runtime; 2. The adaptation of the active PIC region is fully automatic. To realize the first feature, instead of iPIC3D, we use the FLexible Exascale Kinetic Simulator (FLEKS) [Chen et al., 2021] as the PIC model. FLEKS inherits all numerical algorithms from MHD-EPIC, and also accommodates an adaptive PIC grid that allows PIC cells to be turned on and off during the simulation. In addition, FLEKS employs a particle splitting and merging scheme to improve the simulation efficiency and accuracy. FLEKS is described in more detail in Section 3.2.2.

We have developed a reliable and efficient algorithm to identify potential reconnection

sites in the magnetotail using three local criteria. The criteria are easy to compute and provide the information to the FLEKS code to adapt its grid to cover the reconnection sites. This newly developed MHD-AEPIC model is applied to simulate a magnetic storm. The SWMF simulation involves BATSRUS, FLEKS, the ionosphere electrodynamics model RIM [Ridley et al., 2004] and the inner magnetosphere model RCM [Wolf et al., 1982, Toffoletto et al., 2003]. This is the first simulation of a real event with kinetic reconnection physics in the magnetotail scaling from the global scales of the magnetosphere to the electron scales near the reconnection sites.

In this paper, we employ the new model to simulate the magnetic storm of 2011-08-05. We cover the tail reconnection sites with the adaptive PIC model. We also perform ideal MHD and Hall MHD simulations for comparison. All simulations are fully coupled with the inner magnetosphere and ionospheric electrodynamics models within the Space Weather Modeling Framework. We focus on the impact of using ideal MHD, Hall MHD and MHD-AEPIC physics on the dynamical processes in the magnetotail. To make the comparison straightforward, we use the ideal MHD model at the dayside in all three simulations.

The computational methods are described in Section 3.2, the demonstration of the adaptation feature and comparisons between models and observations are shown in Section 3.3 and we summarize in Section 3.4.

3.2 Methods

3.2.1 Global Magnetosphere Model: BATS-R-US

The Block-Adaptive Tree Solar-wind Roe-type Upwind Scheme (BATS-R-US) is used as the Global Magnetosphere (GM) model in our simulation. In the Hall MHD and MHD-AEPIC simulations in this paper, the Hall MHD equations [Tóth et al., 2008] are solved. The Hall term is handled with a semi-implicit scheme. The spatial discretization uses a 2nd order accurate TVD scheme with the Artificial Wind Riemann solver [Sokolov et al., 1999] and the

Koren limiter [Koren, 1993] with $\beta = 1.2$. The hyperbolic cleaning [Dedner et al., 2003] and eight-wave scheme [Powell et al., 1999b] are used to keep the magnetic field approximately divergence-free.

The Hall MHD equations with a separate electron pressure equation are decribed in the Chapter 2. The continuity equation 2.2, momentum equation 2.3, energy equation 2.4 and electron pressure equation 2.6 are solved with an explicit time stepping scheme. In the induction equation 2.5, the convection term $\mathbf{u} \times \mathbf{B}$ and pressure gradient term $\nabla p_e/ne$ are solved using an explicit scheme, while the Hall term $\mathbf{v}_H \times \mathbf{B}$ is advanced with an implicit scheme. The Hall MHD equations introduce whistler mode wave, which has a characteristic wave speed inversely proportional to the wavelength. The shortest wavelength that exists in a numerical simulation is proportional to the cell size Δx, so the fastest whistler wave speed in a simulation is proportional to $1/\Delta x$. The time step in a fully explicit scheme is limited by the Courant-Friedrichs-Lewy (CFL) condition: $\Delta t < \Delta x/c_{\max}$, where $c_{\max}$ is the fastest wave speed, which leads to a time step proportional to $1/(\Delta x)^2$. We use a semi-implicit scheme [Tóth et al., 2012] to handle the stiff Hall term in the induction equation, so that the time step of the explicit part is only limited by the fast magnetosonic wave speed instead of the whistler speed.

A three-dimensional block-adaptive Cartesian grid is used to cover the entire computational domain $-224R_E < x < 32R_E$, $-128R_E < y, z < 128R_E$ in GSM coordinates. The Hall effect is restricted to $x \in [-100R_E, 20R_E], |y| < 30R_E$ and $|z| < 20R_E$ box region excluding a sphere of radius $3R_E$ centered at the Earth to speed up the simulation. Outside this region the Hall effect is neglected by setting $\mathbf{v}_H = 0$. In the magnetosphere, the smallest ion inertial length $d_i = c/\omega_{pi}$ is about $1/20\,R_E$ in the tail lobe region, which is already extremely difficult for a 3-D global MHD model to resolve, let alone the PIC code. Tóth et al. [2017] introduced a scaling approach which scales up the kinetic length by artificially increasing ion mass per charge by a scaling factor. The scaling does not change the fluid variables, such as density, pressure, velocity, IMF and dipole field, and the global structure

of the magnetosphere will not change significantly as long as the scaled up ion inertial length is much smaller than the global scales. In this paper, we use a factor of 16, which satisfies this condition. On the other hand, with the ion inertial length scaled up by 16 times, we don't need an extremely fine grid to resolve it. Wse set the grid cell size in the magnetotail to $\Delta x = 1/4R_E$, which is about 4 times smaller than the scaled up ion inertial length. About fourteen million cells are used in total.

At the inner boundary $r = 2.5R_E$, the density is calculated by the empirical formula $\rho_{\text{inner}} = (28 + 0.1\text{CPCP})$ amu/cm^3, where CPCP is the average of the northern and southern cross polar cap potentials measured in keV. This boundary condition has been used successfully in previous geomagnetic storm simulations [Pulkkinen et al., 2013]. The pressure and magnetic field $\mathbf{B}_1$ have zero gradient at the inner boundary, while the radial velocity is set to zero and the tangential velocity is calculated from the corotation and the $\mathbf{E} \times \mathbf{B}$ drift, where the electric field $\mathbf{E}$ is provided by the Ridley Ionosphere Model (RIM) [Ridley et al., 2004].

3.2.2 Particle-in-cell Model: FLEKS

The FLexible Exascale Kinetic Simulator (FLEKS) [Chen et al., 2021] is used as the particle-in-cell (PIC) model (PC component in the SWMF) to resolve kinetic physics. FLEKS uses the same two-way coupling method as MHD-EPIC [Daldorff et al., 2014] and the Gauss's law satisfying energy-conserving semi-implicit method (GL-ECSIM) [Chen and Tóth, 2019] for the PIC solver. To enable the adaptation in MHD-AEPIC, FLEKS introduces an adaptive grid that allows changing simulation region dynamically. Figure 3.1 shows a schematic plot of the adaptive grid. We choose $\Delta x = 1/4R_E$ to be the PIC grid resolution so that the scaled $d_i/\Delta x \sim 4$. The ion inertial length inside the magnetosphere is described in Subsection 3.2.1. The ion-electron mass ratio is set to 100 in this simulation so that the electron skin depth $d_e = 0.1d_i$. Li et al. [2019] perform 2-D PIC simulations using different ion-electron mass ratios and conclude that features like reconnection rate and magnetic energy conversion

are similar in simulations using different ion-electron mass ratios. Although the grid is not refined to resolve the electron scale, in the PIC model the electron particles can resolve sub-grid scale physics under the influence of the electromagnetic field that is resolved on the ion scale. Chen and Tóth [2019] show that the semi-implicit PIC model can reproduce the most important ion scale features of magnetic reconnection with such grid resolution. The selected resolution balances between the computational cost and the requirement of resolving kinetic scales.

FLEKS provides a particle merging and splitting scheme to maintain the number of particles per cell within bounds. Merging particles in a cell with high number of particles can improve load-balancing and speed up simulation, while splitting particles in a cell with few particles can reduce noise and improve accuracy for the PIC simulation. This feature is very useful keeping the number of particles per cell about uniform during a long geomagnetic storm simulation.

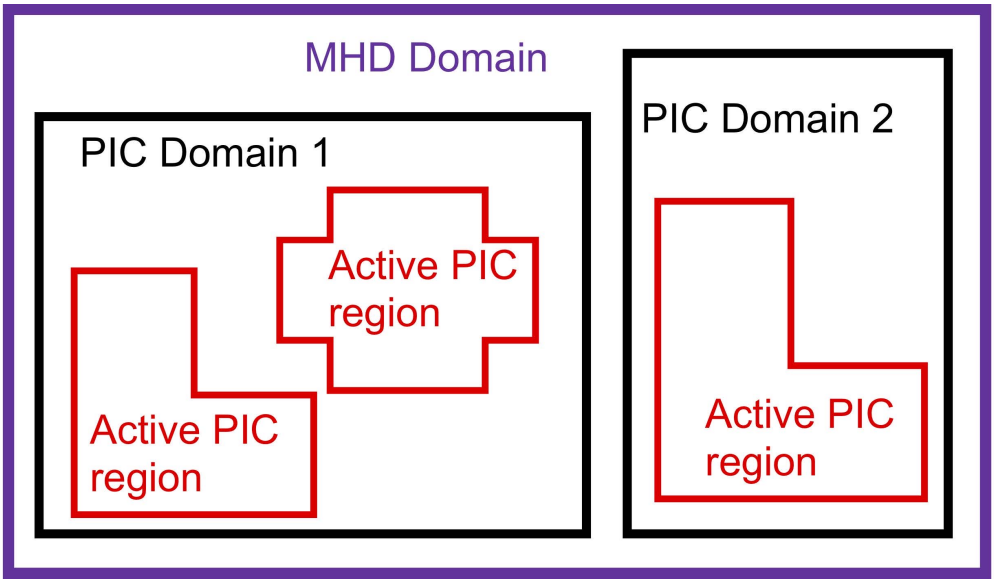

Figure 3.1: The schematic plot of the FLEKS adaptive grid. The red line boundary shows the flexibility of turning on and off the PIC patches during the simulation.

3.2.3 Selection Criteria of PIC Regions

As described in the previous section, FLEKS allows patches to be turned on and off during the simulation. To make the active PIC patches only cover the regions of interest, where magnetic reconnection is happening or will be triggered soon, the MHD model should locate these regions and pass this information to FLEKS. Finding the locations of magnetic reconnection sites can be done in various ways including tracing field lines [Glocer et al., 2016]. For sake of efficiency and generality, here we use local criteria based on the local MHD solution only.

Magnetic reconnection usually happens in current sheets where the current density j is strong and the magnetic field B is weak. In particular, the field $B_\perp$ that is perpendicular to the current $\mathbf{j}$ should be close to zero, while the guide field parallel to the current can be non-zero. We define the following non-dimensional relation as our first criterion

$$\frac{J\Delta x}{B_\perp + \varepsilon} = \frac{J^2\Delta x}{|\mathbf{J}\times\mathbf{B}| + J\varepsilon} > c_1 \tag{3.1}$$

where $\mathbf{J} = \mu_0\mathbf{j} = \nabla\times\mathbf{B}$ and ε is a small dimensional constant in units of the magnetic field introduced to avoid dividing by zero. We use $\varepsilon = 1\,\mathrm{nT}$ in our simulations presented here, which is much smaller than the typical magnetic field intensity in the tail current sheet. Δx is the local cell size that is used in calculating the curl of the magnetic field, so that $J\Delta x$ is the jump of the transverse magnetic field between neighboring grid cells. We set $c_1 = 0.8$ in this work to select the cells that are close to the reconnection sites.

While criterion (3.1) works quite well in general, we sometimes find that it selects the axis of flux ropes, or O-lines, in addition to X-lines, especially if ε is very small. Reconnection does not occur at O-lines, so we developed a second criterion that distinguishes X- and O-lines based on the divergence of the magnetic field curvature vector:

$$[\nabla\cdot(\mathbf{b}\cdot\nabla\mathbf{b})](\Delta x)^2 > c_2 \tag{3.2}$$

where $\mathbf{b} = \mathbf{B}/|\mathbf{B}|$ is a unit vector along the magnetic field. We use $c_2 = -0.1$ to identify X-lines where the curvature vectors point away from the X-line, so their divergence is positive.

The above two criteria are identifying potential magnetic reconnection sites through local plasma properties in a general scenario. However, current sheets in the solar wind can also satisfy those two criteria. To make the selection more selective, we need to introduce a third criterion to exclude the volume outside the magnetosphere. Observations show that specific entropy is two orders of magnitude larger in the magnetosphere than in the magnetosheath [Ma and Otto, 2014] and our simulations properly reproduce these properties. Here we use the specific entropy as the third criterion:

$$\frac{p}{\rho^\gamma} > c_3 \tag{3.3}$$

where p is the plasma thermal pressure, ρ is the plasma density, and $\gamma = 5/3$ is the ratio of the specific heats [Birn et al., 2006, 2009]. Different from the c_1 and c_2 introduced above, this criterion is dimensional and we use the threshold value $c_3 = 0.02\,\mathrm{nPa/cm^{-3\gamma}}$.

The three criteria combined can identify X-lines in the magnetotail well. To make the active PIC region large enough around the X-lines, we flag all patches where all three criteria are met, and then activate all patches within a distance L_x, L_y and L_z from these flagged patches in the x, y and z directions, respectively. The extension in each direction enables the PIC model to cover a buffer area outside the reconnection sites. This buffer ensures that the velocity distribution of ions and electrons at the boundary of the PIC region can be well approximated with a drifting Maxwellian distribution, which results in a consistent coupling between the MHD model. We use $L_x = 4R_E$ and $L_y = L_z = 2R_E$ in this work.

Each MPI process of BATS-R-US calculates the above criteria on their respective sub-domains overlapping with the PIC grid and activate the patches of the PIC grid where all 3 criteria are satisfied. Then the processors collect the information: a PIC patch is activated if any of the BATS-R-US processes activated it. Since the status of all PIC patches (on/off) is

stored in each MPI processor of BATS-R-US, using the default logical array would consume a lot of memory. To reduce the memory use, the status is stored by a single bit, which is 32 times smaller than the size of the default logical variable in Fortran. The information is conveniently collected with the bitwise "or" operator `MPI_BOR` used in the `MPI_ALLREDUCE` call.

3.2.4 Ionospheric Electrodynamics Model: RIM

The Ionospheric Electrodynamics (IE) is simulated by the Ridley Ionosphere Model (RIM) [Ridley et al., 2004] that solves a Poisson-type equation for the electric potential on a 2-D spherical grid. In this work, the grid resolution is set to 2° in both longitude and latitude directions. The lower latitude boundary is at 10° where the electric potential is set to zero.

The BATS-R-US and RIM models are two-way coupled every 5 seconds. To calculate the Poisson-type equation, RIM obtains the field-aligned currents (FAC) calculated at $3R_E$ from the BATS-R-US model and maps them down to its grid. The F10.7 flux is also an input parameter of RIM that is used together with the FAC to calculate the particle precipitation and conductances based on an empirical model. The electric field calculated by the RIM is mapped back to the inner boundary of BATS-R-US to obtain the $\mathbf{E} \times \mathbf{B}/B^2$ velocity for its inner boundary condition. The cross polar cap potentials (CPCP, (the difference of the maximum and minimum potentials in the two hemispheres) are also sent to BATS-R-US to set the density at the inner boundary.

3.2.5 Inner Magnetosphere Model: RCM

The Inner Magnetosphere (IM) is modeled by the Rice Convection Model (RCM) [Wolf et al., 1982, Toffoletto et al., 2003]. The standard RCM settings are used, including an exponential decay term with a 10-hour e-folding rate. The decay term makes the Dst index recover better after strong storms. As a component of the SWMF geospace model, RCM is used in all simulations presented in this paper.

The RCM model is one-way coupled with RIM and two-way coupled with BATS-R-US every 10 seconds. RIM sends the electric potential to RCM, where it is used to advect the field lines with the $\mathbf{E} \times \mathbf{B}/B^2$ drift. In the two-way coupling between BATS-R-US and RCM, BATS-R-US identifies the closed field line regions and calculates field volume integrals of pressure and density [De Zeeuw et al., 2004]. The integrated pressure and density are applied to RCM as the outer boundary condition with the assumption of 90% H^+ and 10% O^+ number density composition. From RCM to BATS-R-US, the GM grid cell centers are traced to the RCM boundary along the magnetic field lines [De Zeeuw et al., 2004] and the BATS-R-US pressure and density are pushed towards the RCM values with a 20s relaxation time.

3.3 3D Global Simulation with Kinetic Physics in the Magnetotail

3.3.1 Simulation Setup

We apply the MHD-AEPIC method to the geomagnetic storm event of Aug. 6. 2011 with an observed minimum Dst $-126\,\mathrm{nT}$. Previous modeling works show frequent flapping motion of the megnetotail current sheet during the storm [Tsutomu and Teruki, 1976, Volwerk et al., 2013], so the adaptive embedding feature is perfect for only covering the current sheet during the simulation. We start our simulation at 2011-08-05 15:00:00 and end it at 2011-08-06 07:00:00. This time range covers the main phase and the early recovering phase of the storm when the largest geomagnetic impact happens. The solar wind inputs are shown in Figure 3.2. First the BATS-R-US and RIM models are run to reach an quasi-steady state after 50k iteration steps using local time stepping. Figure 3.3 shows the plasma density along with the different refinement level boundaries of the AMR grid in the meridional plane for the steady state solution. Then the SWMF is switched to a time-accurate mode with FLEKS

and RCM models turned on. Chen et al. [2017] and Zhou et al. [2020a] study the dayside reconnection at Earth and Ganymede by putting PIC regions at the magnetopause. They also compare the results with Hall MHD and conclude that the two models generate similar global features, such as flux rope formation and reconnection rate. In this paper, we only put PIC regions in the magnetotail, for sake of controlling variants. The dayside reconnection is modeled by the ideal MHD. The computational domain of FLEKS is determined by the selection criteria introduced above. For sake of comparison, we also conduct two other simulations without FLEKS: one with Hall MHD model and the other with ideal MHD model.

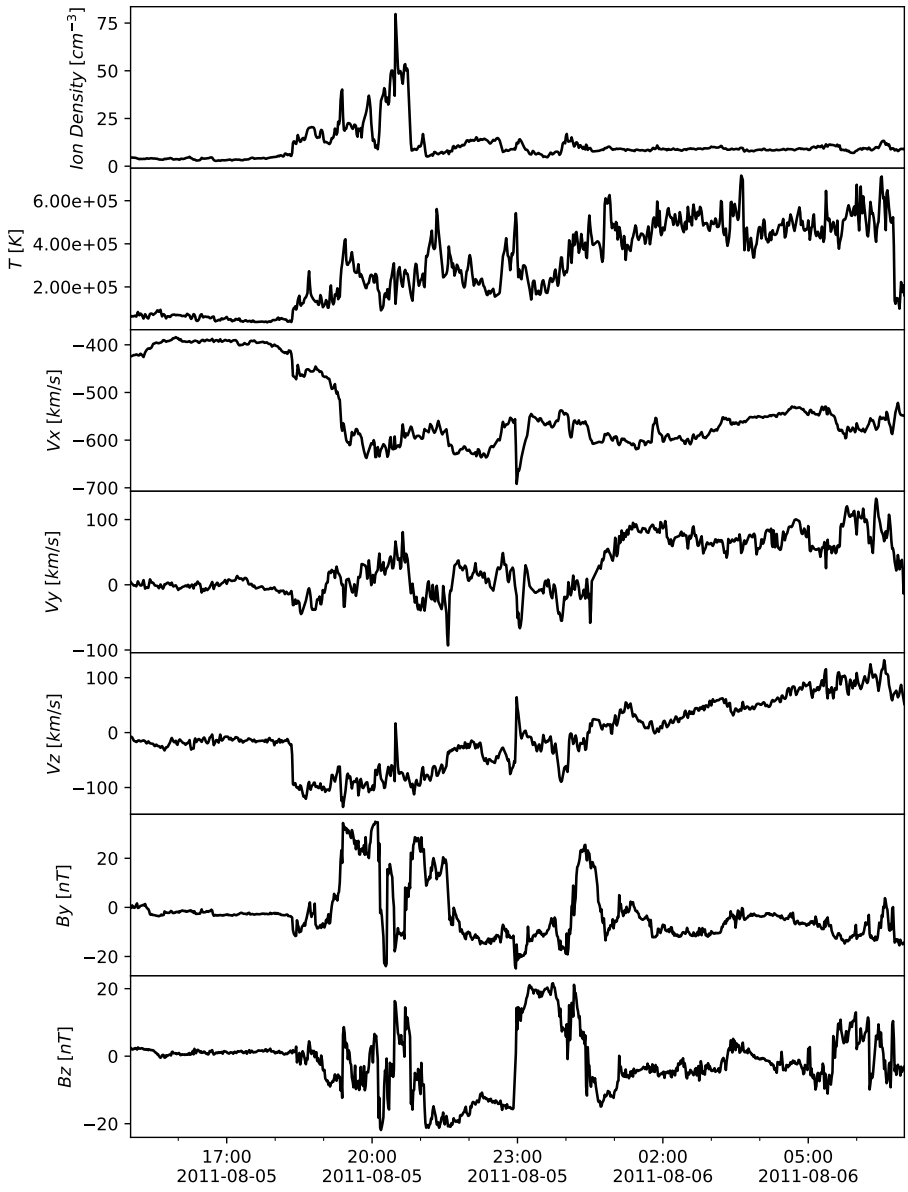

Figure 3.2: The solar wind bulk plasma and interplanetary magnetic field input in Geocentric Solar Magnetospheric coordinates (from top panel to the bottom: plasma density, plasma temperature, x, y and z components of the plasma flow velocity, y and z components of the magnetic field) for the simulation in this paper. The x-component of the magnetic field is set to be 0. The solar wind data is obtained from the ACE spacecraft observation and propagated to the bow shock position [Pulkkinen et al., 2013].

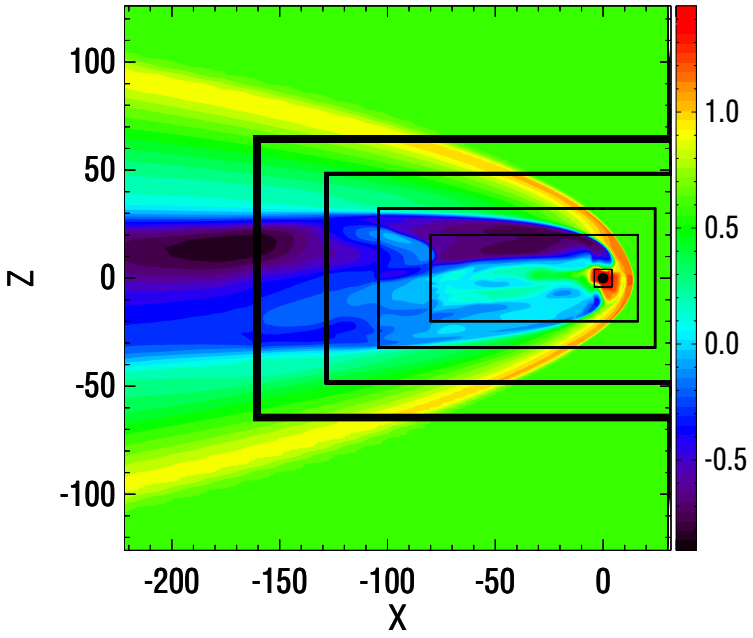

Figure 3.3: The meridional plane of the simulation domain. The color contour shows the plasma density of the steady state on a logarithmic scale. The black lines show the boundaries between different refinement levels. The refinement ratio between two adjacent levels is 2. The grid resolution near Earth is $1/8\,R_E$ it is $1/4\ R_E$ on the dayside and the magnetotail out to $x > -80\,R_E$.

3.3.2 PIC Region Adaptation

In this subsection, we highlight the utility and efficiency of the adaptive embedding scheme. Figure 3.4 illustrates how the PIC region is changing over the simulation. Panels (a)-(f) are snapshots from six different times. The color contours show the j_y component of the current density on the meridional plane to show the magnetospheric current system. Boundaries of the active PIC region are shown by the gray isosurface. Snapshots 3.4 (a) and (b) are taken before the sudden commencement of the storm. At this time, the IMF B_z is pointing northward and the solar wind speed is about 400 km/s. From the isosurface plot, the PIC region is covering the tail current sheet tilting southward. In Figure 3.4 (b), the tail current sheet is kinked and the PIC region adjusts its shape to accommodate the tail current sheet. Snapshots 3.4 (c)-(f) are taken after the sudden commencement of the storm. Here we observe a much compressed magnetosphere as well as an enhanced current density. In the

last two snapshots, the tail current sheet is tilting northward and it is well covered by the PIC region. From the snapshots, we can conclude that the PIC region selection criteria work well in identifying the tail current sheet, which can make the PIC region accommodate with the flapping motion of the magnetotail. The translucent red line in Figure 3.4 (g) shows the volume of the active PIC region recorded every second from the simulation, while the solid red line is the volume smoothed over every minute. The Dst index is also presented in the background for reference. The volume of the PIC region increases after the sudden commencement and starts dropping in the recovering phase. This reflects that the tail current system intensity is related to the solar wind condition. Notice that the volume is less than 2000 R_E^3 for the entire storm simulation, which is only about 1.4% of the large PIC box extending from $-100R_E$ to $-10R_E$ in the x direction and $-20R_E$ to $20R_E$ in the y and z directions. This confirms that the MHD-AEPIC method saves substantial amount of computational resources.

3.3.3 Global Scale: Geomagnetic Indexes and Ionospheric Quantities

To evaluate the models' performance at the global scale, we use the SYM-H and SME as evaluation metrics. The SYM-H index approximates the symmetric portion of the northward component of the magnetic field near the equator based on measurements at six ground magnetometer stations. This index characterizes the strength of the ring current [Ganushkina et al., 2017] and it is an indicator of storm activity. The SYM-H data with a 1-minute cadence is downloaded from NASA OMNIWeb Data Service. The SuperMAG electrojet (SME) index is an indicator of substorms and auroral power [Newell and Gjerloev, 2011]. SME utilizes more than 100 ground magnetometer stations at geomagnetic latitudes between +40° and +80°, which resolves the large and extreme events more effectively than the traditional Auroral Electrojets (AE) index [Davis and Sugiura, 1966, Bergin et al., 2020].

In our model, the simulated SYM-H is calculated by evaluating the Biot-Savart integral

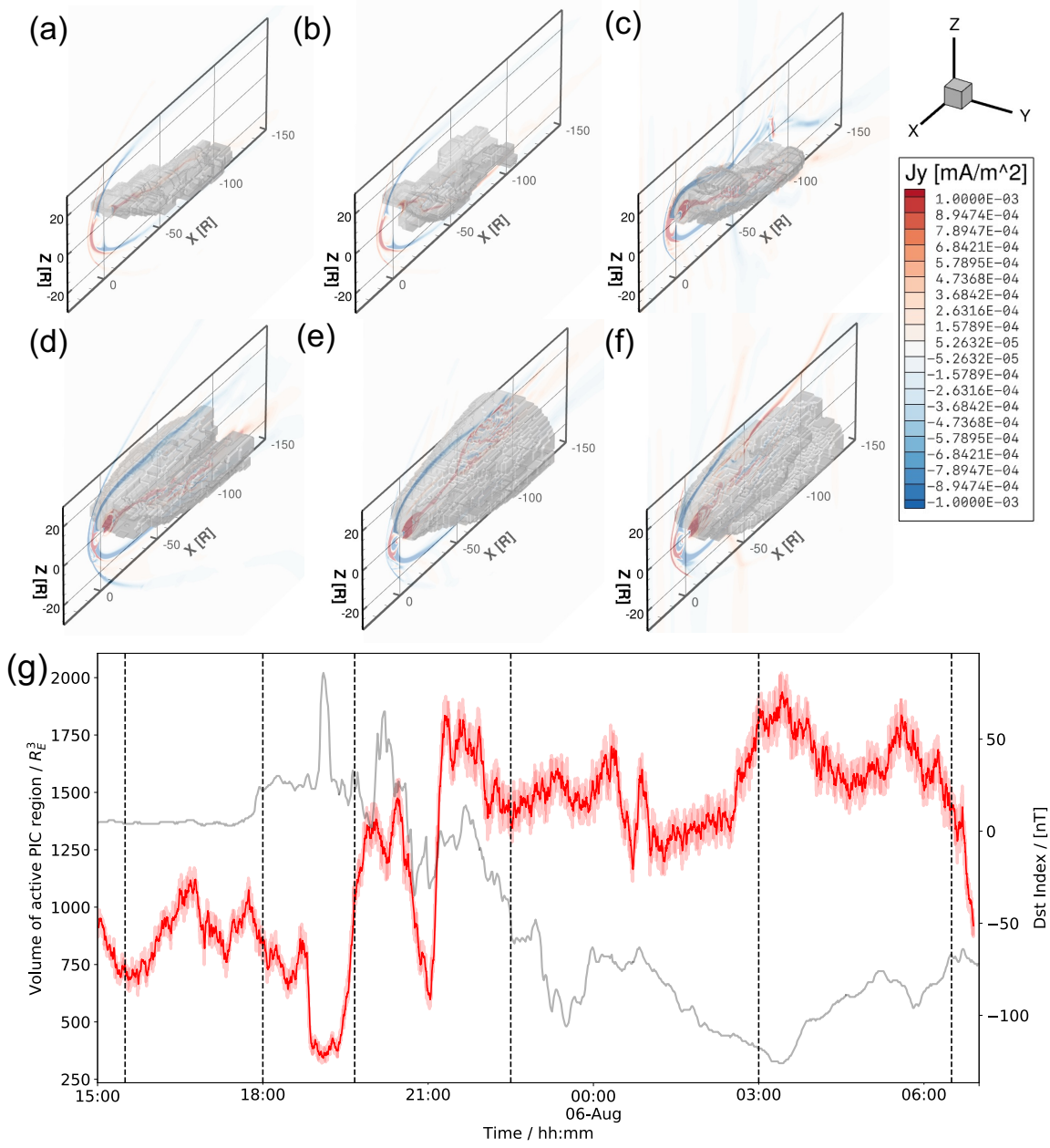

Figure 3.4: (a-f) Demonstration of PIC region adaptation during the simulation. The contour plot of j_y in the meridional plane is showing the general condition of the magnetospheric current system. The active PIC region boundary is shown by a gray isosurface. (g) Time evolution of the active PIC region volume. The translucent red line is the output every second and the solid red is the output smoothed every minute. The Dst index is plotted as a gray line for reference. The six vertical dashed lines correspond to the times of the snapshots (a)-(f), respectively.

at the center of the Earth from all currents in the simulation domain. Calculating SME is more complicated: the magnetic field disturbances are calculated at the positions of the 100+ ground magnetometer stations and the simulated SME is obtained following the SuperMAG procedure. From Figure 3.5, the MHD-AEPIC produces geomagnetic indexes close to the other two MHD models. The SYM-H plot shows that the initial, main and recovery phases of the storm event are reproduced by all three models reasonably well. However, the models cannot reproduce the lowest SYM-H values that correspond to the strongest observed geomagnetic perturbations. This feature can also be observed in the SME plots: all three models produce increased auroral electrojets, however the second and third enhancements are weaker than the observed values.

Apart from the global indexes such as SYM-H and SME, it is also important to compare the amount of energy that the solar wind and interplanetary magnetic field (IMF) transfer to Earth's magnetosphere-ionosphere system through direct driving. The cross polar cap potential (CPCP) is an indicator of this energy transfer process [Troshichev et al., 1988, 1996]. The CPCP is not directly measured but can be derived from observations using the Assimilative Mapping of Ionospheric Electrodynamics (AMIE) [Richmond and Kamide, 1988] technique or from the Defense Meteorological Satellite Program (DMSP) measurements [Hairston et al., 1998]. Another approach based on the Super Dual Auroral Radar Network (SuperDARN) observations [Ruohoniemi and Greenwald, 1998] usually underestimates the CPCP significantly. We opt to use the readily available Polar Cap Index (PCI) from the OMNIWeb website and convert it into CPCP using the empirical relationship derived by Ridley and Kihn [2004]:

$$\mathrm{CPCP_{North}} = 29.28 - 3.31 \sin\left(T + 1.49\right) + 17.81 \mathrm{PCI\_N} \tag{3.4}$$

where T is the month of the year normalized to 2π. The storm event in this paper is in August, so $T = (8-1) * 2\pi/12$. Gao [2012] showed that this formula provides good

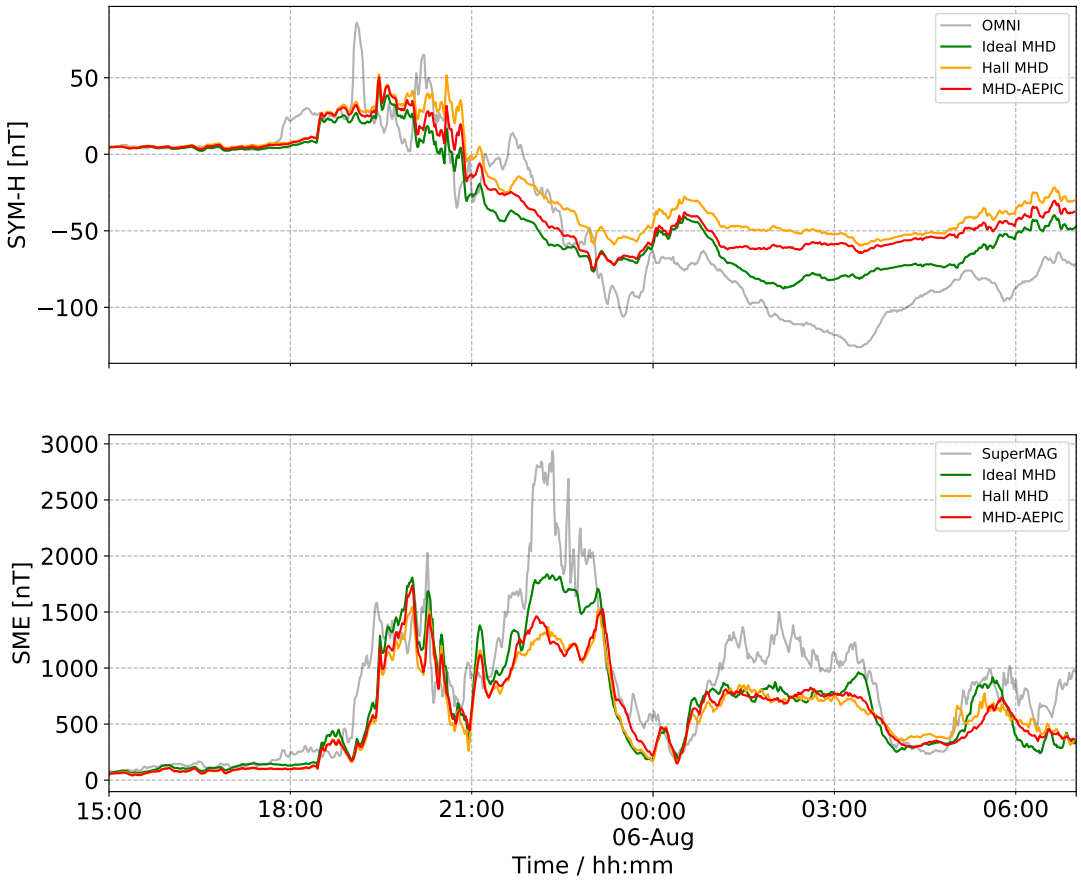

Figure 3.5: Aug. 6 2011 storm. Colored lines show the SYM-H and SuperMAG electrojet (SME) indexes from three different models and the gray line corresponds to the observed indexes.

agreement with AMIE and DMSP based approaches. For the southern hemisphere, since there is no published empirical relationship between southern CPCP and PCI, we change the sign in front of the $\sin(T + 1.49)$ term (expressing the seasonal dependence) in the formula:

$$\mathrm{CPCP}_{\mathrm{South}} = 29.28 + 3.31 \sin(T + 1.49) + 17.81\mathrm{PCI\_S} \tag{3.5}$$

The simulated CPCP is defined as the difference between the maximum and the minimum of the electric potential obtained from the RIM model for both hemispheres.

Figure 3.6 (a) shows the northern and southern cross polar cap potentials from the three models together with the CPCP derived from the PCI. In general, the results from the three models are very close to each other and have good agreements with the PCI derived CPCP for both hemispheres. Notice that the PCI is derived from a single station for each hemisphere while the model calculates CPCP using the entire electric potential. The differences between the model output and CPCP could because the PCI is not measuring the ionospheric dynamics for the entire polar region. We observe that the three models generate the most different CPCP results during the main phase of the storm event at around $t =$ 2011-08-05 22:00:00. Figure 3.6 (b) shows the polar cap potential and radial component of the field aligned currents for both hemispheres. The structure of the electric potentials as well as the field aligned currents are very similar among the three models.

The geomagnetic indexes and ionospheric quantities demonstrate that introducing kinetic physics in the magnetotail does not change the global configuration of the simulated magnetosphere and ionosphere significantly relative to the ideal and Hall MHD simulations. It is to be seen if this trend persists for other storms, especially extreme events.

3.3.4 Mesoscale: Magnetotail Dynamics

During the storm event, the Geotail spacecraft was in the magnetotail at $x \approx -29\, R_E$ crossing the equatorial plane and approaching to the meridional plane. Figure 3.7 shows the mag-

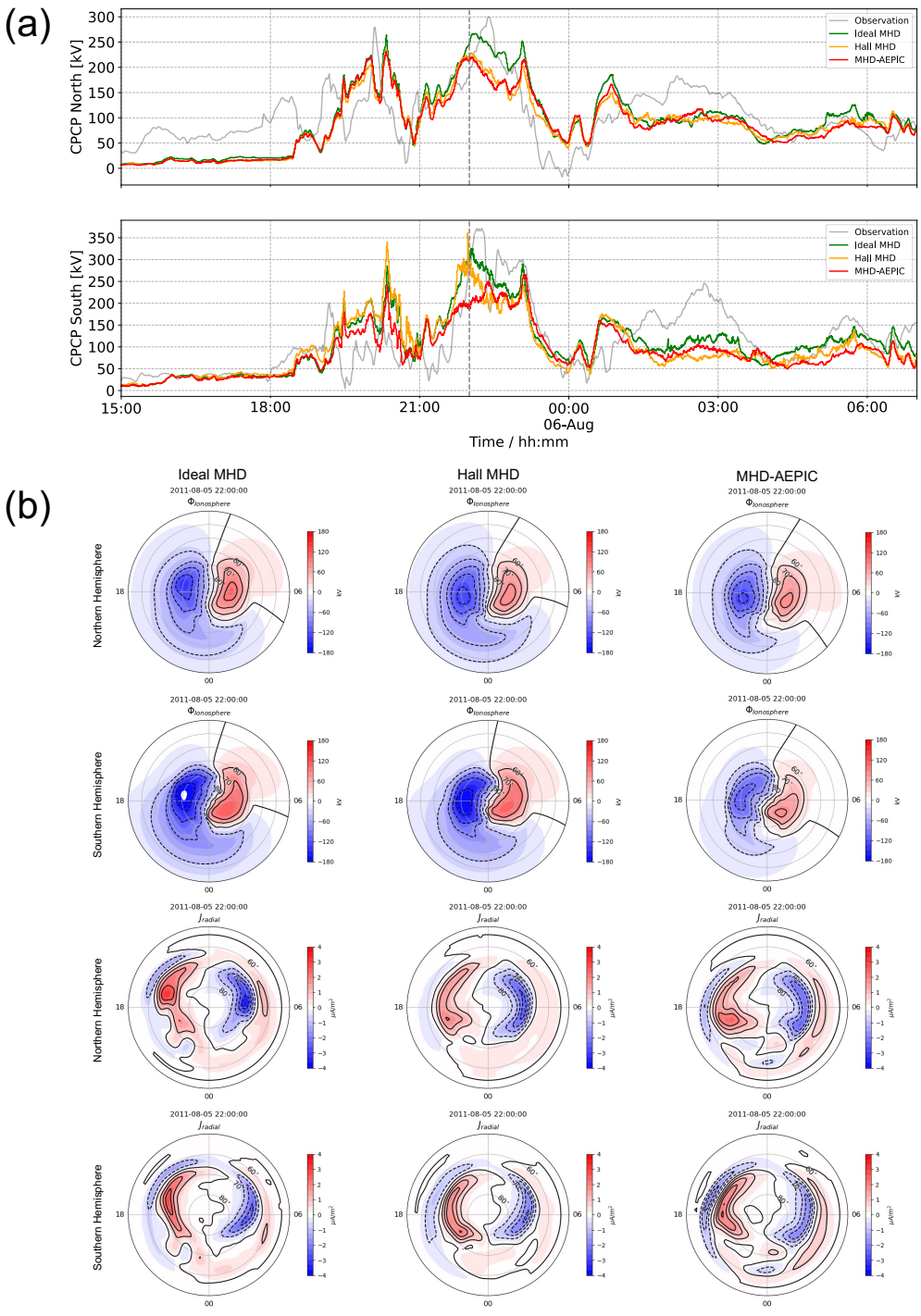

Figure 3.6: (a) The northern and southern cross polar cap potentials (CPCP) of the Aug. 6 2011 storm. Colored lines are model outputs, the gray line is the CPCP estimated [Ridley and Kihn, 2004] from the observed Polar Cap Index . (b) The northern and southern electric potentials and the radial current from the three models at 2011-08-05 22:00:00 (marked with a vertical dashed line in panel (a)).

netic field and ion moments observed by Geotail and compares them with the ideal-MHD, Hall-MHD and MHD-AEPIC simulations. The MHD-AEPIC model shows a reasonable agreement with the Geotail number density observation before t = 2011-08-06 00:00, including the current sheet crossing event between t = 2011-08-05 22:00 and t = 2011-08-05 23:00 while the Hall-MHD model overestimates the ion number density substantially. However, all three models generate much higher number density than observed after t = 2011-08-06 00:00. None of the three models show perfect agreement with the magnetic field observations. The B_x component gives us information about which side of the current sheet the satellite is. The comparison plot shows that the virtual satellites in the simulations are all on the opposite side of the current sheet than Geotail before t = 2011-08-05 22:00. Between t = 2011-08-05 23:00 and t = 2011-08-06 01:00, Geotail is crossing the current sheet from the north side to the south side, and this is captured by all three models. However, the next current sheet crossing at around t = 2011-08-06 01:30 is not captured by MHD-AEPIC and ideal-MHD. The Hall-MHD simulations produces a similar structure but with a 30-minute time shift. The B_y and B_z components give information about flux rope structures. All three models provide good agreement with the observation in terms of overall field magnitude, while it is difficult to tell which one is better in capturing fine details. Geotail observed a B_z reversal along with a relatively strong core B_y at around t = 2011-08-06 05:00, which indicates a flux rope. A similar structure is produced by MHD-AEPIC with a 30-minute delay, while there is no similar signal from the ideal-MHD and Hall-MHD simulations. Geotail observed high ion speed around 1000 km/s at t = 2011-08-06 02:00 and t = 2011-08-06 03:00. The MHD-AEPIC model only generates around 500 km/s ion speeds. Although the ideal-MHD and Hall-MHD models can produce maximum ion speeds around 1000 km/s, they also generate large scale oscillations that are not present in the observations. Overall, introducing kinetic physics in the magnetotail did not improve plasma and magnetic features compared to the ideal MHD simulation at the mesoscale. The Hall MHD simulation, on the other hand, produces significantly more oscillations than observed in multiple time periods.

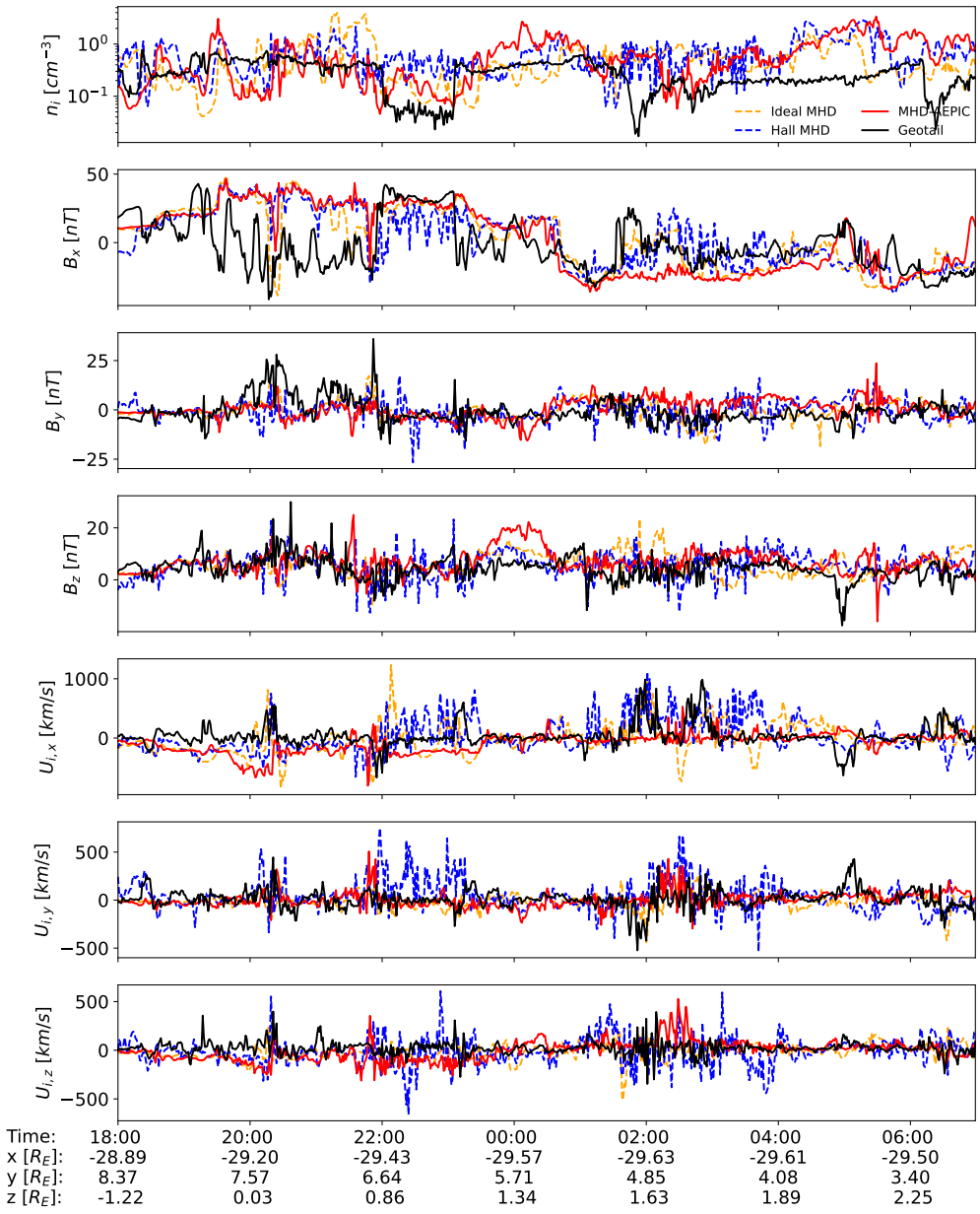

Figure 3.7: The ion density, magnetic field components and the ion velocity components observed by the Geotail spacecraft and the SWMF ideal MHD, Hall MHD and MHD-AEPIC simulations. The time interval shown starts from t = 2011-08-05 18:00:00 right before the sudden commencement to t = 2011-08-06 00:07:00 at the beginning of the recovery phase of the geomagnetic storm. The bottom X axis shows the GSE coordinates of the spacecraft at various times.

Since Geotail only observes along a single trajectory, it cannot provide insight into the full dynamics of the magnetotail. To compare the different models, we plot results on 2-D surfaces. Figure 3.8 shows the magnetosphere simulation results from three models at the same time 2011-08-05 19:40:00. Figure 3.8 (a1), (b1) and (c1) show the x component of the ion bulk velocity and magnetic field lines in the meridional plane ($-80\,R_E < x < -5\,R_E$ and $-20\,R_E < z < 10\,R_E$) from MHD-AEPIC, Hall MHD and ideal MHD simulations, respectively. The global configurations of the magnetosphere share a lot of similarities but there are several differences as well. All three models give a southward tilted magnetotail that is compressed most in the z direction at around $x = -40R_E$ as a result of the IMF structure. In terms of the reconnection feature, all three models generate X-lines in the tail current sheet at around $x = -20\,R_E$ and $z = -5\,R_E$ Diverging reconnection ion jets are generated at the major X-line for all three models.

To analyze physical quantities in the current sheet better, we extract the quantities along a surface where $B_x = 0$ and project this surface to the $x - y$ plane for plotting. The bottom row in Figure 3.8 shows the z coordinate of the center of the current sheet. The structure is similar as in the meridional plane plots: the current sheets are at $z \approx 0$ near Earth and at $z \approx -15\,R_E$ at far tail for MHD-AEPIC and Hall MHD models, while $z \approx -12\,R_E$ for ideal MHD. Figure 3.8 (a2)-(c2) show the ion bulk flow speed on the current sheet surface. There are significant differences among the three models in the earthward ion flow structures. For ideal MHD, the earthward ion flow is distributed roughly symmetrically at $-3\,R_E < y < 3\,R_E$. The earthward ion jet generated by Hall MHD can only be observed on the dawn side at $-5\,R_E < y < 0$. The MHD-AEPIC simulation produces earthward ion jet both on the dawn and dusk sides. However, the ion jet on the dawn side is further away from the earth than the jets on the dusk side. Also, the earthward ion jets can be observed from $-5R_E$ to $7R_E$ in the y direction, which agrees with the observations that earthward flows are observed at a wide range of y values [Angelopoulos et al., 1994].

Although the earthward ion flow from MHD-AEPIC is different from pure MHD models,

the similar magnetic field structure and current sheet position indicate that these snapshots from different models represent the same physical state of the magnetosphere. Hence, it is valid to examine the flux rope features based on these results. As first proposed to be formed in the Earth's magnetotail [Schindler, 1974], magnetic flux ropes are reported to be closely related to magnetic reconnection by various observations and simulations [Hones Jr et al., 1984, Slavin et al., 1989, Daughton et al., 2006, Markidis et al., 2013]. The observational characteristics of the flux ropes are a pair of positive and negative B_z signatures with a core magnetic field B_y in between. Hence, we plot the B_z and $|B_y|$ components on the current sheet surface in Figure 3.8(a-c)(2-3). Panels (c3) and (c4) show only one flux rope at $-40\,R_E$ and there is no evidence indicating flux rope exists at the near earth plasma sheet from $-40\,R_E$ to the Earth based on the ideal MHD model results. The Hall MHD and MHD-AEPIC give very different flux rope occurrence (Figure 3.8 (a-b)(3-4)) from ideal MHD. In addition to the moving directions of the flux ropes, the diameter of the flux ropes also varies: the earthward flux ropes are observed as smaller ones. This difference has been reported in a thorough analysis of Geotail observations [Slavin et al., 2003]. By examining the flux ropes as a mesoscale feature, we can conclude that by modeling the reconnection physics better, the MHD-AEPIC and Hall MHD simulations produce more flux ropes in the magnetotail than ideal MHD as well as distinguish two types of the flux ropes. However, there is no evidence supporting that MHD-AEPIC can produce better mesoscale features than Hall MHD. This could be the case because the spatial scale of the flux ropes is much larger than the kinetic scale which PIC model is resolving.

Figure 3.9 shows different physical quantities near the reconnection X-line at the same time as Figure 3.8. Panel (a) shows the current density of the current sheet j_y, the out-of-plane magnetic field B_y and the ion bulk velocity U_{ix} from the ideal MHD model. The current sheet is smooth and narrow around the X-line. The simullation produces diverging ion outflow as expected. There is no significant B_y near the reconnection site due to the lack of Hall physics in the ideal MHD model. Panel (b) shows the same quantities as Panel (a)

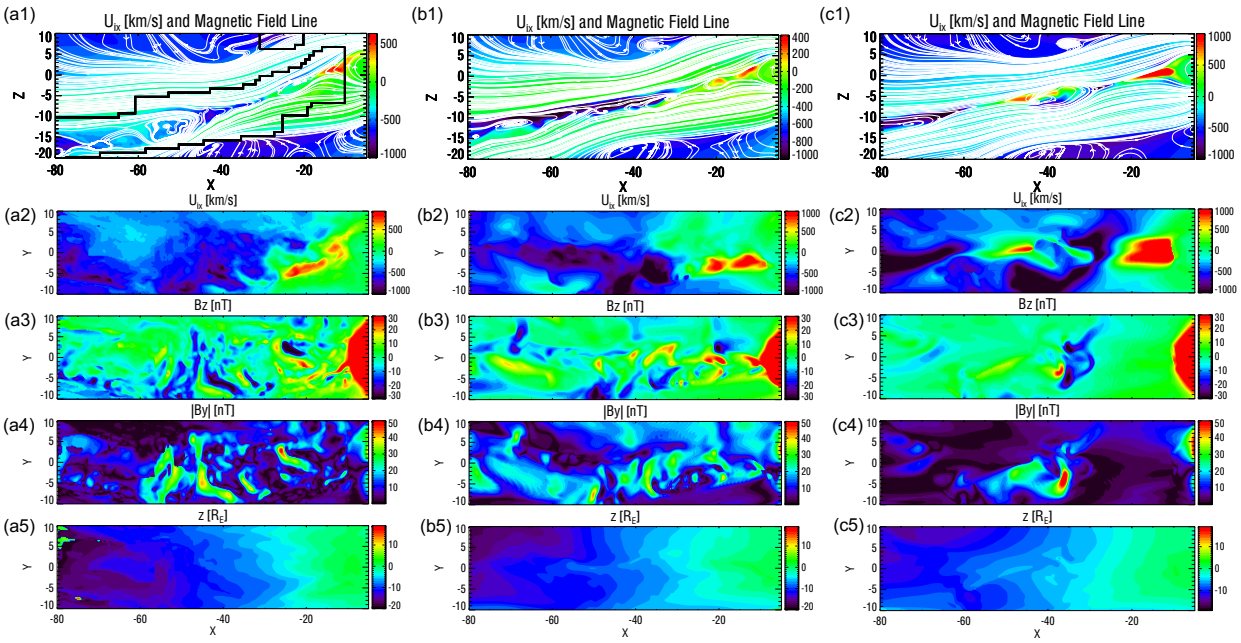

Figure 3.8: (a1) The x component of the ion bulk velocity $u_{i,x}$ and magnetic field lines on the meridional plane from the MHD-AEPIC simulation. The black line shows the boundary of the active PIC region. (a2) $u_{i,x}$ on the current sheet surface projected on the x-y plane. (a3) The contour plot of the B_z on the current sheet surface, color saturated at ± 30 nT. (a4) The absolute value of B_y on the current sheet surface. A pair of positive and negative B_z along with a core B_y indicates a flux rope structure. (a5) The z coordinate of the current sheet surface in the unit of R_E. (b1)-(b5) are same quantities from the Hall MHD and (c1)-(c5) are from the ideal MHD simulation. All snapshots are taken at the same time 2011-08-05 19:40:00.

for the Hall MHD model. In addition, the bottom plot shows the electron velocity in the x direction calculated from the ion bulk velocity and the Hall velocity as $u_{ex} = u_{ix} - j_x/(ne)$. Different from the current sheet in the ideal MHD model, the current sheet in the Hall MHD simulation breaks up at multiple locations. There are strong B_y signatures in the Hall MHD simulation as expected from Hall physics, although the presence of the non-uniform guide field somewhat distorts the classical quadrupolar structure. The diverging ion bulk flow is very similar to the diverging electron flow, because the j_x component of the current is weak. Panel (c) shows the same quantities as Panel (b) from the MHD-AEPIC model with an extra ion nongyrotropy measure $D_{ng,i}$. The current sheet in the MHD-AEPIC simulation also forms multiple flux ropes similar to the Hall MHD results. The MHD-AEPIC model also generates the Hall magnetic field B_y. The ion and electron velocities from the MHD-AEPIC show very clear inflow and outflow features that are quite different from the Hall MHD solution. While both ideal and Hall MHD assume isotropic pressures, the PIC simulation allows a general pressure tensor with anisotropy and even nongyrotropy (non-zero off-diagonal terms). Aunai et al. [2013] defines the nongyrotropy measure as

$$D_{ng} = 2\frac{\sqrt{P_{12}^2 + P_{23}^2 + P_{13}^2}}{P_{11} + P_{22} + P_{33}} \tag{3.6}$$

Here P_{ij} are the pressure tensor components in the local magnetic field aligned coordinate system. The D_{ng} quantity produced by the MHD-AEPIC model shows that the ion nongyrotropy increases near the X-line. In conclusion, both Hall MHD and MHD-AEPIC generate more features than the ideal MHD model. The MHD-AEPIC and the Hall MHD models generate similar Hall magnetic field structures and current sheet features. The MHD-AEPIC model generates distinct ion and electron bulk flows, as well as the nongyrotropic pressure distribution near the X-line.

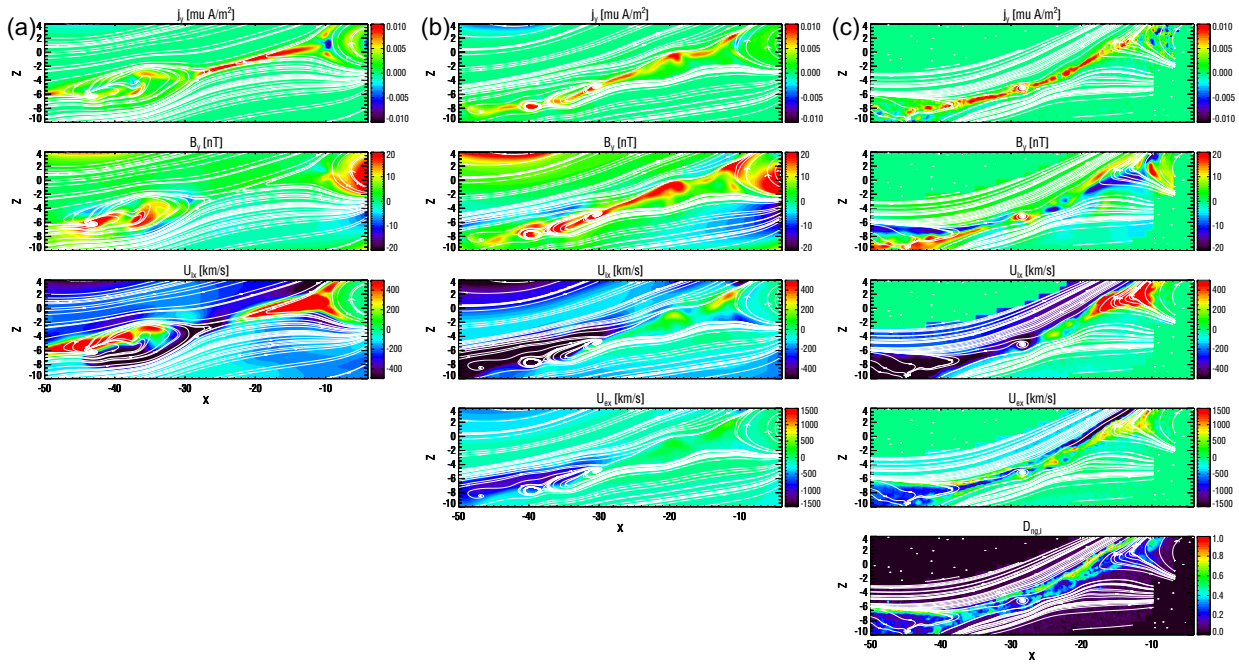

Figure 3.9: (a) The current density j_y, out-of-plane magnetic field B_y and ion bulk velocity in the x direction U_{ix} from the ideal MHD model near the reconnection X-line. (b) Same physical quantities as panel (a) from the Hall MHD model with an extra electron bulk velocity in the x direction U_{ex} calculated from the current. (c) Same physical quantities as panel (b) from the MHD-AEPIC model with an extra ion nongyrotropy measure $D_{ng,i}$ defined by Aunai et al. [2013]. The area covered by the magnetic field lines is the active PIC region.

3.3.5 Kinetic Scale: Electron Velocity Distribution Function

In this subsection, we will demonstrate that the kinetic physics at the reconnection site is also properly captured by the MHD-AEPIC model. The magnetic reconnection is regarded as one of the most fundamental physical processes to transfer energy from magnetic field to plasma. Since the launch of the Magnetospheric Multiscale (MMS) mission [Burch et al., 2016a], magnetic reconnection has been observed at the electron scale during multiple satellite crossings of the electron diffusion region (EDR) [Webster et al., 2018]. The EDR encounters exhibit electron nongyrotropy, which can be recognized by a crescent-shaped electron distributions [Torbert et al., 2018].

Figure 3.10 compares the MHD-AEPIC simulation with MMS observations [Hwang et al., 2019]. Panel (a) is a contour plot of ion bulk velocity in the meridional plane at t = 2011-08-05 23:20:00. The ion jets, a clear signature of magnetic reconnection, are shown by the blue and red colors. The dashed white line near the X-line, which is rotated about 13.3°, is the L direction of the local reconnetion coordinate system. We also found that the M axis is aligned with the y axis in GSM. So the LMN coordinate vectors for this reconnection event are $L = (0.972, 0, 0.233), M = (0, 1, 0)$ and $N = (-0.233, 0, 0.972)$. The electron velocities are shown in the LMN coordinate system to allow a direct comparison with the MMS observations. Panels (b) and (d) show the electron velocity distribution functions (VDF) from the model and the MMS observation. The simulation VDF of the electrons is collected inside an ellipsoid region centered at $(-30.6, 0.5, -0.9)$ R_E with principle semi-axes $(0.3, 2.5, 0.3)$ R_E in the (x, y, z) directions, respectively. The red circle in panel (a) labeled by B is the cross section of the ellipsoid with the meridional plane. The choice of the ellipsoid shape is based on panel (c) that shows where the MMS observations were taken with respect to the reconnection site according to Figure 2 by Hwang et al. [2019]. The MMS3 observations of the electron VDF [Hwang et al., 2019] at the location $(-18.1, 7.30, 0.66)$ R_E are shown in panel (d). Although the simulation and observation are not from the same event and the EDR is not at the same position in GSM coordinates, the electron data is collected

at a similar location relative to the X-line and the velocity components are all projected to the LMN coordinates (see panels (a) and (c)).

This suggests that we can directly compare the two VDF plots in panels (b) and (d), and they indeed agree very well. The agreement is not only qualitative, but in fact quantitative. Since the ion-electron mass ratio is 100, the simulated electron velocity is multiplied by $\sqrt{\frac{\mathrm{m_{i,real}}}{\mathrm{m_{e,real}}}/\frac{\mathrm{m_{i,simulation}}}{\mathrm{m_{e,simulation}}}} \approx \sqrt{18.36} \approx 4.28$ to be comparable with the observations. In both panels the velocity distribution extends to $\pm 40,000\,\mathrm{km/s}$ in the N direction and $(-40,000, +20,000)\,\mathrm{km/s}$ in the M direction. A non-Maxwellian core distribution can also be clearly identified in both panels at $-20,000\,\mathrm{km/s} < v_y < 10,000\,\mathrm{km/s}$) and $|v_z| < 10,000\,\mathrm{km/s}$. In addition to the electron diffusion region, we also collected electrons inside two other ellipsoids at the inflow (labeled by A) and outflow (labeled by C) regions. The semi-axes of these two ellipsoids are the same as before while the centers of the ellipsoids are $(-28.5, 1.5, 0.5)\ R_E$ and $(-33.0, 1.5, -1.0)\ R_E$ in the (x, y, z) directions, respectively. Panels (e) and (f) shows the electron VDF in $L-N$ and $L-M$ coordinates, the distribution can be characterized as a bidirectional beam distribution [Asano et al., 2008]. The distribution functions at outflow region in panels (g) and (h) are almost circles with shifted centers indicating the direction of the bulk velocities. The distribution functions from the inflow and outflow also agree very well with the existing theories [Pritchett, 2006, Egedal et al., 2010]. Hence, we can conclude that an MHD-AEPIC global simulation can generate electron phase space distributions that are very close to the MMS observations, and reproduces the main features of reconnection physics even at the electron scales.

3.4 Conclusions and Discussions

In this paper, we introduced a newly developed magnetohydrodynamic with adaptively embedded particle-in-cell (MHD-AEPIC) model. The MHD-AEPIC allows PIC grid cells to be turned on and off during the simulation based on the physical criteria provided. Different

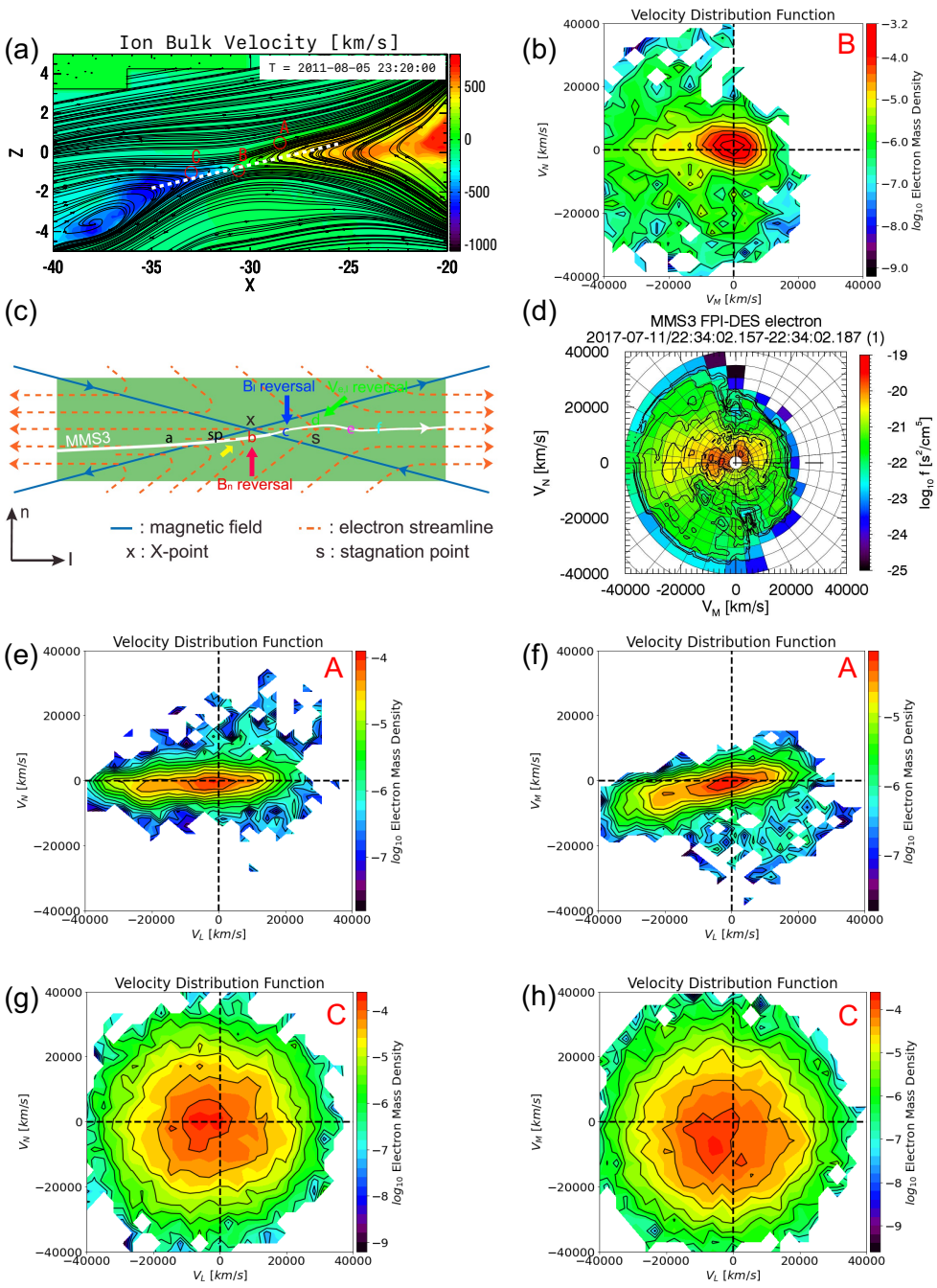

Figure 3.10: (a) The contour plot of the ion bulk velocity overplotted with magnetic field lines. The 2D cut is taken on the meridional plane. The three red circles are the position where the electrons for the VDF are collected. A: Inflow region, B: Electron Diffusion Region, C: Outflow region. The white dashed line with a Notice that some area at upper left is not covered by PIC which illustrates the AEPIC feature. (b) The electron VDF from the simulation, colored in electron mass density in log scale. (c) A sketch (Figure 1 (b) in Hwang et al. [2019]) demonstrating possible magnetic field geometries. The white curve represents a possible MMS3 trajectory. The electron VDF in (d) is taken at the position *b* pointed by a red arrow. (d) MMS3 observation (Figure 2 (c) in Hwang et al. [2019]). (e)-(f) The electron VDF taken at the inflow region. (g)-(h) The electron VDF taken at the outflow region.

from the previous MHD-EPIC model, which requires a fixed Cartesian box to cover the PIC region, the MHD-AEPIC model enables PIC regions moving with the reconnection sites to save computational resources substantially. During the main phase of the storm, from t = 2011-08-06 00:05:00 to t = 2011-08-06 02:54:00, when the volume of the PIC domain is about $1500\,R_E^3$. The relative timings are the following: 72.72% of CPU time is used on FLEKS, 13.26% is for BATS-R-US and 10.35% is taken by the coupling between FLEKS and BATS-R-US. The rest 3.67% of CPU time is consumed by RIM, RCM and the overhead of the SWMF. For the entire 16-hour geomagnetic storm simulation, the total wall time is 256.29 hours on 5600 CPU cores.

We also introduced three physics based criteria to identify the reconnection regions in the magnetotail. To demonstrate the feasibility of the MHD-AEPIC model, we have performed a geomagnetic storm event simulation with kinetic physics embedded for the first time. The flapping motion of the magnetotail current sheet during the geomagnetic storm highlights the advantage of the adaptation feature of the MHD-AEPIC model.

We have also simulated the same event using Hall MHD and ideal MHD models and compared the three models at multiple physical scales. We examined the global scale features by comparing the SYM-H and SME indexes which reflect the equatorial and auroral region disturbances, respectively. All three models properly capture the global scale disturbances such as the main phase of the storm or the increase of the auroral electrojet. However, all three models fail to produce the strongest intensity for the geoindices. Hence no significant difference is found among the three different models at the global scale for this event. This indicates that the global magnetosphere configuration from the three models are very close, the kinetic model embedded in the magnetotail does not improve the global scale feature for this geomagnetic storm. If this trend persists for other storms, especially extreme events, is still to be investigated.

We analyze the mesoscale features by comparing the magnetic field components and ion profiles between the Geotail observation and the simulations. All three models show fairly

good agreement with the Geotail observations, however, none of the three models can match all features such as all the current sheet crossing or flux rope signatures. The Hall MHD simulation shows more oscillations than observed during a few time periods. In this storm event, MHD-AEPIC and ideal MHD models produce similar agreement with the in-situ observations of Geotail.

In addition to comparing with the Geotail observations, we also compare the three models with respect to flux rope structures in the current sheet. Only one major flux rope can be observed from the ideal MHD simulation at the selected time, while Hall MHD and MHD-AEPIC can produce flux ropes at a wider range in the dawn-dusk direction. The difference of two types of the flux ropes: earth-ward with smaller spatial scale and tail-ward with a lager spatial scale is also illustrated by the MHD-AEPIC simulations, in agreement with several observations [Slavin et al., 2003].

The electron scale kinetic physics is well reproduced by the MHD-AEPIC model. We collect electron macro-particle velocities at the same side of the electron diffusion region as the MMS3 satellite did [Hwang et al., 2019]. The velocity distribution functions show excellent agreement between the simulation and the MMS3 observation. This demonstrates that MHD-AEPIC can properly produce the electron scale features within a single self-consistent global model while simulating a complete geomagnetic storm event. In this particular simulation, including the kinetic reconnection physics does not improve agreement with observations at meso- and global scales. This suggests that in this storm event, the magnetosphere is mostly driven by the external solar wind and interplanetary magnetic field and not by the internal reconnection dynamics.

It is to be investigated if the kinetic physics can have a more pronounced influence on the physical condition of the magnetosphere when the external drivers are relatively constant. Another important question is to compare the impact of kinetic versus numerical reconnection during extreme events. In addition to studying the Earth's magnetosphere, we also expect the novel MHD-AEPIC model will find its applications in various collisionless plasma

systems that form small regions where kinetic effects are important inside a large spatial domain.

CHAPTER 4

Simulation of Magnetospheric Sawtooth Oscillations: the Role of Kinetic Reconnection in the Magnetotail

This chapter is adapted from a manuscript to be submitted.

4.1 Introduction

More than two decades ago, Borovsky et al. [1993a] observed that the time variation of electron fluxes at geosynchronous orbit resemble a tooth of a saw blade: a slow decrease followed by a rapid increase. Moreover, this feature is observed in a wide range of magnetic local time (MLT), which distinguishes it from isolated substorms. These periodic injections also have impacts on other geospace features like magnetic field variations at geosynchronous orbit, the auroral electrojet index, and the polar cap index [Cai et al., 2006, Henderson et al., 2006, Huang et al., 2003]. Although there is still no definitive answer to the mechanisms producing the sawtooth oscillations, numerical simulations for the coupled magnetosphere-ionosphere system have demonstrated a possible explanation related to the O^+ outflow from the ionosphere [Brambles et al., 2011]. The basic idea of this theory is that the periodic mass loading and unloading from the ionospheric outflow alters the reconnection rate in the magnetotail current sheet. The different reconnection rate results in different magnetic field

configuration in the tail, which modulates the ionospheric outflow rate. This feed back loop produces the periodic oscillations.

There are a number of studies establishing this theory over the past decade. Wiltberger et al. [2010] uses the Multi-Fluid Lyon Fedder Mobarry (MFLFM) model to demonstrate that the out-flowing cusp ions transported to the tail can have an effect on the magnetic configuration. and trigger substorm dipolarizations. Yu and Ridley [2013] also shows that cusp O^+ outflow can influence the development of isolated substorms. Brambles et al. [2011] applies an empirical power-law relationship between the the Alfvénic Poynting flux and the resulting ionospheric outflow flux at the simulation inner boundary and shows that this outflow can induce quasi-periodic substorms resembling observed sawtooth oscillations. In a follow-up study, Ouellette et al. [2013] studies how the ion composition of the plasma sheet and magnetotail affects the tail reconnection rate. They hypothesized that the massive outflow inflates the magnetosphere and enables the development of the next sawtooth oscillation. Later on, Brambles et al. [2013] used the same model on two different types of sawtooth events induced by different external driving conditions: the SIR-driven 24 October 2002 event and the CME-driven 18 April 2002 event. They find that quasi-periodic substorms occurred in the SIR event without outflow while no periodic substorm occurs in the CME event without outflow. Presumably, the quasi-periodic substorms in the SIR event are triggered by the variations in the external driving condition while in the CME event, they are more related to the internal mechanism of the magnetosphere. More recently, Lund et al. [2018] uses mass composition data from the Cluster satellites and discovers the role ionospheric outflow plays in inducing sawtooth oscillations. They find during the CME events, the O^+ in the mid-tail plasma sheet is mostly from the cusp/dayside while the nightside outflow preconditions the plasma sheet to enable the sawtooth oscillations. The recent work by Zhang et al. [2020] illustrates that magnetospheric sawtooth oscillations can be solely induced by cusp O^+ outflows in the global simulation conducted by the LFM model.

The previous publications all show that the magnetotail reconnection is the key factor in

inducing the sawtooth oscillations and the ionospheric outflow is affecting the reconnection rate. In this paper, we use the University of Michigan's Space Weather Modeling Framework (SWMF) [Tóth et al., 2012] to investigate how kinetic reconnection affects the sawtooth oscillations under constant solar wind driving conditions. In addition to the global MHD model simulating Earth's magnetosphere, we are using the FLexible Exascale Kinetic Simulator (FLEKS) [Chen et al., 2021] in the magnetotail to model the tail reconnection with full kinetic physics. For comparison, we also present results by pure ideal MHD and Hall MHD models to emphasize the significance of the kinetic effects. Different from the previous work discussed above, we are not varying the plasma outflow from the ionosphere, hence the periodic oscillations observed are caused by the kinetic reconnection process embedded into the global MHD model.

The model description and simulation setup are described in section 4.2, the simulation results are presented in section 4.3 and we conclude in section 4.4.

4.2 Model Description and Simulation Setup

The simulations presented in this paper are conducted with the magnetohydrodynamics with embedded particle-in-cell (MHD-EPIC) model [Daldorff et al., 2014, Chen and Tóth, 2019]. The MHD-EPIC model two-way couples the BATS-R-US MHD code [Powell et al., 1999b, Tóth et al., 2008] and the implicit particle-in-cell code FLEKS [Chen et al., 2021] through the Space Weather Modeling Framework [Tóth et al., 2012]. The global magnetosphere structure is simulated by an ideal MHD model, with an embedded PIC region in the magnetotail to simulate the kinetic physics in the magnetic reconnection. The ionospheric electrodynamics is simulated by the Ridley Ionosphere Model (RIM) [Ridley et al., 2004] that solves a Poisson-type equation for the electric potential on a 2-D spherical grid, which is used to set the $\mathbf{E}\times\mathbf{B}$ velocity at the inner boundary of BATS-R-US. The MHD-EPIC model has been applied in studying multiple planetary and moon magnetospheres, such as the Earth [Chen et al., 2017],

Mars [Ma et al., 2018], Mercury [Chen et al., 2019b] and Ganymede [Tóth et al., 2016, Zhou et al., 2019, 2020b].

A three-dimensional block-adaptive Cartesian grid of BATS-R-US is used to cover the entire computational domain: $-224R_E < x < 32R_E$ and $-128R_E < y, z < 128R_E$ in GSM coordinates. The grid resolution is $1/4\,R_E$ between $-60R_E < x < 20R_E$, $-20R_E < y < 20R_E$ and $-16R_E < z < 16R_E$. A shell region near the Earth from $2.5\,R_E$ to $3.5\,R_E$ is covered with $1/8\,R_E$ grid resolution. The PIC box, the computational domain of FLEKS, is in the magnetotail between $-80R_E < x < -4R_E$, $-20R_E < y < 20R_E$ and $-10R_E < z < 10R_E$ with grid resolution $1/4R_E$. Figure 4.1 shows a 3-D overview of the simulation domain at $t = 3600\,\mathrm{s}$ from the simulation presented in this paper. The color contour is the mass density on the equatorial plane, and the magnetic field lines of two flux ropes are also plotted in the magnetotail. The black box is the PIC domain, which covers the tail region where magnetic reconnection could happen.

To reduce the computational cost and make the simulation feasible, the speed of light c is reduced to 15,000 km/s to speed up the implicit solver, and the ion-electron mass ratio m_i/m_e is decreased to 100 to increase the electron skin depth. These modification have no significant impact on the results at the ion and global scales. In addition to these numerical adjustments, we also scale up the ion and electron mass per charge by a factor of 16 to increase the ion inertial length so that it can be resolved with an affordable grid resolution. Tóth et al. [2017] presents theoretical arguments and numerical experiments and concludes that (1) the solution of the equations is not sensitive to the scaling at global scales and (2) the solution at the kinetic scale is proportional to the scaling factor but will look the same. The dipole tilt angle is set to 0° to form an idealized case. The solar wind condition applied at the inflow boundary of BATS-R-US is set to constant to study the magnetosphere's response to an idealized ICME solar wind driving. We have two solar wind conditions: a) $V_x = -600\,\mathrm{km/s}$, IMF $B_z = -15\,\mathrm{nT}$ for strong driving and b) $V_x = -400\,\mathrm{km/s}$, IMF $B_z = -5\,\mathrm{nT}$ for weak driving. The plasma number density and the temperature of the solar wind are fixed to $5\,\mathrm{cm}^{-3}$ and

10^5 K respectively. The solar wind velocity components V_y, V_z and IMF components B_x, B_y are all set to 0. Both strong and weak driving conditions are applied to the MHD-EPIC model to demonstrate that exceeding a threshold of the transported magnetic flux from the solar wind is necessary for triggering the sawtooth oscillation. We also run Hall MHD and ideal MHD models under strong driving to emphasize the importance of the kinetic reconnection.

We first run BATS-R-US and RIM for 15,000 steps using local time stepping with ideal MHD until the system reaches a quasi-steady state. Then the time accurate mode is turned on for 12 hours of physical time. The FLEKS model and/or the Hall MHD solver are switched on in the time accurate section.

4.3 Results

4.3.1 Occurrence of sawtooth-like oscillations

A characteristic signature of saw-tooth oscillations is the temporal variation of the magnetic inclination angle, which is defined as the angle $\alpha = \arcsin(|B_z|/B)$ between the magnetic field vector and the equatorial plane. Here B_z and B are the local magnetic field Z component and magnitude, respectively. The change of the magnetic inclination angle results from the field line stretching and dipolarization processes. At the geostationary orbit, the average minimum inclination angle of an observed sawtooth is 26° as compared to 43° for the isolated substorms [Cai et al., 2006]. Figure 4.2(a) shows the magnetic inclination angles observed at $r = 8\,R_E$ radial distance from the center of Earth, 9° latitude and 2 am magnetic local time (MLT). The corresponding GSM coordinates are $[x, y, z] = [-6.93, -4, 1.25]\,R_E$. Compared to the geostationary orbit, we are observing further toward the magnetotail because the variations detected at $6.6\,R_E$ are small. Due to the $\pm Z$ symmetry, the inclination angle is 90° in the equatorial plane, so we extract values slightly above that plane. As we will see later, the largest variation of the inclination angle occurs slightly off from the midnight

direction, this is why we chose 2 am MLT.

The dashed gray line is the result of the ideal MHD model with strong solar wind driving, and the simulated magnetosphere takes about 2 hours to converge to a steady solution. There is no perturbation of the inclination angle, which stays at about 50° for the entire simulation. The solid gray line shows the result from the Hall MHD model with strong solar wind driving, which takes about 1.5 hours to reach a quasi-steady state. However, unlike the ideal MHD model, the inclination angle oscillates around 60° with a ±5° range. The difference in the average inclination angles between the ideal MHD and Hall MHD models can be explained by the different reconnection modes resulting from the two models. Simulations show that the ideal MHD gives a Sweet-Parker type solution while the Hall MHD model gives a solution closer to the Petschek type [Murphy et al., 2009a]. Though they are different in the values of inclination angles, it is clear that there are no sawtooth-like oscillations in the ideal and Hall MHD simulation results.

The MHD-EPIC result with strong solar wind driving is shown by the solid red line, while the result of weak solar wind driving is plotted in green. The MHD-EPIC run with weak solar wind driving shows similar oscillation to the Hall MHD run, although with a smaller average inclination angle around 55°. The MHD-EPIC run with strong solar wind driving shows different inclination angle variations from the other three runs. After about four hours of the simulation, the inclination angle drops to about 30° from 55° with a recovering phase afterward. There are three sawteeth shown in Figure 4.2 (a) and their starting times are marked by dashed vertical lines at $t = 4.15\text{h}, 5.38\text{h}$ and 7.15h. The third sawtooth shows a small dipolarization during the stretching phase. Partial dipolarizations are consistent with observations as shown in the bottom panel of the figure. Panels (b) and (c) of Figure 4.2 compare the time variation of B_z from the MHD-EPIC simulation with strong solar wind driving and the observation from the POLAR satellite of the sawtooth event reported by Pulkkinen et al. [2006]. The POLAR satellite locations is around $x = -8.0\,R_E$ and $y = 3.5\,R_E$ and moves from $-2\,R_E$ to $2\,R_E$ on z direction in GSM coordinate. The absolute

values of B_z are different between the simulation and the observation because they are acquired at different positions, but the differences between the maximum and the minimum B_z for each sawtooth are around 40 nT in both. Furthermore, a partial dipolarization was observed by POLAR between 17 : 00 and 18 : 00 UT that is reminiscent of the simulation results between 9 and 10 hours.

From the four simulations with different setups presented in this section, we can conclude that two essential factors need to be satisfied for a global model to generate sawtooth-like oscillations without the time varying ionospheric outflow. First, the magnetic flux from the solar wind needs to exceed a certain threshold, which is also reported by [Cai et al., 2006] based on observations of many sawtooth events. Second, the tail reconnection needs to be simulated by the kinetic model.

4.3.2 Kinetic reconnection and sawtooth-like oscillations

In this subsection, we will investigate the connection between the sawtooth-like oscillations shown in Figure 4.2 and the kinetic reconnection process in the magnetotail. Panel (a) of Figure 4.3 shows the magnetic field, particle energy, and half of the total energy inside the PIC box normalized by the total energy at $t = 2\,\mathrm{h}$. The electric field energy oscillates around 0.06% percent of the total energy, which is negligible compared to the energy of the magnetic field and the particles. The magnetic field and particles have a periodic energy gain/loss accompanied with the sawtooth oscillations.

Before $t = 4.4\,\mathrm{h}$, there is no substantial energy transferred between the magnetic field and the particles. At $t \approx 4.4\,\mathrm{h}$, the E_{magnetic} starts increasing while the E_{particle} starts decreasing. This stretching phase (S1) ends at $t \approx 5\,\mathrm{h}$ when the difference reaches about 10%. In the next dipolarization phase (D1) the energy is transferred back from the magnetic field to the particles. The two parts of energy recover to the initial state at $t \approx 5.4\mathrm{h}$, which ends the first sawtooth period, and a similar oscillation starts at $t \approx 6\,\mathrm{h}$ and ends at $t \approx 7.5\,\mathrm{h}$ (S2 and D2). Panels (b)-(e) of Figure 4.3 depict the electron kinetic energy multiplied by the sign of the X

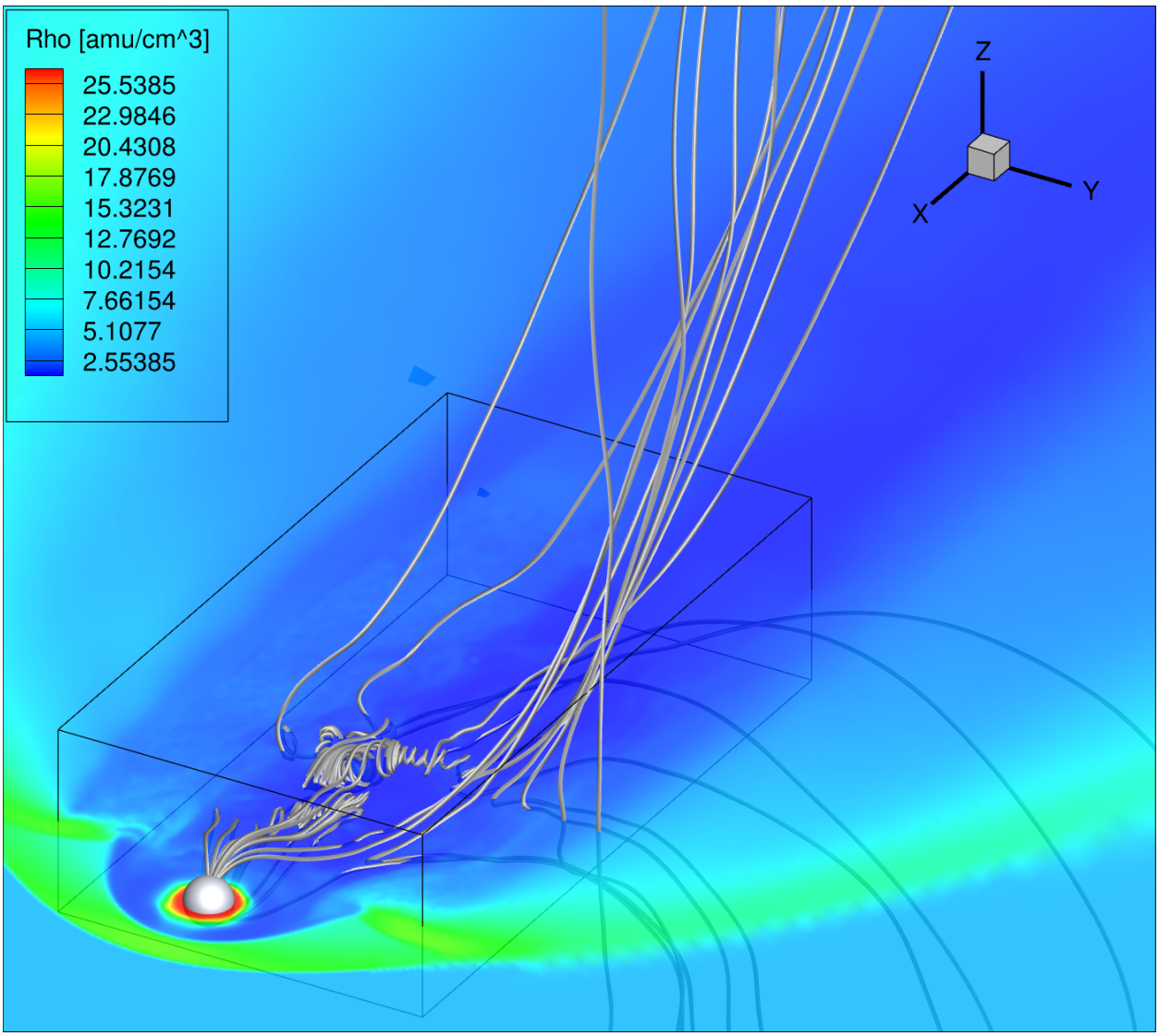

Figure 4.1: The global structure of Earth's magnetosphere at simulation time $t = 1$ h from the MHD-EPIC simulation with the strong solar wind driving condition. The color contour shows the mass density in the equatorial plane. The white spherical surface is the inner boundary at $2.5\,R_E$. The gray rods are magnetic field lines of two flux ropes in the magnetotail. The black box is the domain of the PIC model that covers potential magnetic reconnection sites in the tail.

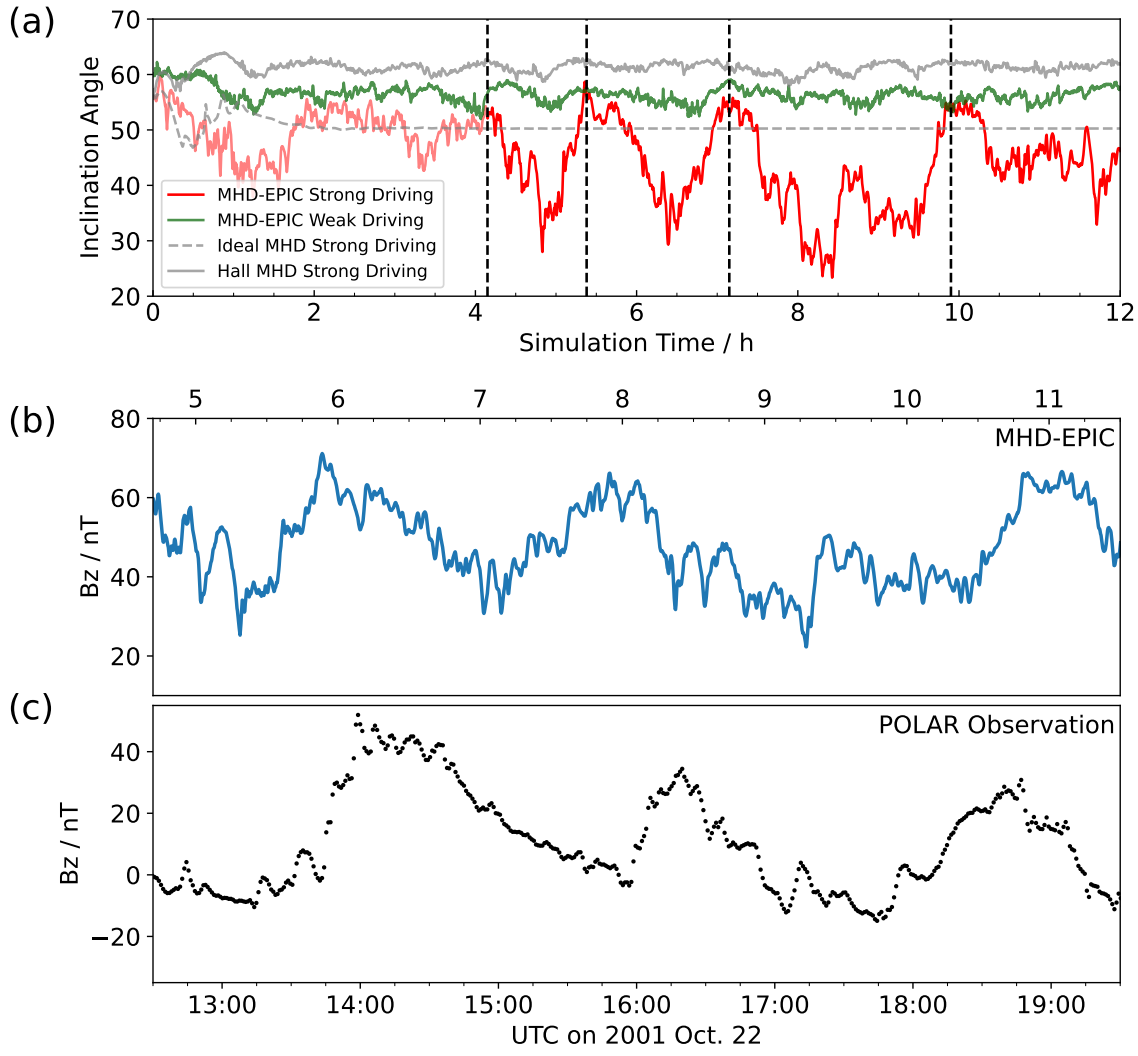

Figure 4.2: (a) Magnetic inclination angle plots from multiple simulations. MHD-EPIC with strong and weak solar wind driving conditions are shown in red and green. The ideal and Hall MHD results under strong solar wind driving are also plotted in gray for comparison. All inclination angles are taken at the same position: $x = -6.93\,R_E$, $y = -4\,R_E$ and $z = 1.25\,R_E$. (b) Time variation of B_z at the same position from the MHD-EPIC simulation with strong driving. (c) Sawtooth event observations of B_z by the POLAR satellite from $(-8.0, 3.5, -2)\,R_E$ to $(-8.0, 3.5, 2)\,R_E$ in GSM coordinate. (Figure 3 from Pulkkinen et al. [2006]).

component of the electron velocity that is defined as $K_e = \frac{1}{2}\rho_e u_e^2 \mathrm{sgn}(u_{e,x})$. The K_e values are plotted on the $B_x = 0$ isosurface, which is the middle of the tail current sheet. We choose the electron kinetic energy because the electron features are well localized, and the sign change of K_e accurately indicates the position of the reconnection X line. The two blue vertical lines labeled S1 and S2 in panel (a) are marked at $t = 4$h 48min and $t = 6$h 30min when E_{magnetic} reaches the maximum in each period and their corresponding E_k contour plots are shown in panels (b) and (d). In these panels, the magnetosphere is in a "stretching phase", when the X lines move towards the distant tail at $x \approx -40\,\mathrm{R_E}$. Another two red vertical lines labeled D1 and D2 in panel (a) are marked at $t = 5$h 14min and $t = 7$h 01min. Those two lines mark when E_{particle} (or E_{magnetic}) is increasing (or decreasing) most rapidly. Panels (c) and (e) show the corresponding E_k contour plots, when the magnetosphere is in a "dipolarization phase." In this phase, the X line is observed at $x \approx -15\,\mathrm{R_E}$ and the E_k near the X line is much larger. The "dipolarization phase" is also matching the recovery from the minimum inclination angle observed in Figure 4.2. The third sawtooth oscillation in the simulation is more complicated than the previous two. The dipolarization phase is interrupted by a secondary stretching from $t \approx 8$h 36min to $t \approx 9$h 24min. The third oscillation fully recovers to the initial state at $t \approx 10\,\mathrm{h}$. The period of the oscillations varies from 1.5 h to 3 h, which is very comparable with the observed periodicity.

4.3.3 Spatial distribution of the magnetic inclination angle

The wide extension of the variations of magnetic inclination angles in magnetic local time (MLT) is a critical signature of the sawtooth oscillations. Figure 4.4 shows the magnetic inclination contour plot from the MHD-EPIC simulation with strong solar wind driving conditions. The inclination angle is calculated along the circle $\sqrt{x^2 + y^2} = 7.9\,R_E$ in the plane $z = 1.26\,R_E$ (the inclination angle is 90° in the $z = 0$ plane due to the symmetry of this idealized setup). The location we are looking at is further from the center of Earth than the observations at the geosynchronous orbit reported by Cai et al. [2006]. Our MHD-EPIC

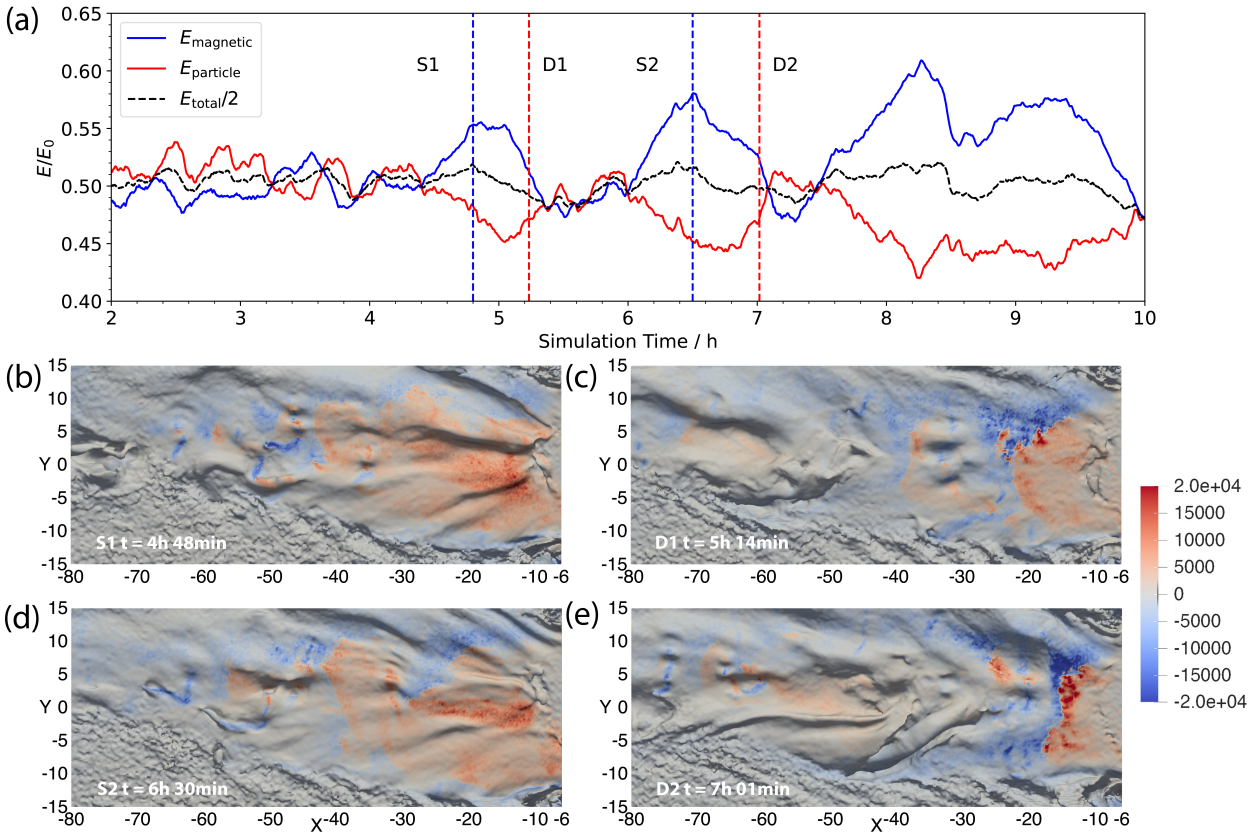

Figure 4.3: (a) The integrated magnetic field energy (blue) and particle energy (red) inside the PIC region normalized by the total energy at t=2h. The black line shows half of the normalized total energy. The four dashed vertical lines correspond to the the times depicted by panels (b)-(e), respectively, during the stretching (S1 and S2) and dipolarization (D1 and D2) phases. These plots show the color contours of the electron kinetic energy multiplied by the sign of the X component of the electron velocity: $K_e = \frac{1}{2}\rho_e u_e^2 \mathrm{sgn}(u_{e,x})$. The color contour is plotted on the $B_x = 0$ isosurface that identifies the middle of the magnetotail current sheet. Sharp jumps from dark blue to dark red color indicate reconnection jets emanating from the X-lines. The black shadows show that the current sheet surface is rippled.

simulation does not produce strong magnetic field perturbations at geosynchronous orbit. Despite the difference in the locations, the simulated inclination angle distribution over MLT exhibits several similarities compared to the observations. The minimum inclination angle from dawn to dusk is about 17°. The minimum inclination angle is close to observed sawtooth oscillations, indicating much stronger dipolarization happens in the MHD-EPIC simulation. The difference between the MHD-EPIC simulation and the observed sawteeth is caused by the location we are taking the samples: The closed field lines of the dipole field is stretched more further towards the tail. We can also observe that the 30° contour line spans from dawn to dusk. This broad span on MLT agrees with the observation. Moreover, the periodic stretching and dipolarization are demonstrated well from the two sawteeth shown in Figure 4.4. In addition to that, we can also identify that the inclination angle is smaller in the pre-midnight sector. The observations also demonstrate more prominent features on the dusk side. However, we honestly acknowledge that there are indeed three major discrepancies between the sawtooth oscillations from the MHD-EPIC simulation and observed sawteeth [Cai et al., 2006]. First, the signatures at the geosynchronous orbit are not strong enough to be observed. Second, the dipolarization at midnight is much weaker. The observed sawtooth oscillations exhibit the lowest inclination angle near midnight and expand towards dawn and dusk. Third, the duration of each sawtooth from the MHD-EPIC simulation is slightly less than 2 hours, which is shorter than a typically observed sawtooth that lasts from 2-4 hours. Hence, the magnetic reconnection rate simulated by the kinetic model can accumulate the magnetic open flux towards a higher threshold than the MHD models. This force imbalance between the dayside and the nightside is the major process that happens during the "stretching phase." One possible reason for the weaker oscillations at midnight the "critical level" of the accumulated magnetic flux simulated by the MHD-EPIC model is lower than reality at dawn and dusk. The reconnection that happens there first causes a much stronger dipolarization, which also dissipates the magnetic flux, which disables strong dipolarization at midnight.

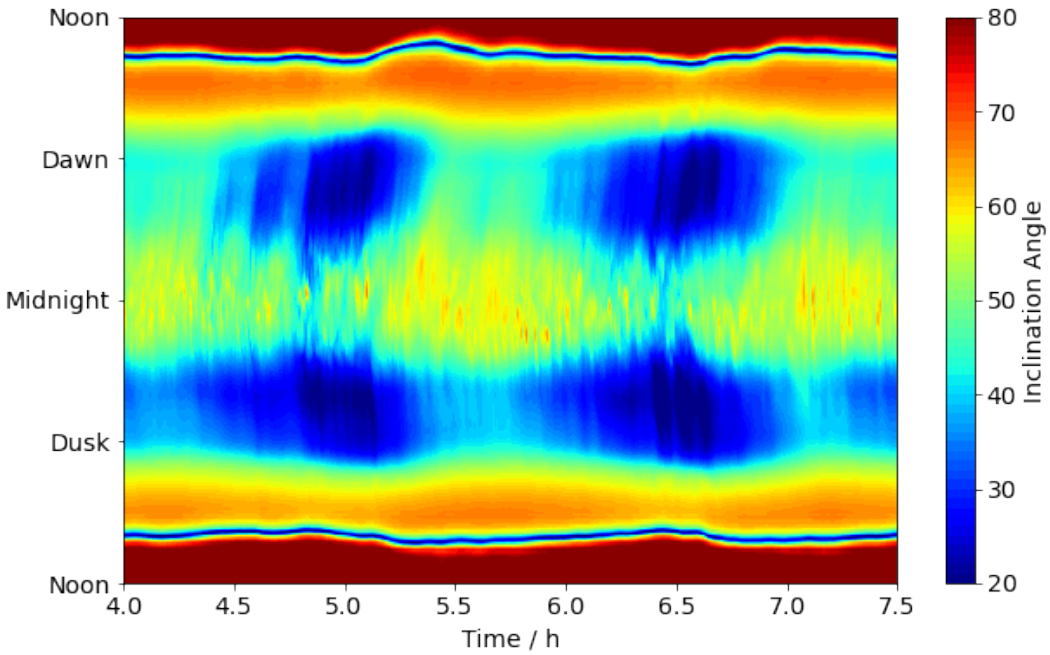

Figure 4.4: The contour plot of the magnetic inclination angle of the first two sawteeth from the MHD-EPIC simulation with strong solar wind driving. The inclination angle is evaluated on the circle $\sqrt{x^2 + y^2} = 7.9\,R_E$ in the plane $z = 1.26\,R_E$, which is outside the geosynchronous orbit.

4.4 Conclusion and Discussion

In this paper, we use the MHD with Embedded Particle-In-Cell (MHD-EPIC) model to study the role kinetic reconnection plays in generating magnetospheric sawtooth events. The PIC region covers a box region in the magnetotail where the reconnection could potentially happen. Different from prior MHD simulations of sawtooth events, there is no time varying ionospheric outflow transporting plasma to the magnetotail. We apply both strong and weak solar wind driving conditions in the MHD-EPIC simulations to demonstrate that the occurrence of the sawtooth oscillations depends on the incoming rate of the magnetic flux from the solar wind. To emphasize the significance of the kinetic model, we also perform the simulation using ideal MHD and Hall MHD models with the strong solar wind driving conditions for comparison.

We examine the temporal variation of the magnetic inclination angle in the near tail at $(x, y, z) = (-6.93, -4, 1.25)\, R_E$ from different simulations. We find that only the MHD-EPIC model with strong solar wind driving condition produces periodic oscillations of the magnetic inclination angle that has a minimum value below 30°, which demonstrates that both the kinetic magnetic reconnection and the incoming rate of the magnetic flux from the solar wind are essential to induce the sawtooth oscillations. We investigate the variations of magnetic and particle energy from the MHD-EPIC simulation. The energy is transferred from the particles to the magnetic field during the stretching phase. When the dipolarization starts, the energy transfers in the opposite direction. We also plot the electron kinetic energy contour on the current sheet surface, and we observe that the dipolarization phase of the sawtooth oscillation is related to the formation of a reconnection X-line close to the Earth. We find that the oscillations from the MHD-EPIC simulation exhibit a wide span over the magnetic local time that is a signature of observed sawtooth events. However, there are three major discrepancies between the MHD-EPIC generated sawtooth oscillations and the observations: 1. the signature at the geosynchronous orbit is relatively weak. 2. the simulated period of each sawtooth is slightly less than 2 hours compared to the observation,

which is 2-4 hours, 3. the minimum inclination angle in the simulation is found at the dawn and dusk regions rather than at midnight.

We suggest that the kinetic reconnection in the magnetotail can solely reproduce the periodic loading and unloading process of the magnetic flux in the magnetosphere. The reconnection rate in the magnetotail is not high enough to dissipate the incoming magnetic flux from the solar wind. Thus the imbalance between the dayside and nightside causes the magnetic flux to accumulate towards a critical level on the nightside and triggers dipolarization. This process is recognized as the direct causing mechanism of the sawtooth oscillations [Zhang et al., 2020]. Hence we conclude that in addition to the ionospheric outflow, the sawtooth oscillations might be an intrinsic feature of the kinetic reconnection in the magnetotail when the incoming magnetic flux from the solar wind exceeds a threshold. However, the discrepancies between the observation and the MHD-EPIC simulation suggest that ionospheric outflow is also an important factor. For example, the O^+ transported into the magnetotail will change the plasma components and potentially change the reconnection rate, which may extend the stretching phase. Also, the "preconditioning" by the nightside outflow mentioned by Zhang et al. [2020] might reduce the discrepancy at the midnight sector between the MHD-EPIC simulation and observations. In future work, we believe it is important to include both ionospheric outflow and kinetic magnetic reconnection physics in the magnetotail to fully understand sawtooth oscillations.

CHAPTER 5

Predicting Solar Flares with Machine Learning: Investigating Solar Cycle Dependence

This chapter was published in the *Astrophysical Journal* by Wang et al. [2020].

5.1 Introduction

Solar flares are energetic eruptions of electromagnetic radiation from the Sun lasting from minutes to hours. The terrestrial impact of small flares is limited, but strong flares have a significant on the upper atmosphere. Increased ionization affects the total electron content, which in turn affects radio wave propagation and global positioning system (GPS) accuracy. Ionospheric heating causes the atmosphere to expand, increasing the mass density and increasing drag on satellites altering their orbits. Strong flare are also often accompanied with coronal mass ejections (CMEs) that can cause substantial impact on the Earth environment. Therefore, it is very worthwhile to improve the prediction of solar flares, especially larger ones. During solar cycle 24, nearly 800 M or X flares were observed. While posing a significant threat, the rareness of extreme events and the complexity of the flares makes solar flare time and intensity predictions a very challenging task.

Although the triggering mechanism of solar flares and the factors determining the solar

flare strength are far from being well understood, it is shown by multiple studies that solar flares are caused by the sudden release of free energy brought by magnetic reconnection in the coronal field. What has come to be know as the standard model for flares and CMEs [Carmichael, 1964, Sturrock, 1966, Hirayama, 1974, Kopp and Pneuman, 1976] (also called the CSHKP model), involves the rise of sheared core or flux rope that results in magnetic reconnection in the surrounding arcade structure. Several variations of this model have been developed, which incorporate different initiation mechanisms [Masuda et al., 1994, Forbes and Acton, 1996, Manchester, 2003, Török et al., 2004]. A number of review papers summarize these works and many others [Green et al., 2018].

Since the photospheric magnetic field drives the coronal field, it is possible that the evolution patterns of the photospheric magnetic field may serve as indicators of the triggering process of flares and CMEs. Those features include the size of the active regions (AR), the integrated magnetic flux, the integrated current helicity, the magnetic field gradient measurements, the shear angle of the magnetic field structure and so on. The Helioseismic and Magnetic Imager (HMI) on the Solar Dynamics Observatory (SDO) satellite, launched a decade ago, has been providing high-cadence high-resolution photospheric vector magnetic field observations starting from 2010. The Space-weather HMI Active Region Patches, a.k.a. SHARPs [Bobra et al., 2014], contain time series data localized to individual active regions (ARs) with many pre-calculated quantities based on the AR magnetic field. We will use these SHARP quantities to train our machine learning model.

Machine learning, a sub-field of artificial intelligence, utilizes past data as a "learning context" for the computer program that allow it to make predictions of the future state of the system. The advent of the Solar Heliophysics Observatory (SOHO)/Michelson Doppler Imager (MDI) and SDO/HMI missions provided sufficient data for machine learning algorithms to predict solar activities. At first, the line-of-sight (LOS) component of the photospheric magnetic field measured by the MDI instrument was used by several groups to forecast solar flares using machine learning algorithms (Ahmed et al. [2013], Huang et al. [2018], Song

et al. [2009], Yu et al. [2009], Yuan et al. [2010]). The support vector machine (SVM) algorithm was used by Boucheron et al. [2015] for a classification task on time series of MDI data from 2000 to 2010. However, the LOS magnetic field component does not include all the magnetic field information, so later studies used the vector magnetic field data once it became available from the HMI instrument. Bobra and Couvidat [2015] used the SVM trained with SHARP parameters for active region classification tasks. Nishizuka et al. [2018] built a residual deep neural network using not only the parameterized photospheric magnetograms but also using chromospheric images. Jonas et al. [2018] used observations from photosphere, chromosphere, transition region, and corona as input of the machine learning algorithm, which gave a comparable result to the works done by Bobra and Couvidat [2015] and Nishizuka et al. [2018].

The machine learning algorithms in these studies mentioned so far do not fully utilize the time dependence of the input. Among various kinds of machine learning algorithms, recurrent neural networks (RNNs) are suitable to analyze time series input. Long-short term memory networks (LSTMs) [Hochreiter and Schmidhuber, 1997, Gers et al., 2000], a particular kind of RNNs, have succeeded in many sequence classification and prediction tasks, including speech recognition, time-series forecasting, handwriting recognition and so on [Franklin, 2005, Graves et al., 2013]. Most recently, Liu et al. [2019], Chen et al. [2019a] and Jiao et al. [2019] used LSTMs on SHARP parameters, which achieved better performance for predicting solar flares compared to previous works. Sun et al. [2019] identifies key signals for strong flares from SHARP parameters using time-series clustering on LSTMs predictions.

In this paper, we apply the LSTM algorithm on the SHARP parameters from SDO/HMI vector magnetic field to predict the maximum solar flare class produced by an active region in the next 24 hours. The inputs are 24-hour time series of SHARP parameters with 12-minute cadence. The observations of ARs are time sequences, hence LSTMs are suitable for this kind of input. First, our results show consistency with recently published work by Liu et al. [2019] that also uses the LSTM algorithm. Second, we also find that the skill scores

vary substantially when using different years of ARs in the training and testing set. This indicates that data samples should be carefully chosen for the model evaluation. It is also of interest to understand in what respect these years differ in the solar cycle from each other that may make the solar flare prediction less or more successful.

The rest of this paper is organized as follows. Section 5.2 describes how we collect data and build the training and testing sets. Section 5.3 describes the LSTM architecture we are using in this work. Section 5.4 explains the metrics used to evaluate the model performance. Section 5.5 shows the results of this study and compares them with previous work. The solar cycle dependence of the prediction skills are also presented in this section. Section 5.6 describes our conclusions.

5.2 Details of the Data Preparation

5.2.1 Dataset

We use SHARP summary parameters as the input data of the prediction model. The Space-weather HMI Active Region Patches (SHARPs) is a data product derived from vector magnetograms taken from the *Helioseismic and Magnetic Imager* (HMI) onboard the *Solar Dynamics Observatory* (SDO) [Bobra et al., 2014]. The summary parameters are calculated based on the *HMI Active Region Patches* (HARPs), which are rectangular boxes surrounding the active regions that are moving with the solar rotation and the evolution of the active regions. Table 5.1 lists the 20 key parameters used in this work. The SHARP summary parameters are downloaded for all active regions from the Joint Science Operations Center (`jsoc.stanford.edu`) from 2011 to 2018. The solar flare events are identified from the NOAA Geostationary Operational Environmental Satellites (GOES) flare list [Garcia, 1994]. In the GOES flare list, flare events are listed with class, start, end, and peak intensity times of each event. The peak time of the flare events are assigned as the "event time" when constructing the data samples. The number of active regions and flare events in different years

are summarized in Table 5.2. Note that C flares outnumber the A and B flares suggesting that most of the A and B flares are missed when their relatively weak signal falls below the X-ray background.

The input of our model are the 24-hour long time series (that we call sequences) extracted from the full time series of SHARP summary parameters of active regions. To guarantee the quality of the data, some time sequences are dropped, especially when the active regions are at the limb. The criteria for dropping unqualified time sequences are as follows:

1. In order to avoid projection effects, the longitude of the HARP region center is within the range of $\pm 68^\circ$ from the central meridian,

2. The fraction of missing frames in a time sequence has to be less than 5%,

3. The starting time of two time sequences are separated by one hour.

The target value (or label) of each sequence is the maximum flare class produced by the active region in the next 24h after the end time of the sequence. The NOAA active region number is used to match the HARP and AR numbers in the GOES flare list. However, while GOES flares are identified strictly with NOAA ARs, we note that a single AR may be split among multiple HARPs or that a HARP may contain multiple ARs. Consequently, we find that 20% of HARPs have this mismatch issue, which may lead to a potential error when we assign the maximum flare classes to the time sequences for flares may be missed or improperly attributed to the HARP.

Because the various SHARP features have different scales and units, the original data samples are normalized before input into the machine learning model: let z_i^n denote the normalized value of the i^{th} feature in the n^{th} data sample, then

$$z_i^n = \frac{v_i^n - \mu_i}{\sigma_i}, \tag{5.1}$$

where v_i^n is the original value of feature i in data sample n, while μ_i and σ_i are the mean and standard deviation of the feature i calculated from the entire dataset, respectively.

Parameter	Description
USFLUX	Total unsigned flux in Maxwells
MEANGAM	Mean inclination angle, gamma, in degrees
MEANGBT	Mean value of the total field gradient, in Gauss/Mm
MEANGBZ	Mean value of the vertical field gradient, in Gauss/Mm
MEANGBH	Mean value of the horizontal field gradient, in Gauss/Mm
MEANJZD	Mean vertical current density, in mA/m^2
TOTUSJZ	Total unsigned vertical current, in Amperes
MEANALP	Total twist parameter, alpha, in 1/Mm
MEANJZH	Mean current helicity in G^2/m
TOTUSJH	Total unsigned current helicity in G^2/m
ABSNJZH	Absolute value of the net current helicity in G^2/m
SAVNCPP	Sum of the Absolute Value of the Net Currents Per Polarity in Amperes
MEANPOT	Mean photospheric excess magnetic energy density in ergs per cubic centimeter
TOTPOT	Total photospheric magnetic energy density in ergs per cubic centimeter
MEANSHR	Mean shear angle (measured using B_{total}) in degrees
SHRGT45	Percentage of pixels with a mean shear angle greater than 45 degrees in percent
SIZE	Projected area of patch on image in micro-hemisphere
SIZE_ACR	Projected area of active pixels on image in micro-hemisphere
NACR	Number of active pixels in patch
NPIX	Number of pixels within the patch

Table 5.1: List of SHARP parameters and brief descriptions

Year	ARs	A	B	C	M	X
2011	168	1	665	1002	106	9
2012	168	0	475	1115	124	7
2013	183	0	469	1197	97	12
2014	194	0	184	1627	194	16
2015	143	0	446	1274	128	2
2016	109	0	757	294	15	0
2017	52	0	620	229	37	4
2018	21	5	255	12	0	0

Table 5.2: Number of active regions and flares of different classes observed each year.

5.2.2 Training/Testing splitting

In order to assess the performance of the machine learning algorithms properly, we need to split the samples (time sequences of SHARP summary parameters and corresponding maximum flare classes) into a training set and a testing set. The training set is used for training the machine learning model while the testing set is for assessing the prediction capability of the model. In the training process, the model learns from the input data and adjusts its parameters to fit the ground truth. Both variable selection and parameter estimation are included in this process. The samples in the testing set should be totally separated from the training set, otherwise there will be an artificial gain of performance since the information in the training set is leaked to the testing set [Kaufman et al., 2012, Schutt and O'Neil, 2013]. Hence, separating the samples based on active regions is necessary to guarantee that sequences from one active region will not occur in both training and testing sets simultaneously. All the training/testing splitting in this paper are conducted based on HARPs.

5.3 Architecture of Machine Learning Model

The Recurrent Neural Network (RNN) is a category of neural networks which can make use of sequential information [Pearlmutter, 1989]. This architecture is naturally used in solar flare prediction since the active regions evolve with time and the occurrence of the solar flares is most likely related to the time-dependent evolution of active regions. RNNs are called recurrent because they perform the same task for every input from the sequence, but the output depends on the previous computations. Among various RNN structures, the Long Short Term Memory (LSTM) network is one of the most commonly used type of RNNs [Hochreiter and Schmidhuber, 1997]. LSTM networks are explicitly designed to avoid the long-term dependency problem, which is a major shortcoming for simpler RNNs. The key to LSTMs is a new cell state variable in the network, which is passed through the whole chain

with only minor linear interactions. This allows the information at a much earlier time to effect the results, which mimics a 'long-term' memory.

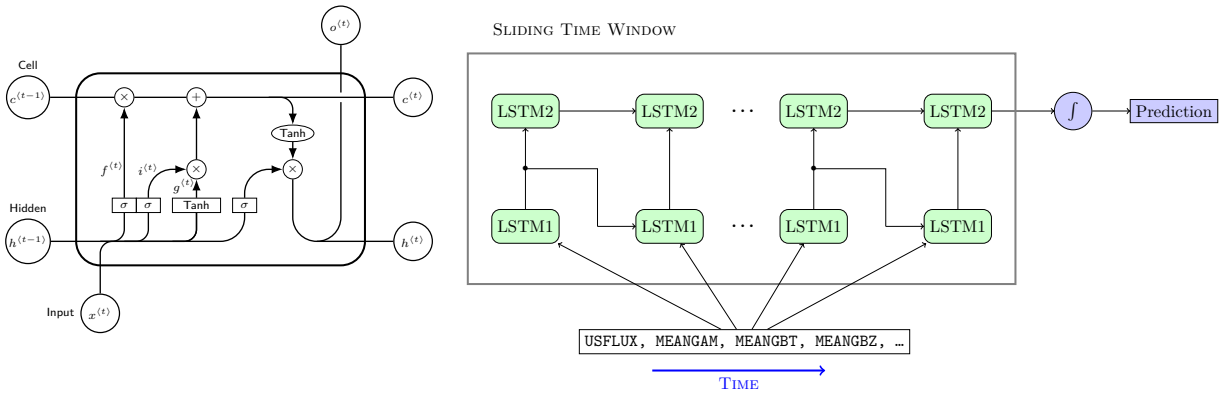

Figure 5.1: The detailed structure of the LSTM cell (left) and the LSTM network (right).

The structure of the LSTM unit and the LSTM network used in this work is shown in Figure 5.1. The left panel shows a single LSTM unit. Each unit takes an input vector $x^{<t>}$ consisting of the input features at a certain time point t, the hidden state $h^{<t-1>}$ and the cell state $c^{<t-1>}$ are from the previous LSTM unit. The right panel shows the structure of the two-layer LSTM network. The LSTM units in the second layer are the same as in the first layer, but their input vectors $x_2^{<t>}$ are the output vectors $o_1^{<t>}$ from the first layer LSTM units. The relationships between the unit input, output and internal states are given by the following equations:

$$i^{<t>} = \sigma(W_{ii}x^{<t>} + b_{ii} + W_{hi}h^{<t-1>} + b_{hi}) \tag{5.2a}$$

$$f^{<t>} = \sigma(W_{if}x^{<t>} + b_{if} + W_{hf}h^{<t-1>} + b_{hf}) \tag{5.2b}$$

$$g^{<t>} = \tanh(W_{ig}x^{<t>} + b_{ig} + W_{hg}h^{<t-1>} + b_{hg}) \tag{5.2c}$$

$$o^{<t>} = \sigma(W_{io}x^{<t>} + b_{io} + W_{ho}h^{<t-1>} + b_{ho}) \tag{5.2d}$$

$$c^{<t>} = f^{<t>} * c^{<t-1>} + i^{<t>} * g^{<t>} \tag{5.2e}$$

$$h^{<t>} = o^{<t>} * \tanh(c^{<t>}) \tag{5.2f}$$

Here $x^{<t>} \in \mathbb{R}^d$ is the input vector to the LSTM unit and d is the number of features. $i^{<t>}$, $f^{<t>}$ and $o^{<t>} \in \mathbb{R}^h$ are the activation vectors of the input gates, forget gates and output gates, respectively. $g^{<t>} \in \mathbb{R}^h$ is an activation vector from the tanh function. h is the hidden dimension of the LSTM unit, which is a hyperparameter in the model that reflects the model complexity and we use 16 in this work. $c^{<t>} \in \mathbb{R}^h$ is the cell state vector and there is only linear relationship between the output and input cell states in a single LSTM unit. The cell state and hidden state vectors are passed to the next LSTM unit in the same layer. The output vectors in the first layer are taken as input in the second layer. The output vector of the last LSTM unit in the second layer is multiplied by a h vector and passed to a sigmoid function to generate the final prediction value. The tanh and the sigmoid function

$$\sigma(x) = \frac{1}{1 + e^{-x}} \tag{5.3}$$

introduce the non-linearity into the neural network. The $W_{i\_} \in \mathbb{R}^{h \times d}$ weight matrices are applied to the input vectors and $W_{h\_} \in \mathbb{R}^{h \times h}$ are applied to the gate activation vectors. $b \in \mathbb{R}^h$ in the equation are the bias vectors. The weight matrices and bias vectors are trainable parameters, which are determined during the training process. Our LSTM model is different from the model of Liu et al. [2019]. We use two layers of LSTM and the output

comes from the last LSTM cell of the second layer. Liu et al. [2019] use one layer of LSTM cells and the output is fed into a fully connected network.

The "training" in the machine learning is essentially an optimization process for an objective function, also known as the loss function. The loss function measures the difference between the model prediction and the ground truth. An optimization algorithm is used to minimize the loss function so that the trainable parameters in the model can "encode" some knowledge from the data samples. The prediction can finally be reduced to a binary classification task: according to the given input, will this AR produce a flare of class Γ in the next 24 hours. The model will generate a prediction score in the last layer in the network and if this score is larger than a threshold, then the model will make a positive prediction. In our work, the last layer is a sigmoid function and the output from a sigmoid function is either close to 0 or 1, so the threshold for binary classification is set to be 0.5. The "Binary Cross Entropy" is typically used as the loss function for binary classification problems. However, this loss function can fail if one category of samples is dominating the entire data set. Constantly predicting the dominant category in the testing set can result in a small value of the loss function but the model has no predictive skill in this case. Large energetic solar flares are extremely rare events so that the dataset we are using is highly unbalanced. To solve this issue, we used "Binary Cross Entropy with Logits Loss" in this work which is defined as:

$$L = \frac{1}{N}\sum_{n=1}^{N} -[p_c y_n \log \sigma(\hat{y}_n) + (1 - y_n)\log(1 - \sigma(\hat{y}_n))] \tag{5.4}$$

Here N is the number of samples in the training or testing set, y_n is the target value and $\hat{y}_n$ is the model output. The coefficient p_c and the use of the sigmoid function distinguish this loss function relative to the simple binary cross entropy loss function. The sigmoid function improves the numerical stability in the optimization process, while p_c is set to the ratio of negative and positive samples from the training set to balance the contributions of the two terms in the sum. This approach is the same as what is used by Liu et al. [2019]

	2011	2012	2013	2014	2015	15-18
$\geq$ C	3.91	4.08	4.27	4.46	4.35	4.35
$\geq$ M	29.41	30.30	31.25	34.48	34.48	34.48

Table 5.3: The ratio of negative and positive sample p_c in the loss function for different training sets.

and Nishizuka et al. [2018] in their cost functions. The values of p_c for different training sets in this paper are presented in Table 5.3.

5.4 Model Evaluation

The four quantities TN, TP, FN, and FP refer to the number of True Negative, True Positive, False Negative and False Positive predictions, respectively. These four numbers can be combined to calculate the Precision, the Recall (also known as Probability of Detection, POD), the False Alarm Rate (FAR, also known as Probability of False Detection or False Alarm, PFD or PFA), the True Skill Statistic (TSS), the Heidke Skill Score (HSS), and the Accuracy (ACC) defined as

$$\text{Precision} = \frac{\text{TP}}{\text{TP} + \text{FP}} \tag{5.5a}$$

$$\text{POD} = \text{Recall} = \frac{\text{TP}}{\text{TP} + \text{FN}} \tag{5.5b}$$

$$\text{FAR} = \text{PFA} = \frac{\text{FP}}{\text{FP} + \text{TN}} \tag{5.5c}$$

$$\text{TSS} = \frac{\text{TP}}{\text{TP} + \text{FN}} - \frac{\text{FP}}{\text{FP} + \text{TN}} = \text{POD} - \text{FAR} \tag{5.5d}$$

$$\text{HSS} = \frac{2(\text{TP} \cdot \text{TN} - \text{FP} \cdot \text{FN})}{(\text{TP} + \text{FN})(\text{FN} + \text{TN}) + (\text{TP} + \text{FP})(\text{FP} + \text{TN})} \tag{5.5e}$$

$$\text{ACC} = \frac{\text{TP} + \text{TN}}{\text{TP} + \text{FP} + \text{FN} + \text{TN}} \tag{5.5f}$$

$$\tag{5.5g}$$

We will use these quantities to evaluate the model performance. The Precision and POD evaluate the model's ability to identify positive events (1 being perfect, 0 being worst), while FAR tests the model for correctly identifying negative events (0 being perfect, 1 being worst). The Accuracy, TSS and HSS evaluate the overall skill with the maximum value 1 being the perfect score. As we will see, the various skill scores have very different dependence on the fraction of positive and negative events in the training and testing sets. For an imbalanced dataset, the Accuracy becomes less meaningful because the model's output will be dominated by the majority of the dataset. Artificial inflation will be caused to the POD (or the FAR) if the model is assigning all testing samples to be positive (or negative). However, in both cases, the model will not have any useful prediction skills. TSS approaches the POD when the forecasting is dominated by correct forecasts of non-occurrence which is the case for solar flare events. Notice that TSS is defined by two terms TSS = TP/(TP+FN) - FP/(FP+TN). Thus, if the model overpredicts the flare occurrence, both terms increases but the second term only changes slightly because the TN is very large. A high TSS value therefore may not really mean that the prediction is reliable, as there can be many false alarms relative to the number of true predictions. HSS is superior to the TSS in this situation, because it produces 0 value for a model that predicts a random number with the correct occurrence rate, and positive HSS means that the model is better than that. However, HSS is sensitive to the ratio of positive versus negative events, which means that the same model can produce very different HSS values depending on the selected data set (for example solar maximum versus solar minimum). In other words, HSS can be scaled up if there are more positive samples in the testing set [Doswell III et al., 1990].

The goal of a predictive model is to minimize some cost function. A simple cost function can be constructed in the following way. Suppose the amount of (financial or other quantifiable) loss saved by taking action thanks to a positive prediction is S, while the cost of taking action due to a false alarm is C. Then the expectation value of the cost function can be expressed as

$$E = N \cdot \mathrm{FAR} \cdot C - P \cdot \mathrm{POD} \cdot S \tag{5.6}$$

where P and N are the total number of positive and negative events. Dividing the equation by $P \cdot C$ results in a normalized expectation value

$$e = \mathrm{FAR} \cdot \frac{N}{P} - \mathrm{POD} \cdot \frac{S}{C} \tag{5.7}$$

If the ratios S/C and N/P are equal, then equation (7) is proportional (with a negative sign) to the TSS, so in this special case TSS is optimal to evaluate and compare the usefulness of models with respect to minimizing the cost function. However, if N/P is much larger than S/C, then a low FAR score is more important than maximizing POD. We don't have good values for estimating S and C and in general they vary with event types. Hence there is no single skill score that can properly evaluate the forecasting performance, and one needs to be careful when models are compared. There are only four independent values (TN, TP, FN, and FP) and only their three ratios truly matter. This means that any three independent values defined above can be used. In practice, we concentrate on the POD, FAR and HSS values, as these provide complete and intuitive information about the model's performance. The TSS, while useful, is not an independent skill score, as it is simply the difference of POD and FAR.

5.5 Results

5.5.1 Training Process

The LSTM network is implemented in Python with the PyTorch package. PyTorch is originally a tensor calculation package for GPU and the auto-gradient feature [Paszke et al., 2017] makes it suitable for machine learning tasks. A minibatch strategy [Li et al., 2014, Bottou et al., 2018] is used for faster convergence during back-propagation. The Adam optimizer

[Kingma and Ba, 2014]is used with the learning rate set to 0.001 and the other parameters are $\beta_1 = 0.9$ and $\beta_2 = 0.999$. The batch size is 1000. The model is trained for multiple epochs on the training set. In each epoch, the model goes through the training samples once. The model is trained for 6 epochs to generate the results presented in Table 5.5, Figure 5.3 and Figure 5.4. We found no statistically significant improvement in the performance after six epochs. To account for the randomness due to the order of training samples and the initial values of the trainable parameters, we perform 20 independent runs with different random seeds to get robust results.

5.5.2 Skill scores for solar flare prediction

The prediction results from the models in this work are summarized in Table 5.4. The contingency table shows the number of TP, TN, FP and FN events. Notice that the mean values of 20 runs are reported here, so the results are not integers. TN is large because of the imbalanced dataset. TP for predicting $\geq C$ flares is much larger than predicting $\geq M$ flares. This is the result of more $\geq C$ flares. FP is also large which indicates that the model overpredicts the occurrence of the flare.

The mean values of the skill scores for the 20 runs are reported in Table 5.5 together with results obtained by earlier work for comparison. From Table 5.5, the skill scores POD, TSS and FAR are better for predicting $\geq M$ flares than $\geq C$ flares while the Precision and HSS show the opposite trend. The higher HSS is partially explained by the larger fraction of positive samples for $\geq C$ flares [Doswell III et al., 1990]. However, essentially all skill scores for predicting any flares ($\geq A$) are worse than predicting $\geq C$ flares. The reason for this reduced performance is that A and B flares are not properly observed. The number of flares in different energy classes roughly obey a power-law distribution (see Lu and Hamilton [1991] and Figure 5.8), thus a large number of class B flares are missing in the GOES flare records (see Figure 5.2). The X-ray emission of many B flares can fall below the background emission level once an active region heats up, which causes those B flares to be unrecorded.

LSTM-2015		P	N	LSTM-15_18		P	N
$\geq M$	P'	396.55	889.6	$\geq M$	P'	513.20	1343.45
	N'	182.45	13531.4		N'	189.80	25953.55
$\geq C$	P'	2043	995.65	$\geq C$	P'	2762.35	1605.60
	N'	1135	10826.35		N'	1683.65	21948.40

Table 5.4: Contingency table of LSTM model in this work. The mean values of 20 runs are presented. P and N means the real observed positive and negative samples, P' and N' refers to the prediction results.

Therefore, we are training and testing the model with mislabeled data samples for predicting any class of flares, hence many weak flares that the model predicts probably are classified as false positives, which lowers the skill scores.

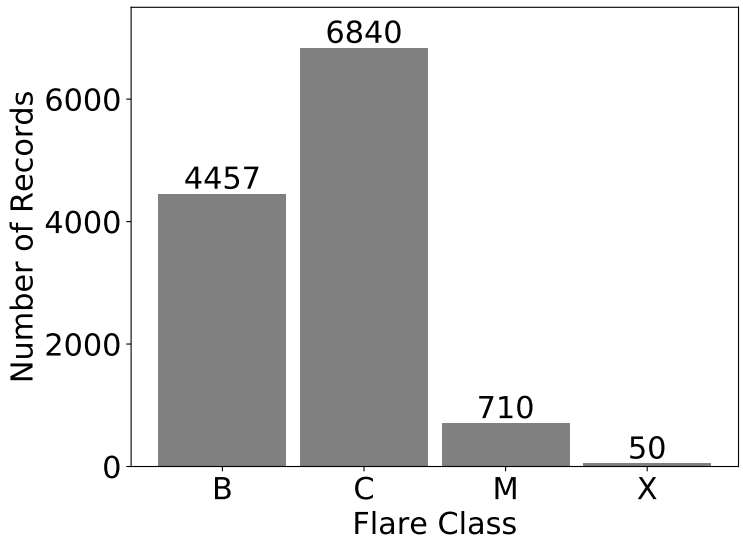

Figure 5.2: The distribution of number of recorded flares for classes B, C, M, X from 2011 to 2018 in the GOES data set. Note that the number of B flares is much smaller than the number of C flares.

5.5.3 Comparison with previous results

In this subsection, we will compare the results of this paper to previously published works. In the past decade, there have been several works that applied machine learning based models to predict solar flares. Those models including MLP (Multilayer perceptrons) [Florios et al.,

2018], SVM (Support Vector Machine) [Qahwaji and Colak, 2007, Yuan et al., 2010, Bobra and Couvidat, 2015, Boucheron et al., 2015, Muranushi et al., 2015, Florios et al., 2018], DeFN (Deep Flare Net) [Nishizuka et al., 2018] and a recently published work [Liu et al., 2019] which also used LSTM network.

The skill scores for different models are shown in Table 5.5. Even though the input and the testing samples may be different in those works using MLP, SVM and DeFN models, the results are representative of the best performance those models can achieve on the solar flare prediction task. The results from the LSTM models outperform the MLP, SVM and DeFN models substantially on HSS and FAR. The TSS from the DeFN is higher than what from the LSTM model, this is because of the high POD produced by the DeFN. Meanwhile, DeFN produces much higher FAR which reduces the reliability of the positive predictions from the DeFN. The difference of the skill scores indicates that taking time series data into account can improve solar flare forecasting. As discussed in subsection 5.5.4, we should use similar testing sets when citing the various models since different train/test splitting can produce different skill scores. The notations for LSTM models are defined as follows: LSTM-15_18 and LSTM-2015 are the models used in this paper. LSTM-15_18 uses ARs from year 2015 to year 2018 for testing and LSTM-2015 uses ARs in year 2015 for testing. LSTM-Liu uses the model reported in Liu et al. [2019] which uses ARs in year 2015 for testing. Among those evaluation metrics, [1] Accuracy (ACC) is the least useful since the data set is highly biased (flare events are rare so the majority samples in the testing set are negative), predicting those negative samples correctly leads to a high accuracy, however not much predictability for strong flare events may actually be achieved. [2] Precision and POD reflect the model's ability of making positive predictions: Precision is the fraction of correctly predicted samples among all predicted positive samples. POD is the fraction of correctly predicted positives among the actual positive samples in the testing set. Therefore Precision provides more useful information about predictability of rare events, while POD by itself is not representative of the predictive skills. From Table 5.5, our model produces

Precision scores within the same range as Liu et al. [2019], and is better than the previous works listed. [3] HSS and TSS are often considered as good metrics for evaluating model predictability in binary classification tasks. However, TSS benefits from the large number of correctly predicted negative samples (TN) so that it is much higher than the HSS in all tests. HSS lessens the importance of true negatives (TN) but it is more sensitive to the fraction of positive samples in the testing set: the value of HSS will be higher if there are more positive samples in the testing set (which can be artificially achieved by creating a testing set that contains larger fraction of positive samples than the actual data). Our model gives better HSS than previous models (MLP, SVM and DeFN) that do not use time sequences and also has similar performance as the recently published results [Liu et al., 2019] using LSTM, which validates the correctness of this work. [4] The FAR for predicting $\geq C$ and $\geq M$ flares are all less than 0.1, which means that more than 90% negative predictions from our model are correct. This contributes greatly to the high HSS values. Notice that both the POD and FAR in our results are lower than those from LSTM-Liu, and our model produces fewer false alarms.

The details of our and the Liu et al. [2019] LSTM models are different but they obtain similar skill scores according to Table 5.5. This suggests that both LSTM models extract most of the useful information from the SHARP parameters and further improvement will require using more information from the observation.

5.5.4 Choosing different testing years

As described before in section 5.2.2, it is important to totally separate the training and testing samples. However, whether choosing different years of flares for testing can have different skill scores is still unclear since the previous works all used data before 2015 for training and after 2015 for testing. In this subsection, we conduct the training-testing process on different combinations of training and testing years. In Figure 5.3, we present the box plots of skill scores for twenty independent runs with the testing samples being one of the years

Metric	Model	$\geq M$ class	$\geq C$ class	Any Class
POD	MLP	0.812	0.637	-
	SVM	0.692	0.746	-
	DeFN	0.947	0.809	-
	LSTM-Liu	0.881	0.762	-
*	LSTM-2015	0.685	0.643	0.625
*	LSTM-15_18	0.730	0.621	0.530
Precision	MLP	0.143	0.451	-
	SVM	0.106	0.497	-
	DeFN	0.180	0.529	-
	LSTM-Liu	0.222	0.544	-
*	LSTM-2015	0.311	0.677	0.670
*	LSTM-15_18	0.282	0.635	0.702
ACC	MLP	0.855	0.778	-
	SVM	0.824	0.803	-
	DeFN	0.858	0.822	-
	LSTM-Liu	0.909	0.829	-
*	LSTM-2015	0.929	0.858	0.814
*	LSTM-15_18	0.945	0.883	0.800
HSS	MLP	0.204	0.389	-
	SVM	0.141	0.472	-
	DeFN	0.263	0.528	-
	LSTM-Liu	0.347	0.539	-
*	LSTM-2015	0.394	0.567	0.519
*	LSTM-15_18	0.382	0.557	0.473
TSS	MLP	0.669	0.449	-
	SVM	0.520	0.562	-
	DeFN	0.802	0.634	-
	LSTM-Liu	0.790	0.607	-
*	LSTM-2015	0.623	0.559	0.509
*	LSTM-15_18	0.681	0.553	0.439
FAR	MLP	0.143	0.188	-
	SVM	0.172	0.184	-
	DeFN	0.145	0.175	-
	LSTM-Liu	0.091	0.155	-
*	LSTM-2015	0.062	0.084	0.116
*	LSTM-15_18	0.049	0.068	0.092
P/N	DeFN	0.034	0.244	-
	LSTM-Liu	0.029	0.243	-
*	LSTM-2015	0.040	0.269	0.371
*	LSTM-15_18	0.026	0.189	0.403

Table 5.5: Comparison of skill scores for different models. Lines with * are results from this work. LSTM-2015 uses the same time period ase DeFN while LSTM-15_18 uses the same time period as LSTM-Liu for the testing data set. The number ratio of positive and negative samples are also reported in this table.

from 2011 to 2015, and the other four years are used for training. (As shown by Table 5.2, there were very few large flares from 2016 to 2018, so those years are not suitable for testing and would not contribute much to training either.)

Figure 5.3 shows that training on 2011 to 2014 and testing on 2015 gives the best HSS and FAR scores for predicting both $\geq C$ and $\geq M$ flares. The trend is different for the TSS for predicting $\geq M$ flares, because TSS is dominated by the POD values, but this does not mean truly good prediction for rare events, such as $\geq M$ flares. Good prediction of rare events requires very few false alarms and this will produce high HSS. Apparently, the model is quite "restrained" on making positive predictions for the year 2015 data, which improves its FAR and HSS scores. It is clear from Figure 5.3 that evaluating the model performance on different years will introduce significant differences in the results.

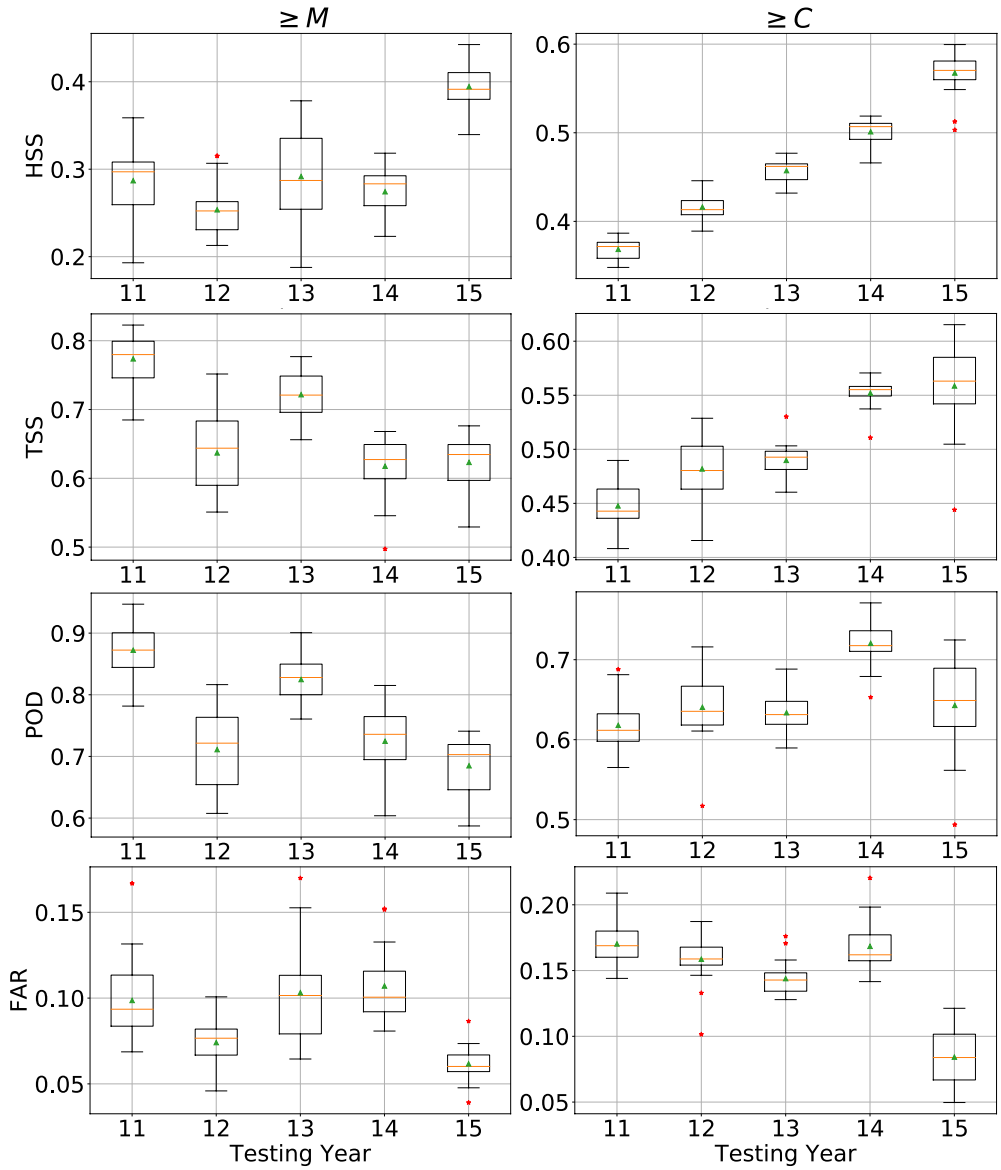

Figure 5.3: The box plots of four skill scores for different training and testing year choices in the 2011−2015 data set. Note that smaller FAR means better performance. The left and right columns show results for predicting flares of class ≥ M and ≥ C flares, respectively. The yellow line is the median and the green triangle is the mean of the 20 independent training runs. The lower and upper bounds of the boxes correspond to the first and third quartiles Q_1 and Q_3. The upper and lower error bars are at $Q_3 + 1.5(Q_3 - Q_1)$ and $Q_1 - 1.5(Q_3 - Q_1)$, respectively. The red stars show the data points outside the error bars (outliers). The mean value and median are calculated including the outliers.

To investigate why the model produces fewer false alarms on year 2015 than other years, we set up two linear regression models (LRM) as the baseline. These two baseline models use

the same training and testing samples as the LSTM model. The time sequences of SHARP parameters are reshaped to one-dimensional vectors as the input of the first linear regression model, denoted by LRM-A. The elements of the reshaped one dimensional vector is in the following order: $[f_1^1, \ldots, f_T^1, \ldots, f_1^N, \ldots, f_T^N]$, f_t^n is the value of n^{th} feature at time t. For the second linear regression model, denoted by LRM-B, the mean values of the time sequences are taken as input. Twenty independent runs are conducted and the mean values of the skill scores from the LSTM model and two baseline models are shown in Figure 5.4. The difference between the LSTM model and the LRM-A is the non-linearity introduced by the LSTM network. The LRM-B eliminates the time sequence information and only inputs the average level of activity into the model. From Figure 5.4: [1] For predicting $\geq M$ flares, the LSTM gives the best HSS, followed by LRM-A and LRM-B. For predicting $\geq C$ flares, the LSTM model has similar HSS as the LRM-A model and both are better than the LRM-B model. This illustrates the importance of the time sequence information. [2] The linear regression models give larger POD and FAR than the LSTM. Therefore, the LSTM model has less tendency to make positive predictions, which results in better HSS. The optimal case is when the model produces high POD while also keeping a low FAR, which is not the case for an LSTM. This is the reason why an LSTM cannot provide a high TSS compared to linear regression models.

The entire time sequence data taken by LRM-A results in better HSS, TSS and FAR scores than LRM-B that uses the average parameter values of the input sequence. This shows that even for simple linear models, time sequence information helps the model to make better predictions. Notice that the LSTM model gives better HSS and FAR than the linear regression models, while the TSS and POD are similar or even smaller than LRM-A. This means that the non-linearity introduced by LSTM networks is effective to improve HSS and FAR but not for TSS and POD. All three models give the lowest FAR when the model is tested on year 2015. All three models give the lowest FAR when the model is tested on year 2015. This indicates that, regardless of the different algorithms, the temporal

averaged SHARP parameters are relevant to the result of FAR, as well as the time sequence parameters. In conclusion, the LSTM model produces more reliable positive predictions than the simple linear regression models although it will miss more positive events. The model gives different results when being tested/trained on different years of data, apparently due to differences in the average SHARP parameters.

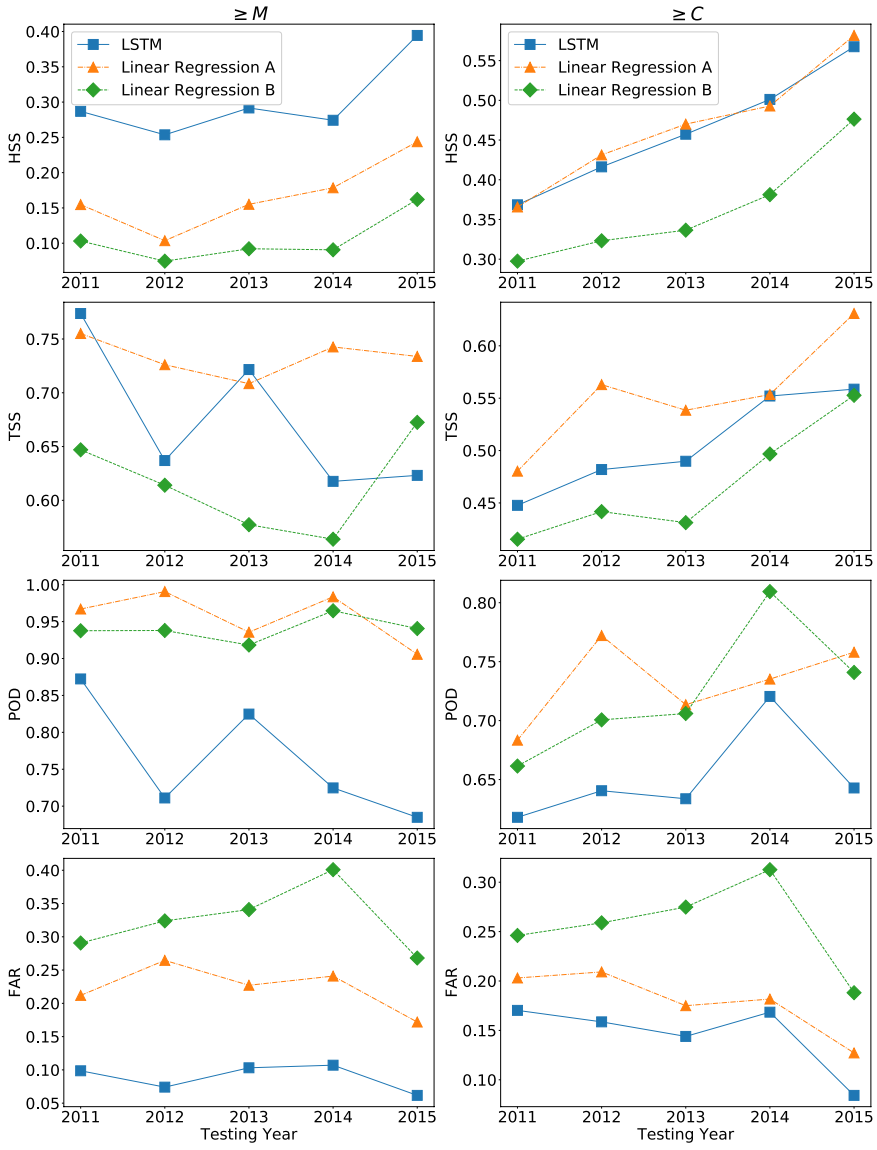

Figure 5.4: The comparison between LSTM model and two baseline linear regression models. Four skill scores are presented. Left column is the prediction for $\geq M$ flare and right column is for $\geq C$ flares. The Linear Regression A takes the whole time sequence as input (same as LSTM) and the Linear Regression B takes the mean value of the time sequence for each SHARP parameter.

5.5.5 Training/Testing on different solar cycle phases

According to subsection 5.5.4, training and testing on different years leads to very different results. One possible reason for the difference could be the changes in the data processing procedure. However, from Hoeksema et al. [2018], although the data processing techniques were modified in January, 2015, those changes will not have major effects on the data products used in this work.

To investigate if there are any intrinsic differences of the active regions from each year in the solar cycle, we first do the training and testing separately on each year. Since the number of active regions and flares is very small in years 2016 to 2018, those three years are grouped together. Four skill scores are collected to evaluate the model performance: HSS, TSS, POD and FAR. The process for selecting data samples is:

1. For active regions in each year, randomly select 25% for testing and rest of them for training.

2. Extract 24h time series of SHARP parameters for training and testing from active regions selected in step 1 and label the time series with the maximum flare class in the next 24 hours from the GOES flare record.

3. Randomly drop negative samples in the training and testing sets to fix the ratio of positive samples and negative samples to be 0.05 for predicting $\geq M$ flares and 0.3 for predicting $\geq C$ flares.

Notice that in step 3, we fix the ratio of positive to negative samples to make the HSS directly comparable across different years. In addition, having a fixed positive/negative sample ratio makes the HSS and TSS behave similarly. We perform multiple runs with randomly dropping negative samples, so in fact the runs use different data sets. For each run, the skill scores are the mean values of the model outputs from the third to the tenth epochs. This range of epochs is chosen based on the typical evolution of skill with epochs: there is an initial rapid improvement, followed by a plateau with random oscillations, and finally worsening

trends due to overfitting. The averaging over multiple epochs reduces the random variation due to the relatively small data sets. In addition, the mean values better reflect the general performance of the model than picking the best epoch for each run.

The box plots of skill scores for predicting $\geq C$ flares are shown in Figure 5.5. Each box contains 100 data points from 100 runs using randomly selected active regions for training/testing and dropping negative samples in the data sets. Because there are few active regions and flare events during the three years from 2016 to 2018 (see Table 5.2), the skills scores are less centered and the number of outliers is larger than those from other years. The results show that training and testing on the data after 2015 produces better skill scores than the earlier years. The FAR has the most substantial difference for data sets after and before 2015, which is also the major reason for better HSS and TSS since the POD does not vary much. We are not showing results for predicting $\geq M$ flares on each year separately because the $\geq M$ flares are too rare to give any statistically significant results on such small data samples.

The results in Figure 5.5 show that the prediction model has better performances for the years 2015-2018 than for 2011-2014. To demonstrate this difference with better statistics, we conduct the training/testing process on two data sets using these two time periods, and compare the results. The data selecting strategy is the same as what we did for training/testing on each year but now there are enough M and X flares to produce statistically robust results. The skill scores for predicting $\geq C$ and $\geq M$ flares are shown in Figures 5.6 and 5.7, respectively. For predicting $\geq C$ flares, the HSS, TSS scores are clearly and significantly better for 2015-2018 than for 2011-2014. The box plots of POD overlap with each other while the box plots of FAR are well separated. This result indicates that for capturing $\geq C$ flares in the testing set, the model has similar performance when trained on the data samples from two phases in a solar cycle. However, the model will produce much fewer false alarms if it is trained on data samples from the declining phase in a solar cycle. For predicting $\geq M$ flares, according to Figure 5.7, the difference of skill scores is less obvious. In general, the

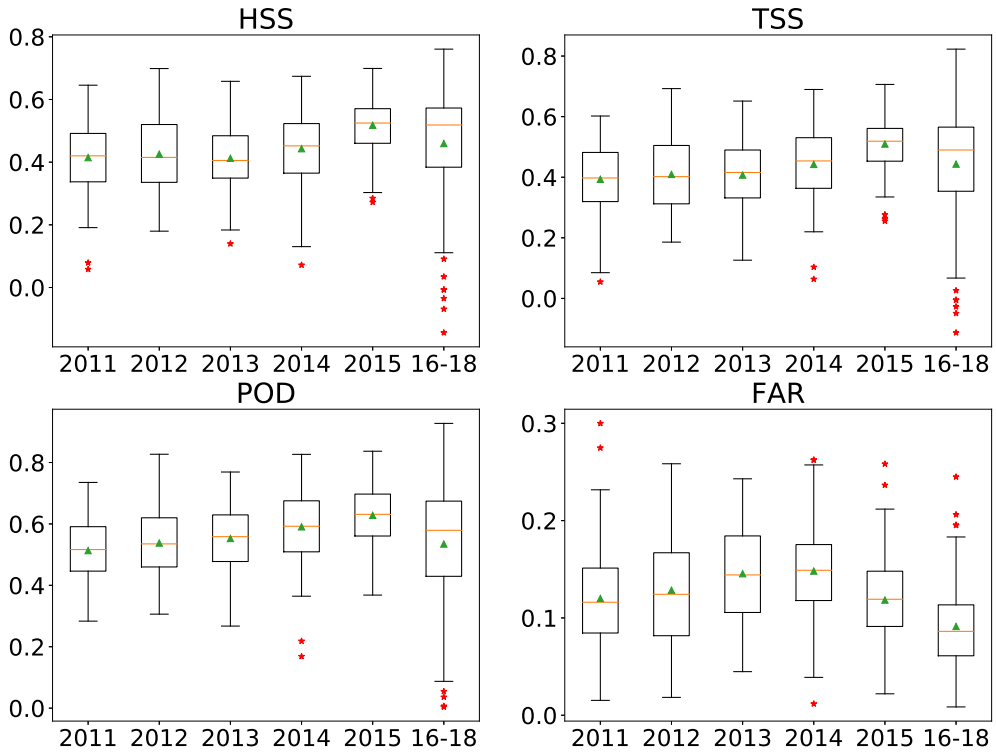

Figure 5.5: The box plots of skill scores for predicting $\geq C$ flares on different years from 2011 to 2018. The symbols in the figures are the same with previous box plots.

results from 2015-2018 show larger variance because there are fewer $\geq M$ flares in this time range. The box plots of HSS, TSS and POD overlap to a large extent except the model gives a higher FAR when trained/tested on year 2015-2018.

There is a significant difference between 2011-2014 and 2015-2018 for predicting $\geq C$ flares, but not for $\geq M$ flares. A simple explanation could be different flare intensity distributions in two phases of a solar cycle. For example, if the frequency of C and M flares are better separated from each other in one of the time periods (i.e. there are relatively fewer flares with energies near the C/M class boundary) then it will help the model to correctly identify $\geq$ M flares. To check this possibility we show the distribution of flare events as a function of energy on a log-log scale for the two time periods in Figure 5.8. The histograms are well approximated with straight lines, indicating that the flare intensity distributions approximately follow power laws [Lu and Hamilton, 1991]. While the amplitudes are differ-

ent by about a factor of 3 (there are more flares during solar max than during solar min), the slopes of the two lines are very close to each other. So there is no obvious difference in the shape of the flare intensity distributions between the two phases of a solar cycle. There seems to be some excess of flares near the C/M class boundary for 2015-2018, which may contribute to the worse performance on predicting $\geq$ M flares than $\geq$ C flares for this time period. However, we set the threshold of positive and negative classes to C8.0. All these excess of flares are labeled as positive. The results show no difference in skill scores for two time periods. Thus we conclude that difference of the skill scores in Figure 5.6 and 5.7 cannot be simply explained by different flare intensity distributions in the two time periods. A further possible explanation could be the coupled eruptions (or sympathetic flares) between different active regions [Moon et al., 2002, Titov et al., 2012]. Sometimes one flare occurring in one active region leads to the occurrence of another flare(s) in other active regions. There are more active regions from year 2011 to 2014 and it is anticipated that more sympathetic flares occur in this time range. The SHARP parameters may not contain enough information to predict sympathetic flares.

5.6 Conclusion

In this paper, we build a data set covering active regions from 2010 to 2018 from Joint Science Operations Center (`jsoc.stanford.edu`). Each data sample is the time sequence of twenty SHARP parameters, which represent the magnetic field properties of an active region. We develop an LSTM network to predict the maximum flare class Γ in the next 24 hours produced by an active region. The prediction task is reduced to a binary classification when Γ is a combination of classes above a certain threshold. We consider three different cases for Γ: $\geq M$, $\geq C$ and $\geq A$. The last case corresponds to predicting any flares. The training/testing splitting is based on active regions, which guarantees that the model is tested on data samples that it has never seen previously. The skill scores produced by the

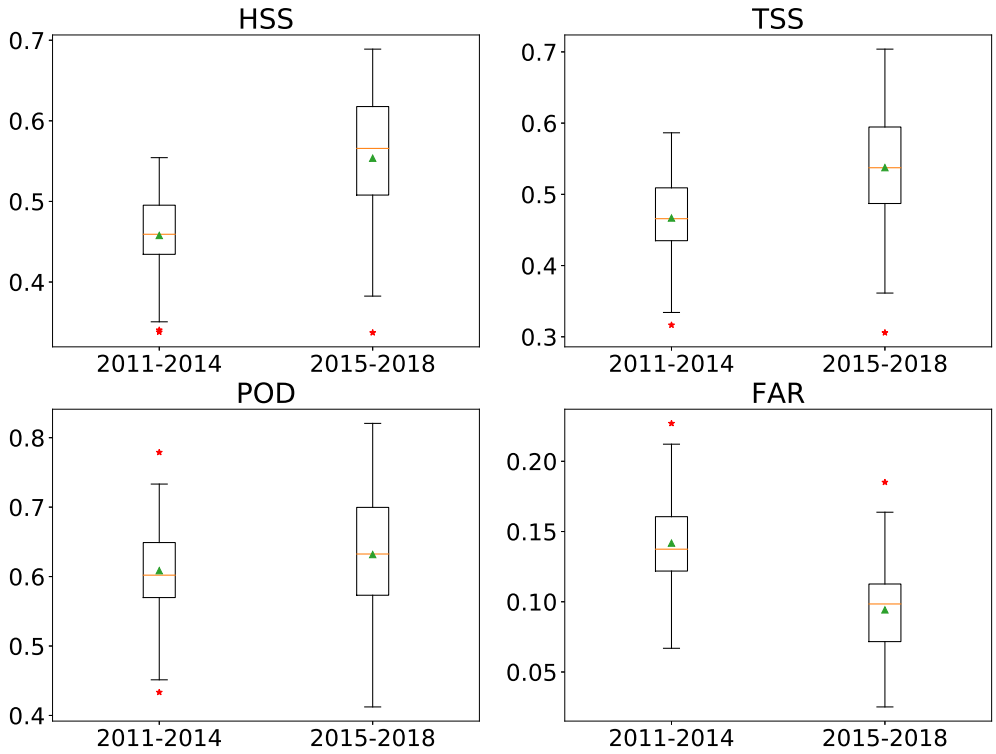

Figure 5.6: The box plots of skill scores for predicting $\geq C$ flares. The training/testing are conducted within one of two time periods: 2011-2014 and 2015-2018. The symbols in the figure are the same as in previous box plots.

model vary substantially for different years and we investigate the solar cycle dependence of the model performance. The main results of this paper are summarized as follows:

1. Flare prediction models should minimize the cost function that is not necessarily proportional or even vary monotonically with the various skill scores. This means that comparison of model performance requires caution.

2. The LSTM based model achieves better HSS for predicting solar flares than the previous approaches such as MLP, SVM and DeFN. Using the time series information improves relevant skills. Our results are also comparable with the recently published work using a similar LSTM method.

3. Although more than 50% percent of skill scores of LSTM model can be acquired from simple linear regression models, the non-linearity introduced by LSTM reduces the

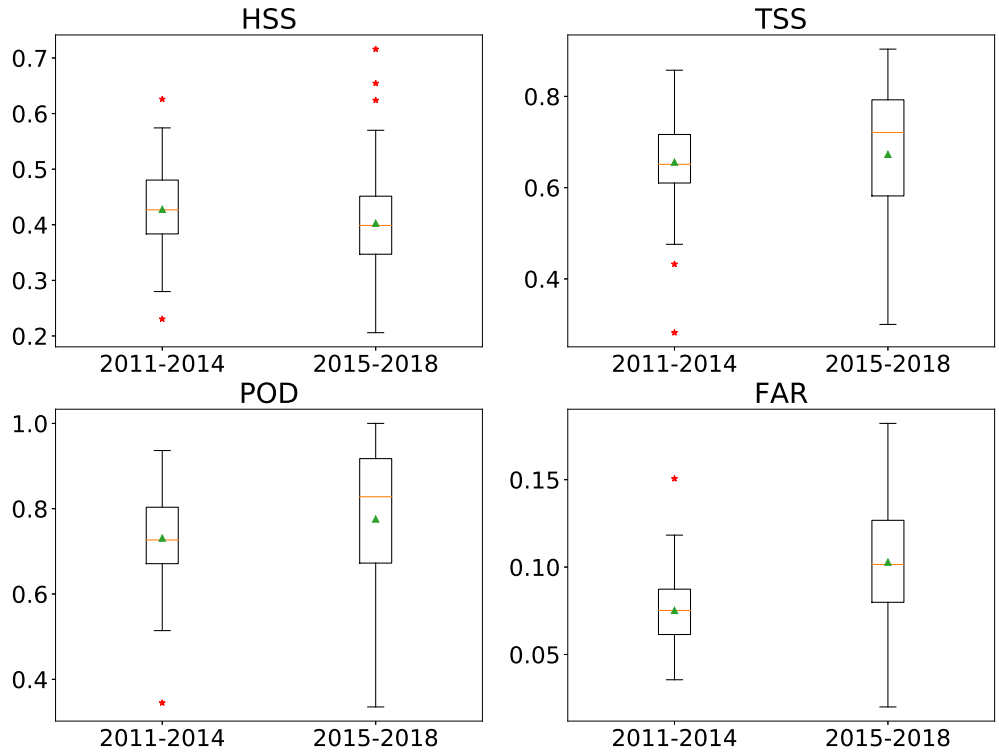

Figure 5.7: The box plots of skill scores for predicting $\geq M$ flares. The training/testing are conducted within one of two time periods: 2011-2014 and 2015-2018.. The symbols in the figure are the same as in previous box plots.

number of false alarms and improves the prediction skills of the model.

4. Previous works using active region data after 2015 for testing could introduce bias into the skill scores. If the model is trained on 2011-2014 and tested on 2015, it produces better skill scores than other combinations of training and testing years. This appears to be related to the difference of the time sequence averaged values of the SHARP parameters used for the input, although the physical interpretation is not revealed. A possible way to avoid this issue is to mix active regions from different years both in the training and the testing sets.

5. The skill scores from the model show statistically significant variation when different years of data are chosen for training and testing. The years 2015 to 2018 have better TSS, HSS and FAR for predicting $\geq C$ flares than the years 2011 to 2014 when the

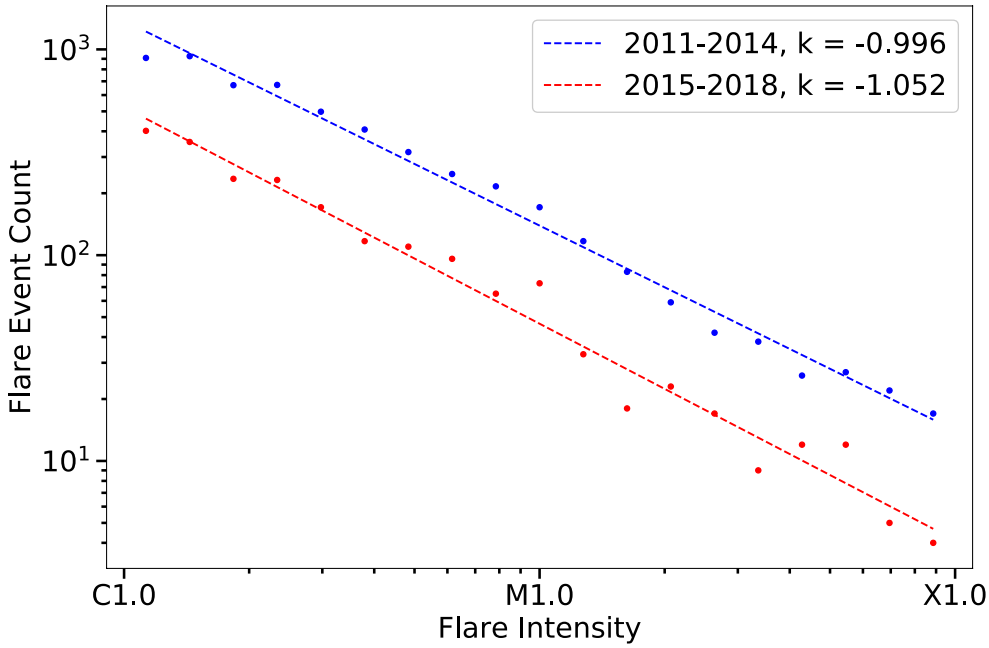

Figure 5.8: The histogram for C and M flares in two groups of years. The plot is in log-log scale and the histograms are straight lines which shows the intensity of flares agrees with the power-law distribution.

difference in flare occurrence rates is properly taken into account.

Based on the results presented in this paper, the LSTM is a valid method for the solar flare prediction task. The skill scores from this paper are very close to those generated by other different LSTM models indicates that the information contained in the SHARP parameters is limited. In future work, we plan to use more observational information to further improve the flare prediction skills.

CHAPTER 6

Conclusions

As presented in the previous chapters, there are three major studies I conducted in this dissertation:

1. I have developed a novel MHD with Adaptively Embedded Particle-In-Cell (MHD-AEPIC) model and validated it through a geomagnetic storm simulation.

2. I have investigated the role of kinetic physics in magnetospheric sawtooth oscillations.

3. I have developed a new, machine learning-based solar flare forecasting model.

More details about the conclusions of the presented studies are described in this chapter. In the end, I propose possible further investigations on these topics.

6.1 Summary of Results

In the first study of this dissertation, we have presented a newly developed MHD with Adaptively Embedded Particle-In-Cell (MHD-AEPIC) model. The PIC grid cells can be turned on and off during the simulation due to the adaptive grid feature introduced by the PIC model FLEKS. This feature enables the PIC regions to move with the reconnection sites to save the computational cost substantially. We introduce three physics-based criteria to determine the reconnection regions in the magnetotail. A geomagnetic storm event happened on 2011-08-06 with minimum Dst around $-120\,nT$ is simulated by the MHD-AEPIC model.

The flapping motion of the magnetotail current sheet during the storm emphasizes the advantage of the adaptation feature of the MHD-AEPIC. We also simulate the same event using ideal MHD and Hall MHD models, and we examine the results at multiple physical scales:

1. The SYM-H and SME indexes are investigated as the global scale features, reflecting the equatorial and auroral region disturbances, respectively. All three models produce reasonable agreements of the global scale disturbances such as the main phase of the storm or the increase of the auroral electrojet with the observations. However, no significant difference is found among the three different models, which implies that the global magnetosphere configuration of the three models is very close. The kinetic model embedded in the magnetotail does not improve the global scale feature for this specific geomagnetic storm.

2. For the mesoscale features, we compare the magnetic field components and ion profiles between the Geotail observation and the simulation outputs. In this storm event, MHD-AEPIC and ideal MHD models produce a similar agreement with the in-situ observations of Geotail. We also compare the three models with respect to flux rope structures in the current sheet. Only one major flux rope can be observed from the ideal MHD simulation at the selected time, while Hall MHD and MHD-AEPIC tend to produce more flux ropes at a wider range along the dawn-dusk direction.

3. The MHD-AEPIC model well reproduces the electron scale kinetic physics. We collect electron macro-particle velocities at the magnetic reconnection's inflow, outflow, and electron diffusion regions (EDR). The velocity distribution functions (VDFs) at the inflow and outflow regions agree well with the theoretical arguments and other PIC simulations. The VDF at EDR shows excellent agreement between the simulation and the MMS3 observation [Hwang et al., 2019]. This demonstrates that MHD-AEPIC can produce electron scale physics within a single self-consistent global model.

In the second study of this dissertation, we use the MHD with Embedded Particle-In-Cell (MHD-EPIC) model to investigate the role of kinetic effects in the magnetospheric sawtooth oscillations. A PIC box is applied in the magnetotail to simulate the kinetic reconnection. The external solar wind driving is constant with a southward IMF B_z. Both strong and weak solar wind driving conditions are applied in the MHD-EPIC simulations. To emphasize the significance of the kinetic model, we also perform the simulation using ideal MHD and Hall MHD models with the strong solar wind driving conditions for comparison. The MHD-EPIC model can produce sawtooth oscillations without a time-varying ionospheric outflow, while MHD models cannot yield similar features. This suggests that the kinetic reconnection in the magnetotail can solely reproduce the periodic loading and unloading process of the magnetic flux. The reconnection rate in the nightside simulated by the kinetic model is possibly closer to the reality that cannot dissipate the incoming magnetic flux from the dayside. The magnetic flux can accumulate in the nightside and then triggers the dipolarization that is pointed as the direct mechanism of the sawtooth oscillations [Zhang et al., 2020]. Hence, we conclude that sawtooth oscillations might be an intrinsic feature of the magnetosphere. We also acknowledge discrepancies between the simulation outputs and the observations, which means ionospheric outflow is a significant contributing factor to the sawtooth oscillations.

In the third study presented in this dissertation, we switch from the first-principle models to machine learning methods and investigate the solar flare forecasting problem. We build a data set of solar flares covering active regions from 2010 to 2018 from Joint Science Operations Center (`jsoc.stanford.edu`). We employ an LSTM network to predict the maximum flare class Γ in the next 24 hours produced by an active region. The LSTM model achieved better HSS than previous models, and using the time-series information improves relevant skills. Despite illustrating the advantage of the LSTM model, we also point out that the skill scores show statistically significant variation when the training/testing splitting is performed on different combinations of years. The years 2015 to 2018 have higher TSS, HSS, and FAR for predicting $\geq C$ flares than the years 2011 to 2014, when the difference in flare occurrence

rates is appropriately considered.

6.2 Future Work

The results from the first and second studies in this dissertation exhibit an interesting perspective: the effects of kinetic physics in a global magnetospheric simulation are not that straightforward. If the external solar wind is strong and variant, it is unlikely that the kinetic physics can affect larger physical scales, such as the global indexes. However, if the external solar wind is constant, the magnetosphere is more likely to evolve along with its intrinsic physical laws. Thus kinetic physics affects the global features. Hence, we are interested in applying the MHD-AEPIC model to more magnetospheric simulations under various solar wind conditions and model setups for future work. Here are several tasks that can be explored in the future:

1. Covering both the dayside and tail reconnection sites with PIC regions in one simulation. This would enable more realistic reconnection at the magnetopause, which is significant for the energy transported into the magnetosphere.

2. Using the MHD-AEPIC model to simulate more geomagnetic storms, eventually extreme ones. So far, we only have one storm event that is simulated with kinetic physics. The overall performance of the MHD-AEPIC model on storm simulations is still unknown.

3. Studying the particle energization process in the magnetosphere. Current simulations only investigate the particle velocity distributions. However, suprathermal particles are often observed. The MHD-AEPIC model is perfect for investigating their heating and accelerating mechanisms in a global context.

The solar flare forecasting in this dissertation shows tremendous potential for the machine learning model in space weather applications. However, there are still open questions in the

field, and several of the most important ones are listed below:

1. *Enough information?*

   Although the LSTM model achieves good skill scores with the SHARP parameters as input, it is still far from enough to establish a reliable forecasting system. One possible reason is that the SHARP parameters lose too many features from active regions. Solar images from magnetograms and extreme ultraviolet channels potentially contain more information. Building machine learning models utilizing these extra data would help understand what information is needed to make a good forecast.

2. *Interpretable models?*

   Can we distill some knowledge from a machine learning model and improve our understanding of the sun-earth system? So far, the machine learning models are like black boxes. Making interpretable machine learning models would help us improve the model performance and understand the critical factors in the complicated physical processes in space weather.

3. *Too often too quiet?*

   Space weather data sets are typically imbalanced: many days of quiet conditions and a few hours of storms, or thousands of weak flares and dozens of strong flares. This poses a serious problem in any machine learning algorithm that finds patterns in the data. It is also problematic for defining meaningful metrics that actually assess the ability of a model to predict interesting events, as we discussed in the Chapter 5. The first-principle models can produce a large amount of data when certain extreme conditions, like storms or X flares, are rare to happen in nature. One possible solution is to use simulation data in the machine learning pipeline.

APPENDIX

Reconnection Due to Numerical Resistivity

It is a common practice to rely on numerical resistivity to mimic reconnection physics in global ideal and Hall MHD simulations. Analytic solutions of ideal MHD obey the frozen-in condition: the magnetic flux through a surface co-moving with the plasma (i.e. the ion fluid) does not change. For Hall MHD the magnetic flux is frozen into the motion of the electron fluid. A consequence of the frozen-in condition is that if two plasma elements are connected by a field line, then they remain connected forever, which means that magnetic reconnection cannot take place.

In reality, and also in the kinetic PIC model, the electrons and ions can "detach" from the magnetic field lines in the ion and electron diffusion regions, respectively. In effect, this allows the magnetic field lines to reconnect inside the electron diffusion region where the frozen in condition does not apply. The simplest mathematical description of this process is adding an Ohmic resistive term $\eta\mathbf{j}$ into the induction equation:

$$\frac{\partial \mathbf{B}}{\partial t} = -\nabla \times [-\mathbf{u}_e \times \mathbf{B} + \eta \mathbf{j}] \tag{.1}$$

For constant resistivity η one can write this as

$$\frac{\partial \mathbf{B}}{\partial t} = -\nabla \times [-\mathbf{u}_e \times \mathbf{B}] + \eta' \nabla^2 \mathbf{B} \tag{.2}$$

where we used $\mathbf{j} = (1/\mu_0)\nabla \times \mathbf{B}$, defined the magnetic diffusivity $\eta' = \eta/\mu_0$ and exploited the

divergence-free condition $\nabla \cdot \mathbf{B} = 0$. The usual argument in favor of using the ideal MHD model is that numerical resistivity will behave similarly to the diffusive term $\eta' \nabla^2 \mathbf{B}$ and indeed, numerical experiments show that magnetic reconnection remains a robust feature of "ideal MHD" simulations. On the other hand, one would expect numerical diffusion to go to zero with increased grid resolution, which implies that reconnection should disappear from a well-resolved solution. In this appendix, we take a closer look and resolve this apparent contradiction.

The main argument is that an ideal MHD reconnecting current sheet behaves like a discontinuity and therefore the derivatives of the solution across the current sheet do not converge to a finite value. In particular, the current density, obtained from the derivative of the magnetic field, goes to infinity as the grid resolution is increased, while the numerical diffusion goes to zero. Their product, which determines the reconnection rate, remains finite. The global reconnection rate in the magnetosphere, in fact, is mostly set by the external conditions. On the dayside, the solar wind brings in magnetic flux at a rate of $|u_x|B_z$. A fraction of this flux will reconnect at the dayside magnetopause for $B_z < 0$. Since the magnetic flux attached to the Earth cannot grow without bound, there has to be a matching reconnection rate in the magnetotail, which completes the Dungey cycle. This means that the global time averaged reconnection rate is predominantly set by the external solar wind and IMF driver, and not by the details of the physics at the reconnection sites [Gonzalez et al., 2016].

We now look into more detail, how the numerical scheme actually achieves this. For finite volume methods solving the

$$\frac{\partial U}{\partial t} + \nabla \cdot F = 0 \tag{.3}$$

equation, the numerical flux is calculated at the cell interfaces, and it depends on the right and left states U^R and U^L extrapolated from the right and left directions, respectively, and

the characteristic wave speeds. The Lax-Friedrichs flux is the simplest example:

$$F^{LF} = \frac{F(U^R) + F(U^L)}{2} - \frac{1}{2}\lambda_{\max}(U^R - U^L) \tag{.4}$$

where F is the physical flux function. The first term contains the physical flux as the average of $F(U^R)$ and $F(U^L)$. The second term introduces numerical diffusion to preserve the monotonicity of the numerical solution. The numerical diffusion is proportional to the fastest wave speed $\lambda_{\max}$ corresponding to the fast magnetosonic wave in ideal MHD. The $U^R - U^L$ difference is some fraction of the difference between the cell center values on the two sides of the cell:

$$(U^R - U^L)_f = \alpha_f(U_{k+1} - U_k) \tag{.5}$$

Here f represents the index of the cell face between cells indexed by k and $k+1$. The fraction $0 \leq \alpha_f \leq 1$ depends on the numerical scheme. For a first order scheme $\alpha_f = 1$. For a higher order scheme, the fraction depends on the limiters used in the algorithm and the differences of U in neighboring cells.

For sake of simplicity, let us consider a current sheet parallel to the $X - Y$ plane and assume that B_x changes sign across the current sheet as we move in the Z direction. The physical flux function in the Z direction is $F = v_z B_x - v_x B_z$. The numerical flux function at the cell interface f is

$$F_f^{LF} = \frac{F(U_f^R) + F(U_f^L)}{2} - \frac{1}{2}\lambda_{\max,f}\alpha_f(B_{x,k+1} - B_{x,k}) \tag{.6}$$

The numerical diffusive part of the flux can be written as

$$F_f^{\text{diff}} = -\frac{\lambda_{\max,f}\alpha_f\Delta z}{2}\frac{B_{x,k+1} - B_{x,k}}{\Delta z} \tag{.7}$$

which is a numerical approximation of $\eta' \partial_z B_x$ with the numerical diffusivity

$$\eta' = \frac{\lambda_{\max,f} \alpha_f \Delta z}{2} \tag{.8}$$

For a smooth solution $\partial_z B_x$ converges to a finite value as the grid is refined, while η' converges to zero because $\Delta z \to 0$. For a discontinuous solution, however, the difference $B_{x,k+1} - B_{x,k}$ as well as $\lambda_{\max,f}$ and α_f all become independent of the grid resolution as $\Delta z \to 0$. This is a direct consequence of the fact that neither the ideal MHD equations, nor the numerical scheme has any intrinsic length scale other than the grid cell size. This means that the current sheet will be resolved with a fixed number of grid points following a fixed numerical profile (a series of the discrete values $B_{x,k}$ across the current sheet) independent of the grid resolution for small enough Δz. Therefore the numerical reconnection rate will converge to a finite value, determined predominantly by the external conditions (the external field $B_x^{\pm\text{ext}}$ and the converging velocity $u_z^{\pm\text{ext}}$ outside the current sheet), instead of zero. In physical terms, the numerical resistivity η' goes to 0, but the current density $(1/\mu_0)\Delta B_x/\Delta z$ goes to infinity and their product remains finite.

The maximum possible numerical reconnection rate is $\lambda_{\max,f}|B^{+\text{ext}} - B^{-\text{ext}}|/2$ corresponding to a current sheet where the magnetic field jumps from $B_x^L = B_{x,k} = B_x^{-\text{ext}}$ to $B_x^R = B_{x,k+1} = B_x^{+\text{ext}}$ across a single cell face, and $\lambda_{\max,f}$ is the maximum (or average) of the fast magnetosonic speeds taken at the two cell centers next to the face. The fraction α_f is 1 at this interface independent of the nominal order of the scheme, because all schemes drop to first order at this type of numerical discontinuity due to the limiters. This maximum numerical reconnection rate far exceeds the typical physical reconnection rate $\approx 0.1 v_A |B^{\text{ext}}|$, where v_A is the Alfvén speed, found in PIC simulations. The actual numerical profile realized by the numerical scheme will have multiple points across the current sheet resulting in a lower numerical diffusion rate than the theoretical maximum. In a 2 or 3 dimensional system, the global reconnection rate will depend on many factors, including the presence of

Hall physics, which has a major impact on the structure of the reconnection site [Birn et al., 2001a] and the achievable reconnection rate.

Figure .1 shows that these theoretical considerations are indeed valid in a complicated 3D magnetosphere simulation. We have performed two ideal MHD simulations with $\Delta x = 1/4\, R_E$ and $1/8\, R_E$ grid resolutions in the magnetotail, respectively. We compare the numerical solution across the current sheet at the same place and same time. As the figure shows, the number of grid cells, represented by the symbols, across the current sheet and the magnetic field values at the cell centers are essentially the same in the two simulations. The only change is the physical distance between the cells, which is reduced by a factor of 2 on the finer grid. As a result, the current density is twice higher, while the numerical dissipation rate is half of those obtained on the coarser grid. In the end, the reconnection rate is essentially the same in the two simulations, which results in essentially the same global solution.

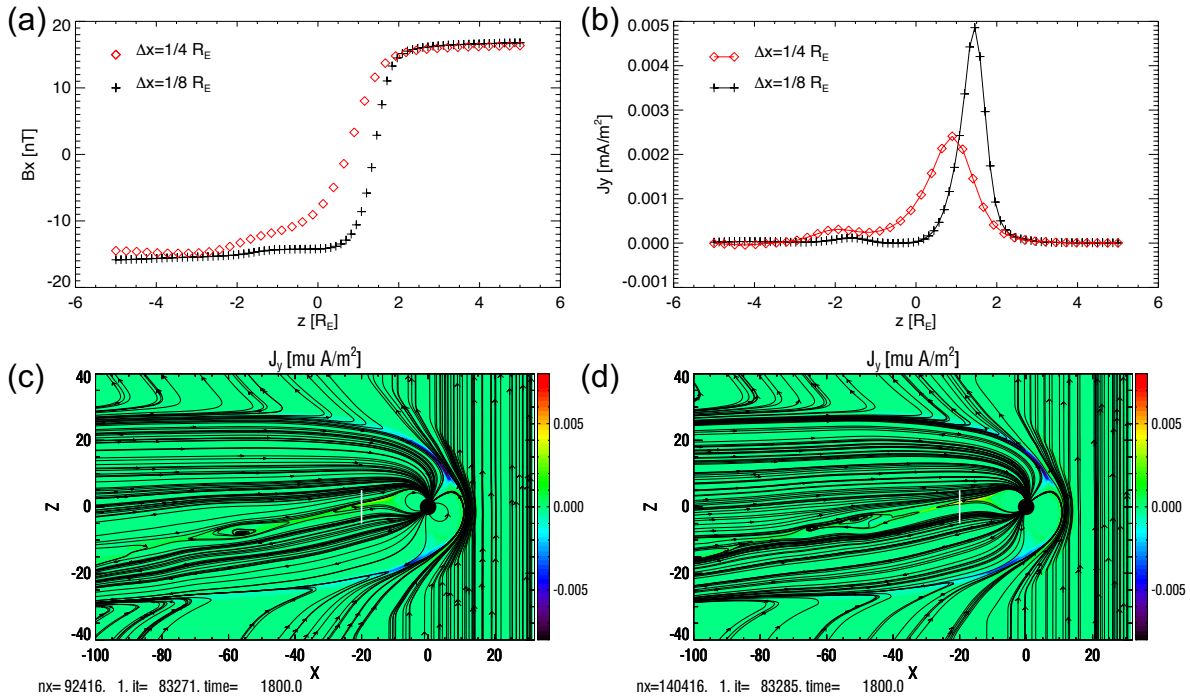

Figure .1: (a) The B_x profiles across the current sheet from two simulations with different grid resolutions in the magnetotail. The profiles are taken along the $x = -20\,R_E$ and $y = 0$ line from $z = -5\,R_E$ to $5\,R_E$. The symbols show the discrete values at the grid cell centers. (b) The J_y current profiles taken at the same position as B_x in panel (a). (c) The meridional cut of the simulation domain with J_y and magnetic field lines for $1/4\,R_E$ grid resolution in the magnetotail. (d) Same physical quantities as panel (c) but with $1/8\,R_E$ grid resolution in the magnetotail.

BIBLIOGRAPHY

Omar W. Ahmed, Rami Qahwaji, Tufan Colak, Paul A. Higgins, Peter T. Gallagher, and D. Shaun Bloomfield. Solar Flare Prediction Using Advanced Feature Extraction, Machine Learning, and Feature Selection. , 283(1):157–175, Mar 2013. doi: 10.1007/s11207-011-9896-1.

S-I Akasofu. The development of the auroral substorm. *Planetary and Space Science*, 12(4): 273–282, 1964.

V. Angelopoulos, C. F. Kennel, F. V. Coroniti, R. Pellat, M. G. Kivelson, R. J. Walker, C. T. Russell, W. Baumjohann, W. C. Feldman, and J. T. Gosling. Statistical characteristics of bursty bulk flow events. *J. Geophys. Res.*, 99:21,257, 1994.

Vassilis Angelopoulos, James P McFadden, Davin Larson, Charles W Carlson, Stephen B Mende, Harald Frey, Tai Phan, David G Sibeck, Karl-Heinz Glassmeier, Uli Auster, et al. Tail reconnection triggering substorm onset. *Science*, 321(5891):931–935, 2008.

Y Asano, R Nakamura, I Shinohara, M Fujimoto, T Takada, W Baumjohann, CJ Owen, AN Fazakerley, A Runov, T Nagai, et al. Electron flat-top distributions around the magnetic reconnection region. *Journal of Geophysical Research: Space Physics*, 113(A1), 2008.

Nicolas Aunai, Michael Hesse, and Maria Kuznetsova. Electron nongyrotropy in the context of collisionless magnetic reconnection. *Physics of Plasmas*, 20(9):092903, 2013.

Daniel N Baker, TI Pulkkinen, V Angelopoulos, W Baumjohann, and RL McPherron. Neutral line model of substorms: Past results and present view. *Journal of Geophysical Research: Space Physics*, 101(A6):12975–13010, 1996.

DN Baker. What is space weather? *Advances in Space Research*, 22(1):7–16, 1998.

Aisling Bergin, Sandra C Chapman, and Jesper W Gjerloev. Ae, dst, and their supermag counterparts: The effect of improved spatial resolution in geomagnetic indices. *Journal of Geophysical Research: Space Physics*, 125(5):e2020JA027828, 2020.

Ludwig Biermann. Kometenschweife und solare korpuskularstrahlung. *Zeitschrift fur Astrophysik*, 29:274, 1951.

J. Birn, J. F. Drake, M. A. Shay, B. N. Rogers, R. E. Denton, M. Hesse, M. Kuznetsova, Z. W. Ma, A. Bhattacharjee, A. Otto, and P. L. Pritchett. Geospace Environmental

Modeling (GEM) magnetic reconnection challenge. *J. Geophys. Res.*, 106(A3):3715–3720, 2001a. doi: 10.1029/1999JA900449.

J Birn, JF Drake, MA Shay, BN Rogers, RE Denton, M Hesse, M Kuznetsova, ZW Ma, A Bhattacharjee, A Otto, et al. Geospace environmental modeling (gem) magnetic reconnection challenge. *Journal of Geophysical Research: Space Physics*, 106(A3):3715–3719, 2001b.

J Birn, M Hesse, and K Schindler. Entropy conservation in simulations of magnetic reconnection. *Physics of plasmas*, 13(9):092117, 2006.

Joachim Birn, M Hesse, K Schindler, and S Zaharia. Role of entropy in magnetotail dynamics. *Journal of Geophysical Research: Space Physics*, 114(A9), 2009.

M. G. Bobra and S. Couvidat. Solar Flare Prediction Using SDO/HMI Vector Magnetic Field Data with a Machine-learning Algorithm. , 798(2):135, Jan 2015. doi: 10.1088/0004-637X/798/2/135.

M. G. Bobra, X. Sun, J. T. Hoeksema, M. Turmon, Y. Liu, K. Hayashi, G. Barnes, and K. D. Leka. The Helioseismic and Magnetic Imager (HMI) Vector Magnetic Field Pipeline: SHARPs - Space-Weather HMI Active Region Patches. , 289(9):3549–3578, Sep 2014. doi: 10.1007/s11207-014-0529-3.

J.E. Borovsky, R. J. Nemzek, and R. D. Belian. The occurrence rate of magnetopheric-substorm onsets: Random and periodic substorms. *J. Geophys. Res.*, 98:3807–3813, 1993a.

Joseph E Borovsky, Robert J Nemzek, and Richard D Belian. The occurrence rate of magnetospheric-substorm onsets: Random and periodic substorms. *Journal of Geophysical Research: Space Physics*, 98(A3):3807–3813, 1993b.

Léon Bottou, Frank E Curtis, and Jorge Nocedal. Optimization methods for large-scale machine learning. *Siam Review*, 60(2):223–311, 2018.

Laura E. Boucheron, Amani Al-Ghraibah, and R. T. James McAteer. Prediction of Solar Flare Size and Time-to-Flare Using Support Vector Machine Regression. , 812(1):51, Oct 2015. doi: 10.1088/0004-637X/812/1/51.

OJ Brambles, W Lotko, B Zhang, M Wiltberger, J Lyon, and RJ Strangeway. Magnetosphere sawtooth oscillations induced by ionospheric outflow. *Science*, 332(6034):1183–1186, 2011.

OJ Brambles, W Lotko, B Zhang, J Ouellette, J Lyon, and M Wiltberger. The effects of ionospheric outflow on icme and sir driven sawtooth events. *Journal of Geophysical Research: Space Physics*, 118(10):6026–6041, 2013.

S.H. Brecht, J. Lyon, J.A. Fedder, and K. Hain. A simulation study of east-west IMF effects on the magnetosphere. *Geophys. Res. Lett.*, 8:397–400, 1981.

S.H. Brecht, J. Lyon, J.A. Fedder, and K. Hain. A time-dependent three-dimensional simulation of the earth's magnetosphere: Reconnection events. *J. Geophys. Res.*, 87:6098–6108, 1982.

J. L. Burch, R. B. Torbert, T. D. Phan, L.-J. Chen, T. E. Moore, R. E. Ergun, J. P. Eastwood, D. J. Gershman, P. A. Cassak, M. R. Argall, S. Wang, M. Hesse, C. J. Pollock, B. L. Giles, R. Nakamura, B. H. Mauk, S. A. Fuselier, C. T. Russell, R. J. Strangeway, J. F. Drake, M. A. Shay, Yu. V. Khotyaintsev, P.-A. Lindqvist, G. Marklund, F. D. Wilder, D. T. Young, K. Torkar, J. Goldstein, J. C. Dorelli, L. A. Avanov, M. Oka, D. N. Baker, A. N. Jaynes, K. A. Goodrich, I. J. Cohen, D. L. Turner, J. F. Fennell, J. B. Blake, J. Clemmons, M. Goldman, D. Newman, S. M. Petrinec, K. J. Trattner, B. Lavraud, P. H. Reiff, W. Baumjohann, W. Magnes, M. Steller, W. Lewis, Y. Saito, V. Coffey, and M. Chandler. Electron-scale measurements of magnetic reconnection in space. *Science*, 352:6290, 2016a. doi: 10.1126/science.aaf2939.

JL Burch and TD Phan. Magnetic reconnection at the dayside magnetopause: Advances with mms. *Geophysical Research Letters*, 43(16):8327–8338, 2016.

JL Burch, RB Torbert, TD Phan, L-J Chen, TE Moore, RE Ergun, JP Eastwood, DJ Gershman, PA Cassak, MR Argall, et al. Electron-scale measurements of magnetic reconnection in space. *Science*, 352(6290):aaf2939, 2016b.

X. Cai, C.R. Clauer, and A.J. Ridley. Statistical analysis of ionospheric potential patterns for isolated substorms and sawtooth events. *Ann. Geophys.*, 24:1977, 2006.

H. Carmichael. A Process for Flares. *NASA Special Publication*, 50:451, 1964.

Li-Jen Chen, Michael Hesse, Shan Wang, Daniel Gershman, Robert Ergun, Craig Pollock, Roy Torbert, Naoki Bessho, William Daughton, John Dorelli, et al. Electron energization and mixing observed by mms in the vicinity of an electron diffusion region during magnetopause reconnection. *Geophysical Research Letters*, 43(12):6036–6043, 2016a.

Y. Chen and G. Tóth. Gauss's law satisfying energy-conserving semi-implicit particle-in-cell method. *J. Comput. Phys.*, 386:632, 2019. doi: 10.1016/j.jcp.2019.02.032.

Y. Chen, G. Tóth, and T. I. Gombosi. A fifth-order finite difference scheme for hyperbolic equations on block-adaptive curvilinear grids. *J. Comput. Phys.*, 305:604, 2016b. doi: 10.1016/j.jcp.2015.11.003.

Y. Chen, G. Tóth, P. Cassak, X. Jia, T. I. Gombosi, J. Slavin, S. Markidis, and B. Peng. Global three-dimensional simulation of earth's dayside reconnection using a two-way coupled magnetohydrodynamics with embedded particle-in-cell model: initial results. *J. Geophys. Res.*, 122:10318, 2017. doi: 10.1002/2017JA024186.

Yang Chen, Ward B. Manchester, Alfred O. Hero, Gabor Toth, Benoit DuFumier, Tian Zhou, Xiantong Wang, Haonan Zhu, Zeyu Sun, and Tamas I. Gombosi. Identifying solar flare precursors using time series of sdo/hmi images and sharp parameters. *Space Weather*, 17(10):1404–1426, 2019a. doi: 10.1029/2019SW002214. URL https://agupubs.onlinelibrary.wiley.com/doi/abs/10.1029/2019SW002214.

Yuxi Chen, Gábor Tóth, Xianzhe Jia, James A. Slavin, Weijie Sun, Stefano Markidis, Tamas I. Gombosi, and Jim M. Raines. Studying dawn-dusk asymmetries of mercury's

magnetotail using mhd-epic simulations. *Journal of Geophysical Research: Space Physics*, 124(11):8954–8973, 2019b.

Yuxi Chen, Gábor Tóth, Heli Hietala, Sarah K Vines, Ying Zou, Yukitoshi Nishimura, Marcos VD Silveira, Zhifang Guo, Yu Lin, and Stefano Markidis. Magnetohydrodynamic with embedded particle-in-cell simulation of the geospace environment modeling dayside kinetic processes challenge event. *Earth and Space Science*, 7(11):e2020EA001331, 2020.

Yuxi Chen, Gabor Toth, Hongyang Zhou, and Xiantong Wang. Fleks: A flexible particle-in-cell code for multi-scale plasma simulations. *Earth and Space Science Open Archive*, 2021. doi: doi.org/10.1002/essoar.10508070.1.

A Compagnino, P Romano, and F Zuccarello. A statistical study of cme properties and of the correlation between flares and cmes over solar cycles 23 and 24. *Solar Physics*, 292(1): 1–19, 2017.

L. K. S. Daldorff, G. Tóth, T. I. Gombosi, G. Lapenta, J. Amaya, S. Markidis, and J. U. Brackbill. Two-way coupling of a global Hall magnetohydrodynamics model with a local implicit Particle-in-Cell model. *J. Comput. Phys.*, 268:236, 2014. doi: 10.1016/j.jcp.2014.03.009.

William Daughton, Jack Scudder, and Homa Karimabadi. Fully kinetic simulations of undriven magnetic reconnection with open boundary conditions. *Physics of Plasmas*, 13(7): 072101, 2006.

T Neil Davis and Masahisa Sugiura. Auroral electrojet activity index ae and its universal time variations. *Journal of Geophysical Research*, 71(3):785–801, 1966.

Darren L De Zeeuw, Tamas I Gombosi, Clinto PT Groth, Kenneth G Powell, and Quentin F Stout. An adaptive mhd method for global space weather simulations. *IEEE Transactions on Plasma Science*, 28(6):1956–1965, 2000.

D.L. De Zeeuw, S. Sazykin, R.A. Wolf, T.I. Gombosi, A.J. Ridley, and G. Tóth. Coupling of a global MHD code and an inner magnetosphere model: Initial results. *J. Geophys. Res.*, 109(A12):219, 2004. doi: 10.1029/2003JA010366.

A. Dedner, F. Kemm, D. Kröner, C.-D. Munz, T. Schnitzer, and M. Wesenberg. Hyperbolic divergence cleaning for the MHD equations. *J. Comput. Phys.*, 175:645–673, 2003.

Charles A Doswell III, Robert Davies-Jones, and David L Keller. On summary measures of skill in rare event forecasting based on contingency tables. *Weather and Forecasting*, 5(4): 576–585, 1990.

J.W. Dungey. Interplanetary magnetic field and the auroral zones. *Phys. Rev. Lett.*, 93:47, 1961. doi: 10.1103/PhysRevLett.6.47.

JP Eastwood, H Hietala, G Toth, TD Phan, and M Fujimoto. What controls the structure and dynamics of earth's magnetosphere? *Space Science Reviews*, 188(1):251–286, 2015.

J Egedal, A Lê, N Katz, L-J Chen, B Lefebvre, W Daughton, and A Fazakerley. Cluster observations of bidirectional beams caused by electron trapping during antiparallel reconnection. *Journal of Geophysical Research: Space Physics*, 115(A3), 2010.

Kostas Florios, Ioannis Kontogiannis, Sung-Hong Park, Jordan A. Guerra, Federico Benvenuto, D. Shaun Bloomfield, and Manolis K. Georgoulis. Forecasting Solar Flares Using Magnetogram-based Predictors and Machine Learning. , 293(2):28, Feb 2018. doi: 10.1007/s11207-018-1250-4.

TG Forbes. A review on the genesis of coronal mass ejections. *Journal of Geophysical Research: Space Physics*, 105(A10):23153–23165, 2000.

TG Forbes and LW Acton. Reconnection and field line shrinkage in solar flares. *The Astrophysical Journal*, 459:330, 1996.

James Franklin. The elements of statistical learning: data mining, inference and prediction. *The Mathematical Intelligencer*, 27(2):83–85, mar 2005. doi: 10.1007/bf02985802. URL https://doi.org/10.1007%2Fbf02985802.

Natalia Ganushkina, Allison Jaynes, and Michael Liemohn. Space weather effects produced by the ring current particles. *Space Science Reviews*, 212(3):1315–1344, 2017.

Ye Gao. Comparing the cross polar cap potentials measured by superdarn and amie during saturation intervals. *Journal of Geophysical Research: Space Physics*, 117(A8), 2012.

Howard A. Garcia. Temperature and Emission Measure from Goes Soft X-Ray Measurements. , 154(2):275–308, Oct 1994. doi: 10.1007/BF00681100.

Felix A. Gers, Jürgen Schmidhuber, and Fred Cummins. Learning to forget: Continual prediction with LSTM. *Neural Computation*, 12(10):2451–2471, oct 2000. doi: 10.1162/089976600300015015. URL https://doi.org/10.1162%2F089976600300015015.

A. Glocer, G. Tóth, Y. J. Ma, T. Gombosi, J.-C. Zhang, and L. M. Kistler. Multifluid Block-Adaptive-Tree Solar wind Roe-type Upwind Scheme: Magnetospheric composition and dynamics during geomagnetic storms – initial results. *J. Geophys. Res.*, 114:A12203, 2009. doi: 10.1029/2009JA014418.

A. Glocer, J. Dorelli, G. Tóth, C. M. Komar, and P. A. Cassak. Separator reconnection at the magnetopause for predominantly northward and southward IMF: techniques and results. *J. Geophys. Res.*, 120:5377, 2016. doi: 10.1002/2015JA021417.

Tamas I Gombosi. *Physics of the space environment*. Cambridge University Press, 1998.

W. D. Gonzalez, E. N. Parker, F. S. Mozer, V. M. Vasyliūnas, P. L. Pritchett, H. Karimabadi, P. A. Cassak, J. D. Scudder, M. Yamada, R. M. Kulsrud, and D. Koga. *Fundamental Concepts Associated with Magnetic Reconnection*, pages 1–32. Springer International Publishing, Cham, 2016. ISBN 978-3-319-26432-5. doi: 10.1007/978-3-319-26432-5_1. URL https://doi.org/10.1007/978-3-319-26432-5_1.

Walter D Gonzalez, Bruce T Tsurutani, and Alicia L Clúa de Gonzalez. Interplanetary origin of geomagnetic storms. *Space Science Reviews*, 88(3):529–562, 1999.

WD Gonzalez, Jo-Ann Joselyn, Yohsuke Kamide, Herb W Kroehl, G Rostoker, BT Tsurutani, and VM Vasyliunas. What is a geomagnetic storm? *Journal of Geophysical Research: Space Physics*, 99(A4):5771–5792, 1994.

JT Gosling, DJ McComas, JL Phillips, and SJ Bame. Geomagnetic activity associated with earth passage of interplanetary shock disturbances and coronal mass ejections. *Journal of Geophysical Research: Space Physics*, 96(A5):7831–7839, 1991.

Alex Graves, Abdel rahman Mohamed, and Geoffrey Hinton. Speech recognition with deep recurrent neural networks. In *2013 IEEE International Conference on Acoustics, Speech and Signal Processing*. IEEE, may 2013. doi: 10.1109/icassp.2013.6638947. URL https://doi.org/10.1109%2Ficassp.2013.6638947.

Lucie M. Green, Tibor Török, Bojan Vršnak, Ward Manchester, and Astrid Veronig. The Origin, Early Evolution and Predictability of Solar Eruptions. , 214(1):46, Feb 2018. doi: 10.1007/s11214-017-0462-5.

John D Haiducek, Daniel T Welling, Natalia Y Ganushkina, Steven K Morley, and Dogacan Su Ozturk. Swmf global magnetosphere simulations of january 2005: Geomagnetic indices and cross-polar cap potential. *Space Weather*, 15(12):1567–1587, 2017.

M. R. Hairston, D. R. Weimer, R. A Heelis, and F. Rich. Analysis of the ionospheric cross polar cap potential drop and electrostatic potential distribution patterns during the January 1997 CME event using DMSP data. *JATP*, 61:195–206, 1998.

MG Henderson, GD Reeves, R Skoug, MF Thomsen, Michael H Denton, SB Mende, TJ Immel, PC Brandt, and HJ Singer. Magnetospheric and auroral activity during the 18 april 2002 sawtooth event. *Journal of Geophysical Research: Space Physics*, 111(A1), 2006.

M Hesse and PA Cassak. Magnetic reconnection in the space sciences: Past, present, and future. *Journal of Geophysical Research: Space Physics*, 125(2):e2018JA025935, 2020.

T Hirayama. Theoretical model of flares and prominences. *Solar Physics*, 34(2):323–338, 1974.

Sepp Hochreiter and Jürgen Schmidhuber. Long short-term memory. *Neural computation*, 9(8):1735–1780, 1997.

J. T. Hoeksema, C. S. Baldner, R. I. Bush, J. Schou, and P. H. Scherrer. On-Orbit Performance of the Helioseismic and Magnetic Imager Instrument onboard the Solar Dynamics Observatory. , 293(3):45, Mar 2018. doi: 10.1007/s11207-018-1259-8.

EW Hones Jr. Comment on'on hot tenuous plasmas, fireballs, and boundary layers in the earth's magnetotail'by la frank, kl ackerson, and rp lepping. *J. Geophys. Res.;(United States)*, 83(A3), 1978.

EW Hones Jr, J Birn, DN Baker, SJ Bame, WC Feldman, DJ McComas, RD Zwickl, JA Slavin, EJ Smith, and BT Tsurutani. Detailed examination of a plasmoid in the distant magnetotail with isee 3. *Geophysical research letters*, 11(10):1046–1049, 1984.

Chao-Song Huang, GD Reeves, JE Borovsky, RM Skoug, ZY Pu, and G Le. Periodic magnetospheric substorms and their relationship with solar wind variations. *Journal of Geophysical Research: Space Physics*, 108(A6), 2003.

Xin Huang, Huaning Wang, Long Xu, Jinfu Liu, Rong Li, and Xinghua Dai. Deep Learning Based Solar Flare Forecasting Model. I. Results for Line-of-sight Magnetograms. , 856(1): 7, Mar 2018. doi: 10.3847/1538-4357/aaae00.

Zhenguang Huang, Gábor Tóth, Bart van der Holst, Yuxi Chen, and Tamas Gombosi. A six-moment multi-fluid plasma model. *Journal of Computational Physics*, 387:134–153, 2019.

K-J Hwang, E Choi, K Dokgo, JL Burch, DG Sibeck, BL Giles, ML Goldstein, WR Paterson, CJ Pollock, QQ Shi, et al. Electron vorticity indicative of the electron diffusion region of magnetic reconnection. *Geophysical research letters*, 46(12):6287–6296, 2019.

P. Janhunen. GUMICS-3: A global ionosphere-magnetosphere coupling simulation with high ionospheric resolution. In *Proceedings of the ESA 1996 Symposium on Environment Modelling for Space-Based Applications*, pages 233–239. ESA SP-392, 1996.

Zhenbang Jiao, Hu Sun, Xiantong Wang, Ward Manchester, Alfred Hero, Yang Che, et al. Solar flare intensity prediction with machine learning models. *arXiv preprint arXiv:1912.06120*, 2019.

Eric Jonas, Monica Bobra, Vaishaal Shankar, J. Todd Hoeksema, and Benjamin Recht. Flare Prediction Using Photospheric and Coronal Image Data. , 293(3):48, Mar 2018. doi: 10.1007/s11207-018-1258-9.

John G Kappenman. An introduction to power grid impacts and vulnerabilities from space weather. *Space Storms and Space Weather Hazards*, pages 335–361, 2001.

Shachar Kaufman, Saharon Rosset, Claudia Perlich, and Ori Stitelman. Leakage in data mining: Formulation, detection, and avoidance. *ACM Transactions on Knowledge Discovery from Data (TKDD)*, 6(4):15, 2012.

Diederik P Kingma and Jimmy Ba. Adam: A method for stochastic optimization. *arXiv preprint arXiv:1412.6980*, 2014.

R. A. Kopp and G. W. Pneuman. Magnetic reconnection in the corona and the loop prominence phenomenon. , 50:85–98, October 1976. doi: 10.1007/BF00206193.

B. Koren. A robust upwind discretisation method for advection, diffusion and source terms. In C.B. Vreugdenhil and B.Koren, editors, *Numerical Methods for Advection-Diffusion Problems*, page 117. Vieweg, Braunschweig, 1993.

Louis J Lanzerotti. Space weather effects on technologies. *Washington DC American Geophysical Union Geophysical Monograph Series*, 125:11–22, 2001.

G. Lapenta. Particle simulations of space weather. *J. Comput. Phys.*, 231:795–821, 2012.

G. Lapenta. Exactly energy conserving semi-implicit particle in cell formulation. *J. Comput. Phys.*, 334:349, 2017. doi: 10.1016/j.jcp.2017.01.002.

J. N. LeBoeuf, T. Tajima, C. F. Kennel, and J. M. Dawson. Global simulations of the three-dimensional magnetosphere. *Geophys. Res. Lett.*, 8:257–260, 1981.

Mu Li, Tong Zhang, Yuqiang Chen, and Alexander J. Smola. Efficient mini-batch training for stochastic optimization. In *Proceedings of the 20th ACM SIGKDD international conference on Knowledge discovery and data mining - KDD '14*. ACM Press, 2014. doi: 10.1145/2623330.2623612. URL https://doi.org/10.1145%2F2623330.2623612.

Xiaocan Li, Fan Guo, and Hui Li. Particle acceleration in kinetic simulations of nonrelativistic magnetic reconnection with different ion–electron mass ratios. *The Astrophysical Journal*, 879(1):5, 2019.

Hao Liu, Chang Liu, Jason T. L. Wang, and Haimin Wang. Predicting Solar Flares Using a Long Short-term Memory Network. , 877(2):121, Jun 2019. doi: 10.3847/1538-4357/ab1b3c.

A Lotekar, IY Vasko, FS Mozer, I Hutchinson, AV Artemyev, SD Bale, John W Bonnell, Robert Ergun, B Giles, Yu V Khotyaintsev, et al. Multisatellite mms analysis of electron holes in the earth's magnetotail: Origin, properties, velocity gap, and transverse instability. *Journal of Geophysical Research: Space Physics*, 125(9):e2020JA028066, 2020.

Edward T Lu and Russell J Hamilton. Avalanches and the distribution of solar flares. *The astrophysical journal*, 380:L89–L92, 1991.

Eric J Lund, Niloufar Nowrouzi, Lynn M Kistler, Xia Cai, and Harald U Frey. On the role of ionospheric ions in sawtooth events. *Journal of Geophysical Research: Space Physics*, 123(1):665–684, 2018.

J. G. Lyon, J.A. Fedder, and J.G. Huba. The effect of different resistivity models on magnetotail dynamics. *J. Geophys. Res.*, 91:8057–8064, 1986.

J.G. Lyon, J.A. Fedder, and C.M. Mobarry. The Lyon-Fedder-Mobarry (LFM) global MHD magnetospheric simulation code. *J. Atmos. Sol-Terr. Phys.*, 66:1333, 2004.

Xuanye Ma and Antonius Otto. Nonadiabatic heating in magnetic reconnection. *Journal of Geophysical Research: Space Physics*, 119(7):5575–5588, 2014.

Yingjuan Ma, Christopher T Russell, Gabor Toth, Yuxi Chen, Andrew F Nagy, Yuki Harada, James McFadden, Jasper S Halekas, Rob Lillis, John EP Connerney, et al. Reconnection in the martian magnetotail: Hall-mhd with embedded particle-in-cell simulations. *Journal of Geophysical Research: Space Physics*, 123(5):3742–3763, 2018.

ZW Ma and A Bhattacharjee. Hall magnetohydrodynamic reconnection: The geospace environment modeling challenge. *Journal of Geophysical Research: Space Physics*, 106 (A3):3773–3782, 2001.

W. Manchester. Buoyant disruption of magnetic arcades with self-induced shearing. *Journal of Geophysical Research (Space Physics)*, 108:1162, April 2003. doi: 10.1029/2002JA009252.

S. Markidis, G. Lapenta, and Rizwan-Uddin. Multi-scale simulations of plasma with ipic3d. *Mathematics and Computers in Simulation*, 80:1509–1519, 2010. doi: 10.1016/j.matcom.2009.08.038.

Stefano Markidis, Pierre Henri, Giovanni Lapenta, Andrey Divin, Martin Goldman, David Newman, and Erwin Laure. Kinetic simulations of plasmoid chain dynamics. *Physics of Plasmas*, 20(8):082105, 2013.

S Masuda, T Kosugi, H Hara, S Tsuneta, and Y Ogawara. A loop-top hard x-ray source in a compact solar flare as evidence for magnetic reconnection. *Nature*, 371(6497):495–497, 1994.

Y. J. Moon, G. S. Choe, Y. D. Park, Haimin Wang, Peter T. Gallagher, Jongchul Chae, H. S. Yun, and Philip R. Goode. Statistical Evidence for Sympathetic Flares. , 574(1): 434–439, July 2002. doi: 10.1086/340945.

Takayuki Muranushi, Takuya Shibayama, Yuko Hada Muranushi, Hiroaki Isobe, Shigeru Nemoto, Kenji Komazaki, and Kazunari Shibata. UFCORIN: A fully automated predictor of solar flares in GOES X-ray flux. *Space Weather*, 13(11):778–796, Nov 2015. doi: 10.1002/2015SW001257.

Nick Murphy, Carl Sovinec, and Paul Cassak. Simulation and analysis of magnetic reconnection in an experimental geometry. In *Bulletin of the American Astronomical Society*, volume 41, page 514, 2009a.

Nick Murphy, Carl Sovinec, and Paul Cassak. Simulation and analysis of magnetic reconnection in an experimental geometry. In *Bulletin of the American Astronomical Society*, volume 41, page 514, 2009b.

T Nagai, M Fujimoto, Y Saito, S Machida, T Terasawa, R Nakamura, T Yamamoto, T Mukai, A Nishida, and S Kokubun. Structure and dynamics of magnetic reconnection for substorm onsets with geotail observations. *Journal of Geophysical Research: Space Physics*, 103(A3): 4419–4440, 1998.

T Nagai, I Shinohara, M Fujimoto, M Hoshino, Y Saito, S Machida, and T Mukai. Geotail observations of the hall current system: Evidence of magnetic reconnection in the magnetotail. *Journal of Geophysical Research: Space Physics*, 106(A11):25929–25949, 2001.

PT Newell and JW Gjerloev. Evaluation of supermag auroral electrojet indices as indicators of substorms and auroral power. *Journal of Geophysical Research: Space Physics*, 116 (A12), 2011.

N. Nishizuka, K. Sugiura, Y. Kubo, M. Den, and M. Ishii. Deep Flare Net (DeFN) Model for Solar Flare Prediction. , 858(2):113, May 2018. doi: 10.3847/1538-4357/aab9a7.

JE Ouellette, OJ Brambles, JG Lyon, W Lotko, and BN Rogers. Properties of outflow-driven sawtooth substorms. *Journal of Geophysical Research: Space Physics*, 118(6):3223–3232, 2013.

E. N. Parker. Dynamics of the interplanetary gas and magnetic fields. *Astrophys. J.*, 128 (3):664–676, November 1958.

Eugene N Parker. Sweet's mechanism for merging magnetic fields in conducting fluids. *Journal of Geophysical Research*, 62(4):509–520, 1957.

Adam Paszke, Sam Gross, Soumith Chintala, Gregory Chanan, Edward Yang, Zachary DeVito, Zeming Lin, Alban Desmaison, Luca Antiga, and Adam Lerer. Automatic differentiation in pytorch. 2017.

Barak A Pearlmutter. Learning state space trajectories in recurrent neural networks. *Neural Computation*, 1(2):263–269, 1989.

Harry E Petschek. 50 magnetic field annihilation. In *AAS-NASA Symposium on the Physics of Solar Flares: Proceedings of a Symposium Held at the Goddard Space Flight Center, Greenbelt, Maryland, October 28-30, 1963*, volume 50, page 425. Scientific and Technical Information Division, National Aeronautics and ..., 1964.

Kenneth G Powell, Philip L Roe, Timur J Linde, Tamas I Gombosi, and Darren L De Zeeuw. A solution-adaptive upwind scheme for ideal magnetohydrodynamics. *Journal of Computational Physics*, 154(2):284–309, 1999a.

K.G. Powell, P.L. Roe, T.J. Linde, T.I. Gombosi, and D. L. De Zeeuw. A solution-adaptive upwind scheme for ideal magnetohydrodynamics. *J. Comput. Phys.*, 154:284–309, 1999b. doi: 10.1006/jcph.1999.6299.

PL Pritchett. Relativistic electron production during driven magnetic reconnection. *Geophysical research letters*, 33(13), 2006.

A. Pulkkinen, L. Rastatter, M. Kuznetova, H. Singer, C. Balch, D. Weimer, G. Toth, A. Ridley, T. Gombosi, M. Wiltberger, J. Raeder, and R. Weigel. Community-wide validation of geospace model ground magnetic field perturbation predictions to support model transition to operations. *Space Weather*, 11:369–385, 2013. doi: 10.1002/swe.20056.

TI Pulkkinen, N Yu Ganushkina, EI Tanskanen, M Kubyshkina, GD Reeves, MF Thomsen, CT Russell, HJ Singer, JA Slavin, and J Gjerloev. Magnetospheric current systems during stormtime sawtooth events. *Journal of Geophysical Research: Space Physics*, 111(A11), 2006.

R. Qahwaji and T. Colak. Automatic Short-Term Solar Flare Prediction Using Machine Learning and Sunspot Associations. , 241(1):195–211, Mar 2007. doi: 10.1007/s11207-006-0272-5.

J. Raeder, R. J. Walker, and M. Ashour-Abdalla. The structure of the distant geomagnetic tail during long periods of northward IMF. *Geophys. Res. Lett.*, 22:349–352, 1995.

J. Raeder, J. Berchem, and M. Ashour-Abdalla. The importance of small scale processes in global MHD simulations: Some numerical experiments. In T. Chang and J. R. Jasperse, editors, *The Physics of Space Plasmas*, volume 14, page 403, Cambridge, Mass., 1996. MIT Cent. for Theoret. Geo/Cosmo Plasma Phys.

J. Raeder, R.L. McPherron, L.A. Frank, S. Kokubun, G. Lu, T. Mukai, W.R. Paterson, J.B. Sigwarth, H.J. Singer, and J.A. Slavin. Global simulation of the Geospace Environment Modeling substorm challenge event. *J. Geophys. Res.*, 106:281, 2001.

IG Richardson, EW Cliver, and HV Cane. Sources of geomagnetic storms for solar minimum and maximum conditions during 1972–2000. *Geophysical Research Letters*, 28(13):2569–2572, 2001.

A.D. Richmond and Y. Kamide. Mapping electrodynamic features of the high-latitude ionosphere from localized observations: Technique. *J. Geophys. Res.*, 93:5741–5759, 1988.

A. Ridley, T. Gombosi, and D. Dezeeuw. Ionospheric control of the magnetosphere: conductance. *Annales Geophysicae*, 22:567–584, February 2004. doi: 10.5194/angeo-22-567-2004.

A. J Ridley and E. A Kihn. Polar cap index comparisons with AMIE cross polar cap potential, electric field, and polar cap area. *Geophysical Research Letters*, 31:07801, Apr 2004. doi: 10.1029/2003GL019113.

RM Robinson and RA Behnke. Space weather, 2001.

G Rostoker, S-I Akasofu, JC Foster, RA Greenwald, Y Kamide, K Kawasaki, ATY Lui, RL McPherron, and CT Russell. Magnetospheric substorms—definition and signatures. *Journal of Geophysical Research: Space Physics*, 85(A4):1663–1668, 1980.

J.M. Ruohoniemi and R.A. Greenwald. The response of high latitude convection to a sudden southward IMF turning. *Geophys. Res. Lett.*, 25:2913, 1998.

CT Russell. The dynamics of planetary magnetospheres. *Planetary and Space Science*, 49 (10-11):1005–1030, 2001.

K Schindler. A theory of the substorm mechanism. *Journal of Geophysical Research*, 79(19): 2803–2810, 1974.

Rachel Schutt and Cathy O'Neil. *Doing data science: Straight talk from the frontline.* O'Reilly Media, Inc., 2013.

Yinsi Shou, Valeriy Tenishev, Yuxi Chen, Gabor Toth, and Natalia Ganushkina. Magnetohydrodynamic with adaptively embedded particle-in-cell model: Mhd-aepic. *Journal of Computational Physics*, page 110656, 2021.

JA Slavin, DN Baker, JD Craven, RC Elphic, DH Fairfield, LA Frank, AB Galvin, WJ Hughes, RH Manka, DG Mitchell, et al. Cdaw 8 observations of plasmoid signatures in the geomagnetic tail: An assessment. *Journal of Geophysical Research: Space Physics*, 94(A11):15153–15175, 1989.

JA Slavin, M Hesse, CJ Owen, S Taguchi, DH Fairfield, RP Lepping, S Kokubun, T Mukai, ATY Lui, RR Anderson, et al. Dual spacecraft observations of lobe magnetic field perturbations before, during and after plasmoid release. *Geophysical research letters*, 26(19): 2897–2900, 1999.

JA Slavin, DH Fairfield, RP Lepping, M Hesse, A Ieda, E Tanskanen, N Østgaard, T Mukai, T Nagai, HJ Singer, et al. Simultaneous observations of earthward flow bursts and plasmoid ejection during magnetospheric substorms. *Journal of Geophysical Research: Space Physics*, 107(A7):SMP–13, 2002.

JA Slavin, RP Lepping, J Gjerloev, DH Fairfield, M Hesse, CJ Owen, MB Moldwin, T Nagai, A Ieda, and T Mukai. Geotail observations of magnetic flux ropes in the plasma sheet. *Journal of Geophysical Research: Space Physics*, 108(A1):SMP–10, 2003.

Conway W Snyder and Marcia Neugebauer. Interplanetary solar-wind measurements by mariner ii. In *Proceedings of the Plasma Space Science Symposium*, pages 67–90. Springer, 1965.

I. V. Sokolov, E. V. Timofeev, J. I. Sakai, and K. Takayama. On shock capturing schemes using artificial wind. *Shock Waves*, 9:423–426, 1999.

Hui Song, Changyi Tan, Ju Jing, Haimin Wang, Vasyl Yurchyshyn, and Valentyna Abramenko. Statistical Assessment of Photospheric Magnetic Features in Imminent Solar Flare Predictions. , 254(1):101–125, Jan 2009. doi: 10.1007/s11207-008-9288-3.

P. Song, T. I. Gombosi, and A. J. Ridley. Three-fluid Ohm's law. *J. Geophys. Res.*, 106: 8149–8156, 2001.

Quentin F Stout, Darren L De Zeeuw, Tamas I Gombosi, Clinton PT Groth, Hal G Marshall, and Kenneth G Powell. Adaptive blocks: A high performance data structure. In *Proceedings of the 1997 ACM/IEEE conference on Supercomputing*, pages 1–10, 1997.

P. A. Sturrock. Model of the High-Energy Phase of Solar Flares. , 211:695–697, August 1966. doi: 10.1038/211695a0.

Hu Sun, Ward Manchester, Zhenbang Jiao, Xiantong Wang, and Yang Chen. Interpreting lstm prediction on solar flare eruption with time-series clustering. *arXiv preprint arXiv:1912.12360*, 2019.

V. S. Titov, Z. Mikic, T. Török, J. A. Linker, and O. Panasenco. 2010 August 1-2 Sympathetic Eruptions. I. Magnetic Topology of the Source-surface Background Field. , 759(1): 70, November 2012. doi: 10.1088/0004-637X/759/1/70.

F. Toffoletto, S. Sazykin, R. Spiro, and R. Wolf. Inner magnetospheric modeling with the Rice Convection Model. *Space Sci. Rev.*, 107:175–196, 2003. doi: 10.1023/A:1025532008047.

RB Torbert, JL Burch, TD Phan, M Hesse, MR Argall, J Shuster, RE Ergun, L Alm, R Nakamura, KJ Genestreti, et al. Electron-scale dynamics of symmetric magnetic reconnection diffusion region in space. *Science*, 362(6421):1391–1395, 2018.

T. Török, B. Kliem, and V. S. Titov. Ideal kink instability of a magnetic loop equilibrium. , 413:L27–L30, 2004. doi: 10.1051/0004-6361:20031691.

G. Tóth, D. L. De Zeeuw, T. I. Gombosi, W. B. Manchester, A. J. Ridley, I. V. Sokolov, and I. I. Roussev. Sun to thermosphere simulation of the October 28-30, 2003 storm with the Space Weather Modeling Framework. *Space Weather Journal*, 5:S06003, 2007. doi: 10.1029/2006SW000272.

G. Tóth, Y. J. Ma, and T. I. Gombosi. Hall magnetohydrodynamics on block adaptive grids. *J. Comput. Phys.*, 227:6967–6984, 2008. doi: 10.1016/j.jcp.2008.04.010.

G. Tóth, B. van der Holst, I. V. Sokolov, D. L. De Zeeuw, T. I. Gombosi, F. Fang, W. B. Manchester, X. Meng, D. Najib, K. G. Powell, Q. F. Stout, A. Glocer, Y-J. Ma, and M. Opher. Adaptive numerical algorithms in space weather modeling. *J. Comput. Phys.*, 231:870–903, 2012. doi: 10.1016/j.jcp.2011.02.006.

G. Tóth, X. Jia, S. Markidis, B. Peng, Y. Chen, L.K.S. Daldorff, V. Tenishev, D. Borovikov, J. Haiducek, T. Gombosi, A. Glocer, and J. Dorelli. Extended magnetohydrodynamics with embedded particle-in-cell simulation of ganymede's magnetosphere. *J. Geophys. Res.*, 121, 2016. doi: 10.1002/2015JA021997.

G. Tóth, Y. Chen, T. I. Gombosi, P. Cassak, , S. Markidis, and B. Peng. Scaling the ion inertial length and its implications for modeling reconnection in global simulations. *J. Geophys. Res.*, 122:10336, 2017. doi: 10.1002/2017JA024189.

Gábor Tóth. Flexible, efficient and robust algorithm for parallel execution and coupling of components in a framework. *computer Physics communications*, 174(10):793–802, 2006.

Gábor Tóth, Bart Van der Holst, Igor V Sokolov, Darren L De Zeeuw, Tamas I Gombosi, Fang Fang, Ward B Manchester, Xing Meng, Dalal Najib, Kenneth G Powell, et al. Adaptive numerical algorithms in space weather modeling. *Journal of Computational Physics*, 231(3):870–903, 2012.

O.A. Troshichev, V.G. Andezen, S. Vennerstrom, and E. Friis-Cristensen. Magnetic activity in the polar cap - a new index. *Planet. Space. Sci.*, 36:1095, 1988.

O.A. Troshichev, H. Hayakawa, A. Matsuoka, T. Mukai, and K. Tsuruda. Cross polar cap diameter and voltage as a function of PCindex and interplanetary quantities. *J. Geophys. Res.*, 101:13,429, 1996.

Saku Tsuneta. Structure and dynamics of magnetic reconnection in a solar flare. *The Astrophysical Journal*, 456:840, 1996.

Bruce T Tsurutani, Walter D Gonzalez, Alicia LC Gonzalez, Fernando L Guarnieri, Nat Gopalswamy, Manuel Grande, Yohsuke Kamide, Yoshiya Kasahara, Gang Lu, Ian Mann, et al. Corotating solar wind streams and recurrent geomagnetic activity: A review. *Journal of Geophysical Research: Space Physics*, 111(A7), 2006.

Toichi Tsutomu and Miyazaki Teruki. Flapping motions of the tail plasma sheet induced by the interplanetary magnetic field variations. *Planetary and Space Science*, 24(2):147–159, 1976.

N.E. Turner, T.I. Pulkkinen, D.N. Baker, and R.L. McPherron. Evaluation of the tail current contribution to *Dst*. *J. Geophys. Res.*, 105:5431, 2000.

Alfred L Vampola. Thick dielectric charging on high-altitude spacecraft. *Journal of electrostatics*, 20(1):21–30, 1987.

V. M. Vasyliunas. Plasma distribution and flow. In A. J. Dessler, editor, *Physics of the Jovian Magnetosphere*, pages 395–454. Cambridge University Press, New York, 1983.

Martin Volwerk, Nicolas Andre, CS Arridge, CM Jackman, Xianzhe Jia, Stephen E Milan, Aikaterini Radioti, MF Vogt, AP Walsh, Rumi Nakamura, et al. Comparative magnetotail flapping: An overview of selected events at earth, jupiter and saturn. In *Annales Geophysicae*, volume 31, pages 817–833. Copernicus GmbH, 2013.

X. Wang, Y. Chen, G. Toth, W. Manchester, T. Gombosi, A. Hero, Z. Jiao, H. Sun, M. Jin, and Y. Liu. Predicting solar flares with machine learning: investigating solar cycle dependence. *Astrophys. J.*, 895:3, 2020. doi: 10.3847/1538-4357/ab89ac.

JM Webster, JL Burch, PH Reiff, AG Daou, KJ Genestreti, Daniel B Graham, RB Torbert, RE Ergun, SY Sazykin, A Marshall, et al. Magnetospheric multiscale dayside reconnection electron diffusion region events. *Journal of Geophysical Research: Space Physics*, 123(6): 4858–4878, 2018.

SP Williamson, J Hayes, F Lewis, WR Bell, JF Devine, H Bell, D Wells, K Hodgkins, V Cox, R Fisher, et al. National space weather program: Strategic plan. *FCMP30-2010 Washington DC*, page 32, 2010.

M. Wiltberger, W. Lotko, J. G. Lyon, P. Damiano, and V. Merkin. Influence of cusp o+ outflow on magnetotail dynamics in a multifluid mhd model of the magnetosphere. *J. Geophys. Res.*, 115(A10):148–227, 2010. doi: 10.1029/2010JA015579.

R. A. Wolf, M. Harel, R. W. Spiro, G.-H. Voigt, P. H. Reiff, and C. K. Chen. Computer simulation of inner magnetospheric dynamics for the magnetic storm of July 29, 1977. *J. Geophys. Res.*, 87:5949–5962, 1982. doi: 10.1029/JA087iA08p05949.

C. C. Wu, R.J. Walker, and J. M. Dawson. A three-dimensional MHD model of the Earth's magnetosphere. *Geophys. Res. Lett.*, 8:523–526, 1981.

Daren Yu, Xin Huang, Huaning Wang, and Yanmei Cui. Short-Term Solar Flare Prediction Using a Sequential Supervised Learning Method. , 255(1):91–105, Mar 2009. doi: 10.1007/s11207-009-9318-9.

Yiqun Yu and Aaron J Ridley. Exploring the influence of ionospheric o+ outflow on magnetospheric dynamics: dependence on the source location. *Journal of Geophysical Research: Space Physics*, 118(4):1711–1722, 2013.

Yuan Yuan, Frank Y. Shih, Ju Jing, and Hai-Min Wang. Automated flare forecasting using a statistical learning technique. *Research in Astronomy and Astrophysics*, 10(8):785–796, Aug 2010. doi: 10.1088/1674-4527/10/8/008.

Binzheng Zhang, Oliver J Brambles, William Lotko, and John G Lyon. Is nightside outflow required to induce magnetospheric sawtooth oscillations. *Geophysical Research Letters*, 47 (6):e2019GL086419, 2020.

Weiqun Zhang, Ann Almgren, Vince Beckner, John Bell, Johannes Blaschke, Cy Chan, Marcus Day, Brian Friesen, Kevin Gott, Daniel Graves, et al. Amrex: a framework for block-structured adaptive mesh refinement. *Journal of Open Source Software*, 4(37):1370–1370, 2019.

Hongyang Zhou, Gábor Tóth, Xianzhe Jia, Yuxi Chen, and Stefano Markidis. Embedded kinetic simulation of ganymede's magnetosphere: Improvements and inferences. *Journal of Geophysical Research: Space Physics*, 124(7):5441–5460, 2019.

Hongyang Zhou, Gábor Tóth, Xianzhe Jia, and Yuxi Chen. Reconnection-driven dynamics at ganymede's upstream magnetosphere: 3-d global hall mhd and mhd-epic simulations. *Journal of Geophysical Research: Space Physics*, 125(8):e2020JA028162, 2020a.

Hongyang Zhou, Gábor Tóth, Xianzhe Jia, and Yuxi Chen. Reconnection-driven dynamics at ganymede's upstream magnetosphere: 3-d global hall mhd and mhd-epic simulations. *Journal of Geophysical Research: Space Physics*, 125(8):e2020JA028162, 2020b.

Ellen G Zweibel and Masaaki Yamada. Magnetic reconnection in astrophysical and laboratory plasmas. *Annual review of astronomy and astrophysics*, 47:291–332, 2009.